

AMERICAN UNIVERSITY OF BEIRUT

BASED ON THE EXTENDED THICK SHEAR ZONE ANALYSIS:
METAL CUTTING AS MATERIAL CHARACTERIZATION
TECHNIQUE

by
CHARBEL YOUSSEF SEIF

A dissertation
submitted in partial fulfillment of the requirements
for the degree of Doctor of Philosophy
to the Department of Mechanical Engineering
of the Maroun Semaan Faculty Engineering and Architecture
at the American University of Beirut

Beirut, Lebanon
April 2020

AMERICAN UNIVERSITY OF BEIRUT

BASED ON THE EXTENDED THICK SHEAR ZONE ANALYSIS: METAL CUTTING AS MATERIAL CHARACTERIZATION TECHNIQUE

by
CHARBEL YOUSSEF SEIF

Approved by:

Dr. Kamel Abu Ghali, Professor
Department of Mechanical Engineering,
MSFEA, AUB, Beirut, Lebanon

Committee Chair

Dr. Ramsey Hamade, Professor
Department of Mechanical Engineering,
MSFEA, AUB, Beirut, Lebanon

Advisor

Dr. Mutasem Shehadeh, Associate Professor
Department of Mechanical Engineering,
MSFEA, AUB, Beirut, Lebanon

Committee Member

Dr. Peter Krajnik, Professor
Department of Industrial and Materials Science,
Chalmers University of Technology, Göteborg, Sweden

Committee Member

Dr. Ali Ammouri, Visiting Assistant Professor.
Department of Industrial and Mechanical Engineering,
School of Engineering, LAU, Byblos, Lebanon

Committee Member

Dr. Elsa Maalouf, Assistant Professor
Department of Chemical Engineering and Advanced Energy
MSFEA, AUB, Beirut, Lebanon

Committee Member

Date of dissertation defense: April 15th, 2020

AMERICAN UNIVERSITY OF BEIRUT

THESIS, DISSERTATION, PROJECT RELEASE FORM

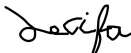
Student Name: Charbel Seif Youssef
Last First Middle

Master's Thesis Master's Project Doctoral Dissertation

I authorize the American University of Beirut to: (a) reproduce hard or electronic copies of my thesis, dissertation, or project; (b) include such copies in the archives and digital repositories of the University; and (c) make freely available such copies to third parties for research or educational purposes.

I authorize the American University of Beirut, to: (a) reproduce hard or electronic copies of it; (b) include such copies in the archives and digital repositories of the University; and (c) make freely available such copies to third parties for research or educational purposes after:

One ---- year from the date of submission of my thesis, dissertation, or project.
Two ---- years from the date of submission of my thesis, dissertation, or project.
Three ---- years from the date of submission of my thesis, dissertation, or project.

 11/05/2020
Signature Date

ACKNOWLEDGMENTS

I would like to express my special appreciation to my advisor Prof. Ramsey Hamade; you have been a tremendous mentor for me. I want to acknowledge your encouragement detrimental to my transformation into a research scientist. The priceless mentoring you provided was necessary for the development of my career. I want to show my gratefulness to Prof. Kamel Abu Ghali, the committee chair who continuously supported my work. Also, I would like to express my recognition to the esteemed committee members for providing me with constructive comments making my thesis defense an enjoyable moment. A special acknowledgment is dedicated to the technical staff at the American University of Beirut mechanical shops, especially Mr. Joseph Nassif. All of you have been there to realize my Ph.D. work.

I would express a distinct appreciation to my wife, Ilige Hage, who was always available to support me. Gratefulness to my wife, my mother, and my father, cannot be expressed for all the sacrifices that you've made on my behalf. And finally, I would like to dedicate my work to my wife and three children Joseph, Michelle, and Mathea, who constantly provided me with Love, Enthusiasm, and Happiness that helped me realize this work.

OBJECTIVES

The dissertation objectives are summarized as:

- Implement the Drilling and Turning setups for machining data collection
- Validate the use of thick shear zone approach methodology to characterize cut material.
- Extend the thick shear zone force simulation methodology to account for Zerilli Armstrong, BCC, FCC, and HCP models.
- Extend the thick shear zone force simulation methodology to account for the analytical moving heat source based thermal machining model.

AN ABSTRACT OF THE DISSERTATION OF

Charbel Youssef Seif for Doctor of Philosophy
Major: Mechanical Engineering

Title: Based on The Extended Thick Shear Zone Analysis: Metal Cutting as Material Characterization Technique

Material characterization under various loading conditions is essential for researchers to evaluate its response under operational conditions. The presented research focuses on metal machining simulation and benefits from the variation of cutting conditions encountered along the drill bit cutting lip to conceive a procedure for updating material model subject to the cutting action. Specifically, the presented methodology, dubbed the drill lip cutting force prediction methodology, utilizes a small number of pre-cored drilling experiments to extract the Johnson-Cook (JC) parameters for Aluminum Al6061-T6 material.

Machining simulation is based on the existing thick shear zone simulation approach. The DLCFPM is modified to account for multiple material models popular in literature as an extension to Oxley machining prediction methodology through substituting the original velocity-modified power form material model by the widely used constitutive material model developed by Zerilli and Armstrong (ZA) of types applicable to hexagonal close-packed (HCP), body-centered cubic (BCC) and face-centered cubic (FCC) metals.

Magnesium alloy of the type AZ31B is used as an application and cutting experiments coupled with the HCP Zerilli Armstrong material model used to update the material parameters following the inverse methodology based on turning operations.

Also, the conceived machining forces simulation thick shear zone accounted for the variations of ZA constitutive laws applicable to body-centered cubic (BCC) and face-centered cubic (FCC) and validated against literature reported machining tests. Validation of the ZA FCC extension is performed against reported Aluminum 6061-T6 turning tests. And the BCC/FCC dual methodology is challenged against performed AISI 1045 literature reported turning experiments.

A thermal extension is adopted for the thick shear zone approach by modifying the moving heat source analytical solution. The adopted thermal extension is coupled with the conceived drill lip cutting force prediction methodology for simulating the drilling process. This methodology validated by comparing to experimentally collected drilling torque, thrust, and drill lip flank temperatures based on Aluminum 6061-T6 workpiece material.

The outcomes of the research are defined by extending the thick shear zone approach to account for the Zerilli Armstrong material model variations along with accounting for the modified moving heat source thermal model. The proposed thick shear zone approach validated for simulating machining response under simple orthogonal cutting along with simulating complex machining processes such as drilling. The conceived machining simulation methodology also used as a material characterization tool for modeling the material response subject to operating strain, strain rates, and temperatures encountered in machining through the inverse method. As an application, the conceived simulation method may be used by machinists for simulating cutting conditions, thus optimizing the tool geometry as well as identifying operational parameters that satisfy the reduced tool wear and energy consumption criteria.

CONTENTS

ACKNOWLEDGMENTS	v
OBJECTIVES	vi
ABSTRACT	vii
LIST OF ILLUSTRATIONS	xiv
LIST OF TABLES	xx
NOMENCLATURE.....	xxii
Chapter	
I. INTRODUCTION	1
A. Experimental machining applications	2
B. Overview of Empirical Machining Models.....	2
C. Twist drill adopted for data collection	3
D. Overview of Existing Analytical Machining Models	4
1. Development of Thin Shear Plane Analyses for Orthogonal Machining	4
2. Development of Thick Shear Zone Analyses for Orthogonal Cutting	5
3. Development of Thick Shear Zone Analyses for Drilling	6
4. Constitutive Equations That Describe Material Behavior	6
E. Drill lip force prediction inverse methodology.....	7
F. AZ31b Zerilli-Armstrong HCP updated parameters forms extended thick shear zone approach.....	8
G. Zerilli-Armstrong BCC/FCC forms extended thick shear zone approach. ..	9

H. Thick shear zone approach extension to account for the conceived analytical temperature solution	10
I. Thesis Organization	10
II. MACHINING PARAMETERS ANALYSIS	
EXPERIMENTAL WORKS	12
A. Drilling Experimental Setup	12
B. Orthogonal Machining Experimental Setup	16
C. Summary	18
III. UTILIZING THE DRILL CUTTING LIP TO EXTRACT	
JOHNSON COOK FLOW STRESS PARAMETERS FOR	
AL6061-T6	19
A. Introduction	19
B. Drilling Experiments	24
C. Shear Zone Formulations for the Drill's Cutting Lip Force Prediction	27
1. Two-Dimensional Orthogonal Cutting Shear Zone Model.....	27
2. Extending Shear Zone Formulation for JC-Type Constitutive Equation (e.g., Al 6061-T6)	34
3. Oblique cutting Model (based on Lin [40])	35
4. Extended JC Shear Zone Approach Applied To Drill Cutting Lip Force Prediction	38
D. Determining the Johnson-Cook Equation Parameters for Al 6061-T6.....	42
E. Validation of Methodology Using FEM Simulations	45
1. FEM model setup	45
2. FEM results	46
F. Comparison of the Drill Lip Cutting Force Prediction Methodology versus FEM and Experimental Drilling Measurements	47
G. Summary and Conclusions	52

IV. EXTRACTING HCP ZERILLI-ARMSTRONG MATERIAL PARAMETERS FROM ORTHOGONAL CUTTING TESTS ON AZ31B MAGNESIUM 54

A. Introduction 54

B. Experimental Force Collection and Processing 57

 1. Force Collection..... 57

 2. Cutting pressures..... 62

B. Oxley shear zone approach extension to Zerilli Armstrong constitutive law for HCP materials 65

 1. ZA-extended Oxley's for HCP materials 67

 2. AZ31B Thermo-physical Properties 70

D. Determining ZA material model via the inverse method 71

E. Validation of ZA-extended Oxley's for AZ31B: Cutting forces and state variables 72

F. Validation of ZA-extended Oxley's for AZ31B: Stress-Strain behavior ... 75

G. Discussion..... 78

H. Conclusion 79

V. INCORPORATING DUAL BCC/FCC ZERILLI-ARMSTRONG AND BLUE BRITTLINESS CONSTITUTIVE MATERIAL MODELS INTO OXLEY’S MACHINING SHEAR ZONE THEORY 81

A. INTRODUCTION 81

B. Oxley’s thick shear zone analytical model 84

C. Tasks INVOLVED IN EXECUTING THE METHODOLOGY 89

D. Za-extended Oxley's for single (bcc or fcc) phase materials (task 1) 91

E. Validation of Za-Extended Oxley’s For Single (Bcc Or Fcc) Phase Materials: Aluminum 6061-T6 (Task 2)..... 94

F. Za-material model for dual (bcc and fcc) phase materials (task 3)..... 99

G. Za-extended Oxley's for dual (bcc and fcc) phase materials: aisi1045 steel (task 4).....	103
H. Conclusions	108
VI. INCORPORATING CUTTING TEMPERATURE DISTRIBUTION INTO OXLEY'S MACHINING SHEAR ZONE THEORY	109
A. Introduction	110
B. Methodology	113
C. Experimental	114
D. Thermal extension of Oxley thick shear zone approach adapted Zerilli- Armstrong	118
E. Analytical approach simulating shear and tool chip interface temperature.....	120
1. Workpiece side temperature modeling	122
2. Chip side temperature modeling	123
3. Temperature modeling on the tool side.....	130
4. Discretization for the tool chip heat partition ratio.	130
5. Comparison against temperature contours presented in the literature	132
F. Oxley Zerilli Armstrong adapted a thick shear zone approach thermal extension.	133
G. Validation of Orthogonal cutting simulation methodology	137
H. Validation of Drilling simulation methodology	139
I. Discussion.....	145
J. Conclusion	146
VII CONCLUSION	148
A. Summary of Results and Contributions.....	148
B. Recommendations and Future Research Developments	150

BIBLIOGRAPHY	151
Appendix	
I. APPENDIX 1.....	161
II. APPENDIX 2	162
A. Appendix A	162

LIST OF ILLUSTRATIONS

Figure		
1.1	Merchant stack of cards model Merchant [11].....	4
2.1	a) Drilling experimental set up b) Aluminum 60601-T6 drilled specimen.....	12
2.2	a) Drilling experimental set up b) Aluminum 60601-T6 drilled specimen.....	13
2.3	a) Inverted drill with fixed thermocouples b) Inverted drilling setup d) Photograph of drilling experiment d) Pre-cored Workpiece e) Drilled Workpiece	14
2.4	Experimental collected a) torque and thrust force profiles b) temperature profiles.	15
2.5	a) Guhring twist drill series 768 b) Guhring twist drill series 223.....	16
2.6	Diagram representation of the Orthogonal cutting force data collection.....	17
2.7	a. Photograph of orthogonal cutting force measurement set up, b. Photograph of a cut.....	18
3.1	Extracting JC parameters based on the proposed DLCFPM methodology from drilling tests.....	23
3.2	Photographs of a) drilling set up with dynamometer, b) Al 6061-T6 workpiece with pre-cored hole (diameter =3.5 mm), c) fully drilled workpiece, and d) typical torque and thrust force profiles.	25
3.3	The parameters and force components involved in orthogonal cutting.....	27
3.4	Flow chart for the shear zone solution following Oxley [30]	30

3.5	Oblique cutting model based on the shear zone formulation Lin [40].....	36
3.6.	Oblique cutting parameters and force components Lin [40].....	37
3.7	Features and geometry of the cutting point of the traditional chisel drill (a) front view, (b) and top view.	39
3.8	Variations of the geometric angles along the cutting lip as function of non-dimensional radius	40
3.9	Lip force predication module Williams [1].....	42
3.10	Conversion histories of the Equation 3.1, JC parameters A, B, C, n, and m versus iteration number.....	44
3.11	Workpiece a) showing the pre-cored pilot hole and b) while being drilled in FEM (showing chip generation).	46
3.12	FEM results for plots of (a) temperature, (b) effective stress, (c) strain, and (d) strain rate for the 2.5 mm pre-cored workpiece simulation (rotational speed of 9868 rpm and feed of 0.64 mm/revolution).	47
3.13	Comparative plots of (L) torque and (R) thrust force profiles generated by DLCFPM and compared to experiments and FEM (spindle speed 9868 rpm, tool feed = 0.64mm/rev). From top to bottom pre-cored holes = 2.5 mm 3.5 mm, 5.5 mm, and 7.5 mm, respectively.....	49
3.14	(a) Engaged Lip Torque and (b) Thrust force results for experimental, FEM, and DLCFPM numerical results.....	49
3.15.	Shear plane and tool-chip interface temperatures: DLCFPM versus FEM results reported at (rotational speed of 9868 rpm and feed of 0.64 mm/revolution).	50

3.16.	Comparative plots of (L) torque and (R) thrust force profiles generated by DLCFPM and compared to experiments and FEM. Drilling parameters of pre-cored hole diameter, spindle speed, and tool feed rate are: (top) 3.5 mm, 6366 rpm, 0.32 mm/rev, (middle) 5.5 mm, 3183 rpm, 0.16 mm/rev, and (bottom) 7.5 mm, 1592 rpm, 0.08 mm/rev.....	52
4.1	Workpiece configuration (left) arrangement and dimensions and (right) photograph revealing ring arrangement.....	58
4.2	(a) Photograph of orthogonal cutting force measurement set up, (b) Photograph of a cut specimen. (c) Diagram representation of the orthogonal cutting force setup.....	59
4.3	(left) photograph of AZ31B cut concentric tubes specimen; (right) sample of collected cutting and thrust forces: at 2000Hz sampling rate, $V=400$ m/min, $t_1=0.3$ mm.....	60
4.4	Raw experimental machining (a) cutting and (b) thrust pressures versus cutting speed for uncut chip thickness = 0.05, 0.1, 0.2, 0.3, and 0.4 mm.	63
4.5	Zero feed extrapolation a. Cutting forces. b. Thrust.....	64
4.6	Corrected experimental machining (a) cutting and (b) thrust pressures versus cutting speed for uncut chip thickness = 0.05, 0.1, 0.2, 0.3, and 0.4 mm.....	64
4.7	Shear zone's orthogonal cutting parameters and force components ([52]).	65
4.8	Flowchart illustrating the Zerilli-Armstrong thick shear zone extension methodology.....	69
4.9	Case#2: Conversion records of ZA parameters.....	72
4.10	Numerical (solid lines) and experimental (data points) machining results for (a) cutting and (b) thrust forces versus cutting speed for uncut chip thickness = 0.05, 0.1, 0.2, 0.3, and 0.4 mm.	74

4.11	Shear and tool-chip interface temperatures: numerical versus those reported by [59] and [60].	75
4.12	Validation of the found AZ31B Zerilli Armstrong model plotted against strains for 100, 150, and 250 C at strain rates of: a) 1000, b) 1400, c) 1500, and d) 3000 s ⁻¹ . Data from [55] co-plotted as points.	76
4.13	Validation of the found AZ31B Zerilli Armstrong model plotted against strains for 45, 150, and 250 C at strain rates of: a) 500 s ⁻¹ , b) 1000 s ⁻¹ , and c) 1500 s ⁻¹ . (Data from [25] co-plotted as points).	77
5.1	Shear zone's orthogonal cutting parameters and force components.	86
5.2	Flowchart for Oxley's [30] thick shear zone analysis	87
5.3	Flowchart illustrating the development and validation process for extending the thick shear zone to include ZA flow stress models for dual FCC/BCC materials.	90
5.4	Flowchart illustrating the Zerilli-Armstrong thick shear zone extension methodology.	93
5.5	Aluminum 6061-T6 flow stress according to ZA [74] and JC [36] models as compared with experimental data [74] at temperatures: a) 100 °C, and b) 350 °C.	95
5.6	Cutting force components for Al 6061-T6: Experimental data (Adibi et al. [29], Guo [21]) and Oxley-ZA extended methodology results (this work): a) Cutting Force Component at 8° rake angle, b) Thrust Force Component at 8° rake angle, c) Cutting Force Component at 6° rake angle, d) Thrust Force Component at 6° rake angle.	96
5.7	Chip thickness for Al 6061-T6: Experimental data (Adibi et al. [29], Guo [21]) and Oxley-ZA extended methodology results.	99

5.8	AISI-1045 flow stress for Oxley, JC, and ZA constitute models compared with experimental data ([69],[70]): a) for BCC crystal structure versus strain, b) for FCC crystal structure versus strain, c) for BCC crystal structure versus temperature, d) for FCC crystal structure versus temperature.	102
5.9	Methodology ZA based material model definition a) function of temperature b) comparison versus Oxley [30], Johnson cook [69] Modified Johnson cook by Sartkulvanich et al. [75] material models at $10000s^{-1}$ & $0.7mm/mm$	103
5.10	Cutting force components for AISI 1045 steel: Oxley experimental data Oxley [30], Ivester experimental data [76], Oxley numerical results Oxley [30], Oxley extended to JC results [19], and Oxley-ZA extended methodology results [this work]: a, c, e) Cutting force for rake angle = -7° , -5° , and 5° respectively; b, d, f) Thrust force for rake angle = -7° , -5° , and 5° respectively.	105
5.11	Chip thickness for AISI 1045 steel: Oxley experimental data Oxley [13] versus and Oxley-ZA extended methodology predicted results for rake angle = (left) - 5° and (right) 5°	107
6.1	Photograph reporting a) Pre-cored Workpiece b) Drilled workpiece c) Guhring RT150 straight flute drill d) Thermocouples brazed on the drill flank face ...	114
6.2	Photograph reporting a) Drill with brazed thermocouples fixed in inverted positions b) Inverted Drilling Set up c) Drilling experiment following inverted setup d) Machine Center.	115
6.3	Experimentally measured a) Sample temperature data b) Sample torque and thrust data.....	118
6.4	Shear zone's orthogonal cutting parameters and force components.	119
6.5	Workpiece boundary conditions.....	122
6.6	Tool chip interface heat generation profile	129
6.7	Tool chip heat partition ratio.....	131

6.8.	Comparison for AISI 1045 steel: a) This work thermal model contours b) Published machining temperature contours Komanduri [93]	132
6.9	Flowchart illustrating the development and validation process for extending the thick shear zone to include ZA flow stress models for dual FCC/BCC material	135
6.10	Comparison for AISI 1045 steel: a) interface Saglam [32] versus and Oxley-ZA extended methodology	138
6.11	Comparison for AISI 1045 steel: a) Cutting Forces Saglam [32] versus and Oxley-ZA extended methodology b) thrust Forces Saglam [32] versus and Oxley-ZA extended methodology	139
6.12	Drill Force and temperature simulation flow diagram	141
6.13	Comparison for Al 6161-T6: a) Drilling torque (this work) [32] versus and Oxley-ZA extended methodology b) Drilling thrust (this work) versus and Oxley-ZA extended methodology c) Flank temperature (this work) versus and Oxley-ZA extended methodology	143
6.14	Simulated temperature versus experimentally collected flank temperature comparison	145

LIST OF TABLES

Table

3.1	List of literature-reported parameters for JC-type material flow stress models	21
3.2	Geometry of the utilized HSS chisel point drills.....	26
3.3	Drilling test cases with cutting process parameters listed.	26
3.4	Ranges, initially assigned values, and optimized JC parameter values.....	43
4.1	Experimental orthogonal cutting test results.....	61
4.2.	ZA parameters: ranges, initially assigned values, and determined values.....	71
4.3	Estimated generated state variables.	73
4.4.	ZA parameters comparison against Kurukuri et al. [61] and Hasenpouth [25].	79
5.1	Aluminum 6061-T6 Orthogonal tests summary.....	98
5.2	AISI 1045 Orthogonal tests summary	106
6.1	Guhring RT150 Straight Flute Drills Geometric Characteristics.....	116
6.2	Drilling test matrix.....	117
6.3	Drilling test matrix Saglam [32].....	137
S-1a.	Shear Zone Model validation results for 0.2% carbon and rake angle of -5 degrees	161
S-1b.	Shear Zone Model validation results for 0.38% carbon and rake angle of +5 degrees case.....	161

S-2 JC extended Shear Zone Model validation results for 0.38% carbon steel161

NOMENCLATURE

Symbol	Description
K_s	Adjusted' specific cutting power
h, t_1	Uncut chip thickness (mm)
ϕ	Shear angle.
T	Material temperature
D	Drill diameter
F	Drilling feed rate
V	Cutting speed
W	Web thickness
T	Torque
(θ_0)	Drill helix angle
$2p$	Drill point angle
Ψ	Drill chisel angle
RPM	Rotation per minute
Dia	Diameter
M	Torque (nm)
T	Thrust (N)
F_h	Horizontal forces
F_v	Vertical forces
α_n	Normal rake angle
Γ	Chisel dynamic rake angle
F_t	Thrust (N)
A	Rake angle
K_{nc}	Normal cutting pressure
K_{tc}	Tangential Cutting pressure
ρ	Non-dimensional drill lip radius
R	Drill diameter
M	Total number of lip elements
BL	Lip element Length
κ	Drill point half-angle
δ_w	Element width
RPM	Rotational speed
r_j	Radial position of the jth
t_1	Uncut chip thickness
$\beta(\rho)$	Local helix angle
$\theta(\rho)$	Web angle
$i(\rho)$	Inclination angle
TQ_j	Measured torque value
TH_j	Measured thrust value
ϵ	Operating strain
$\dot{\epsilon}$	Operating strain rate
$\dot{\epsilon}_0$	Reference strain rate

T_r	Room temperature
T_m	Melting temperature
N	Cutting tool normal force
RF	Resultant cutting force
P	Cutting tool friction force
F _s	Shear plane force
F _n	Normal to shear plane force
F _{feed}	Feed force
F _t	Tangential force
S1	Primary shear deformation zone thickness
S2	Secondary tool chip interface deformation zone thickness S2
C'	Primary deformation zone thickness ratio
Δ	Secondary deformation zone thickness ratio
t ₂	Chip thickness
θ _R	Resultant force angle
T _{AB}	Shear zone temperature
V _s	Shear zone speed
λ	Friction angle
k _{AB}	Shear zone average shear stress
Y _{AB}	Shear zone average shear strain
Ȳ _{AB}	Shear zone strain rate
l	Shear zone length
T _w	Room temperature
H	Shear zone heat partition ratio
ΔT _m	Maximum temperature rise in the chip
Ψ	Tool chip interface heat partition ratio
ρ _d	Workpiece density
C _p	Workpiece specific heat
β _T	Boothroyd Workpiece heat partition ratio
RT	Non-dimensional thermal number
K	Workpiece thermal conductivity
h	Tool/chip contact length
ΔT _c	Average chip temperature rise
τ _{int}	Tool chip interface stress
σ _N	Normal stress
n'	Strain hardening index
k _{chip}	Chip flow stress
n _{eq}	Strain-hardening exponent
F' _t	Oblique cutting force
F' _{feed}	Oblique thrust force
F' _r	Force components normal to F' _t and F' _{feed}
η _c	Chip flow angle
ω	Rotational speed

$\theta(\rho)$	Drill Lip web angle
$\beta(\rho)$	Local helix angle
$\alpha_f(\rho)$	Effective rake angle
$\alpha_n(\rho)$	Normal rake angle
t_2	Chip thickness
JC	Johnson cook
ZA	Zerilli armstrong
BCC	Body-centered Chrystal structure
FCC	Face centered Chrystal structure
HCP	Hexagonal close pack
Fce	Cutting parasitic forces
Fte	Thrust parasitic forces
K_c	Cutting pressure
K_r	Thrust pressure
q_s	Shear zone heat generation
Ko(x)	Modified Bessel function of the second kind of order zero
$T_{work-shear}$	Workpiece temperature distribution
$T_{chip-shear}$	Chip temperature distribution
q_f	Tool chip interface friction heat generation
q_p	Tool chip interface plastic deformation heat generation
L_c	Tool chip contact length
$T_{chip-friction}$	Tool temperature distribution
T_{tool}	Tool chip temperature distribution

CHAPTER I

INTRODUCTION

During the past few years, considerable development made concerning machine tool design, where developed more and more sophisticated machine tools targeting to minimize machining power consumption and increasing tool life. Considering the increased need for improving the overall manufacturing efficiency, optimizing the cutting process represents a challenge for many researchers. Applications seek correlations between cutting parameters such as (speed and feed) tool geometry, materials properties, with the generated cutting forces and machine power consumption. Other researchers adopted a more sophisticated approach following mechanistic models to determine the cutting, thrust, and power in metal cutting, such as reported by Williams [1]. This research investigates the use of machining experiments to characterize the response of the material at varying machining parameters of uncut chip thickness, cutting speed, and rake angle. Varying the said machining parameters results in different operating strain, strain rate, and temperatures allowing the investigation of the different machining models to characterize the material response and define competing effects reported as:

- Softening of the work material due to thermal softening caused by heat generation at the shear plane and the tool-work interface.
- Work hardening associated with high strain rates at the shear plane (proportional to cutting speed).

A. Experimental machining applications

Machining experiments have long been investigated to examine and characterize the material removal processes. Turning experiments arrangement similar to reported by [2] is applied by researchers as an application to orthogonal cutting machining. While complex 3D cutting is investigated following milling and drilling experiment. Part of analyzing material response under machining conditions performed turning experiments on Magnesium alloy A31B material for investigating orthogonal cutting response. Also, drilling experiments on Aluminum 6161-T6 workpiece are performed following the full drill arrangement following Wiriyacosol and Armarego [2] to investigate the Drill action, including the chisel edge and pre-cored workpiece arrangement reported by Hamade et al. [3] to analyze the drill bit cutting lip action.

B. Overview of Empirical Machining Models

Early works adopted the specific cutting power models based on the empirical parameter to estimate the specific cutting power function of uncut chip thickness, t_1 , through a power relation of the form as presented by Sabberwal [4] in Eq. 1.1.

$$K_s = K t_1^{-p} \quad (1.1)$$

where K_s is the 'adjusted' specific cutting power, and p is a constant. A widely accepted range for K_s for Aluminum is 800-900 W.s/m³ at a reference uncut chip thickness of 0.25 mm (0.01 in). Presented by Rao et al. [5] experimental data for specific cutting energy reduction with increasing cutting speed. For example, turning of Aluminum 6061-T6 exhibits a decrease in cutting forces for cutting speeds up to about 3000 m/min. Some equations also account for the effect of parameters such as rake angle and other geometric features. Examples of such

approaches include models developed by Chandrasekharan et al. [6], Stephenson, and Bandyopadhyay [7] and Hamade et al. [3] for modeling orthogonal cutting processes applied to the metallic material. Others, like Kumar et al. [8], proposed to include the material Brinell hardness to account for machining forces.

C. Twist drill adopted for data collection

The geometry and cutting mechanics of the classical twist drill are well developed over the years. It is well recognized that the drill chisel edge contributes mostly to the generation of thrust force, while the torque is generated mostly due to the cutting action of the lip. Although the lips contribute to some thrust generation, they are responsible for generating the bulk of the cutting forces in drilling.

Early, Oxford Jr. [9] investigated the geometry and mechanics of drilling. He divided the drill into three different cutting zones; at the lip reporting, the oblique cutting process is involved where the angle of obliquity decreases as the radial position of lip element considered increases. As for the lip's normal rake angle α , it increases from a negative to a positive value as the distance from the center increases. To estimate cutting force distributions, Pal et al. [10] were the first to apply machining cutting models to simulate drilling. The drill lip is divided into several elements, and Merchant [11] type thin shear zone model for single edge orthogonal used to represent the deformation at each element of the lip. They also established methods for estimating the cutting forces along the cutting lip where the lip is modeled as assumed to be a series of small, adjacent, and inclined cutting edges. Wiriycosol and Armarego [2] used an approach by which they

assumed that the drill's cutting edges consisting of small inclined cutting elements that is treated as separate cutting edges.

Consequently, drilling presents an opportunity to be utilized as a replacement for traditional 2D (orthogonal) or 3D (oblique) turning tests. To isolate the cutting forces generated by the lip, drilling experiments were conducted following (Hamade et al. [3] and Kouam et al.[12]) setup.

D. Overview of Existing Analytical Machining Models

There are two types of approaches in modeling the cutting process, the shear plane model developed by Merchant [11], where the shear zone is assumed to be a thin plane and the shear zone approach where Oxley[13] based his analysis on a thick shear deformation zone.

1. Development of Thin Shear Plane Analyses for Orthogonal Machining

Orthogonal machining is a simple two-dimensional machining model for simulating planning shaping and turning process, where the material is removed by a cutting edge that is perpendicular to the direction of the relative tool-workpiece velocity.

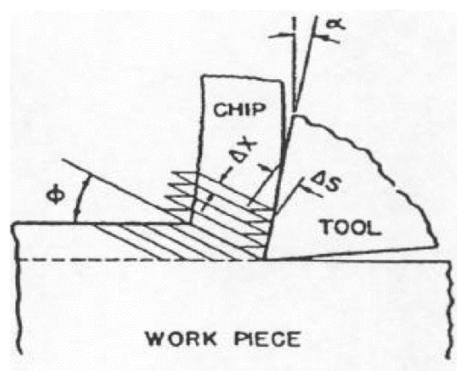


Figure 1.1. Merchant stack of cards model Merchant [11]

Piispén [14], Ernst [15], and Merchant [11] were the first to propose the shear plane model for orthogonal machining; they assumed that the chip is formed by shearing along a single plane inclined at an angle ϕ defined as the shear angle. The shear angle ϕ is evaluated function of the chip thickness ratio r_c and the rake angle α_r , following Eq. 1.2

$$\phi_c = \tan^{-1}\left(\frac{r_c \cos(\alpha_r)}{1 - r_c \sin(\alpha_r)}\right) \quad (1.2)$$

Limitation of the thin shear approach inherited by its extensive reliance on experimentally collected data such as the chip thickness ratio and the material cutting empirical energy equations to provide force estimates.

2. Development of Thick Shear Zone Analyses for Orthogonal Cutting

A more general approach, as proposed by Oxley [13], defined as the thick shear zone approach where the deformation is assumed to occur in a narrow band centered on the shear plane where the moment equilibrium also introduced. The basis of this theory is to analyze the stress distribution occurring at the primary deformation zone along the shear plane AB and the secondary deformation zone at the tool/chip interface in terms of the shear angle ϕ (angle made by plane AB and the cutting velocity) and work material properties including the strain, strain rate, and temperature effect. Then selecting ϕ so that the resultant forces transmitted by the shear plane and the interface plane are in equilibrium, the tool is assumed to be perfectly sharp. Once ϕ is known, the chip thickness t_2 and the various components of force can be determined from simple geometrical and kinematical transformations.

3. Development of Thick Shear Zone Analyses for Drilling

Watson [16] proposed a drilling model for the cutting lip and chisel using the thick shear zone developed by Oxley [13]. Where the lip is divided into small oblique cutting elements and the chisel divided into a secondary orthogonal cutting zone and the indenting zone. Drilling experiments were conducted on K1045 steel to verify his model. In a comprehensive treatise of the mechanics of drilling, one of Watson's [16] major conclusions was that the distribution of thrust and torque across the length of the cutting lip is not uniform. Elements near the chisel edge corner contributed to thrust, while the majority of the torque is produced by portions of the lip adjacent to the outside diameter. The model also predicted a decrease in torque and thrust as the cutting speed increases. Experimental measurements on pre-drilled pilot holes were made that provided corroborating evidence. More recently, Elhachimi et al. [17] proposed an integration scheme to calculate the distribution of thrust and torque along the lip (and chisel) edge where the integrand is a function of the properties of the machined material, cutting conditions, and drill point geometry.

4. Constitutive Equations That Describe Material Behavior

Knowledge of material flow stress data as a function of the cutting conditions is necessary for cutting force estimation using an analytical thick shear zone approach. In his work Oxley[13] adopted a power form material model reported in Eq. 1.3

$$\sigma = \sigma_1 \varepsilon^n \quad (1.3)$$

While some constitutive equations include such variables as material response models describe the properties (such as modulus or strength) as a function of strain, strain rate, and

temperature. For example is one developed by Johnson and Cook [18] which relates the flow stress to three variables: strain, strain rate, and temperature as follows:

$$\sigma = (A + B \varepsilon^n) \left[1 + C \ln \left(\frac{\dot{\varepsilon}}{\dot{\varepsilon}_0} \right) \right] \left[1 - \left(\frac{T - T_r}{T_m - T_r} \right)^m \right] \quad (1.4)$$

Where ε is the plastic strain, $\frac{\dot{\varepsilon}}{\dot{\varepsilon}_0}$ is the dimensionless plastic rate, T is the material temperature, T_r is reference temperature, and T_m is the material melting temperature. Additionally, the five experimentally determined material constants defined as, A , the yield stress, B , the strain hardening coefficient, n the strain-hardening exponent, C , the strain-rate dependent coefficient, and, m , the temperature-dependent coefficient. Where the constitutive equation is formed by the strain and strain rate hardening terms, and the thermal softening term. By assuming adiabatic deformation at high strain rates, it allows for a reduction in the strength corresponding to the increase in temperature. Lalwani et al. [19] presented the extension of Oxley[13] thick shear zone approach to account for the widely used Johnson-Cook material model.

E. Drill lip force prediction inverse methodology

Using drill bit cutting lip machining data as a means for finding material constants allows the authors to benefit from the significant variations in cutting parameters encountered along the lip cutting edge. Adopted the Lalwani et al. [19] extended Oxley's thick shear zone approach accounting for the JC material model, where used the drill lip model for calculating generated cutting forces based on drilling conditions and JC material model. Using optimization schemes, JC material model parameters found by minimizing the error between calculated drill bit cutting lip forces and experimentally measured machining forces at matching rotational speed and feed

rate. Also, the authors utilize FEM simulations for further corroboration of the accuracy of the obtained JC flow stress parameters. Unlike the large number of orthogonal machining tests typically required (e.g., (Daoud et al.[20], Guo et al. [21], and Naik and Naik [22])), only a small number of drilling tests are required for determining a material's constitutive equation.

F. AZ31b Zerilli-Armstrong HCP updated parameters forms extended thick shear zone approach

Considering the studied Magnesium alloys to have a hexagonal close pack (HCP) crystal arrangement, defined in this research an extension of the Oxley [13] thick shear zone approach to account for a crystal structure-dependent material model of the HCP Zerilli Armstrong (ZA) form presented by Zerilli [23]. The benefit of using the HCP Zerilli Armstrong (ZA) for modeling the response of Magnesium alloys is validated by Ammouri and Hamade [24] for modeling AZ31b material. Also, in the is research presented the use of an inverse scheme that uses machining experiments to find updated AZ31b Zerilli-Armstrong HCP material model that correlate with experimentally found cutting and thrust machining force using the conceived extended thick shear zone approach. In this research, found updated AZ31b material model is validated by comparison against material stress response reported by Ammouri and Hamade [24] and Hasenpouth [25] at encountered strain, strain rate, and temperature conditions occurring in machining operation.

G. Zerilli-Armstrong BCC/FCC forms extended thick shear zone approach.

Popular material models such as the Zerilli-Armstrong (ZA) constitutive model [26] have crystal structure dependency model. As reported by Zerilli and Armstrong [26], ZA flow stress formulation for body-centered cubic (BCC) is described by

$$\sigma = c_0 + c_1 \exp\left(-c_3 T + c_4 T \ln\left(\frac{\dot{\epsilon}}{\dot{\epsilon}_0}\right)\right) + c_5 \epsilon^n \quad (1.5)$$

The normalized strain rate is a ratio of the equivalent strain rate $\dot{\epsilon}$ to reference strain rate $\dot{\epsilon}_0$. The terms c_0 , c_1 , c_2 , c_3 , c_4 , c_5 , and n are Zerilli – Armstrong material constants. While the ZA flow stress formulation for face-centered cubic (FCC) materials originally reported in [26] by

$$\sigma = c_0 + c_2 \epsilon^n \exp\left(-c_3 T + c_4 T \ln\left(\frac{\dot{\epsilon}}{\dot{\epsilon}_0}\right)\right) \quad (1.6)$$

Presented the Oxley [27] methodology extension by correlating the thick shear zone parameters compatible with Zerilli-Armstrong BCC and FCC material models also the presented methodology accounts blue brittleness effect caused by the localized precipitate formation defined by Long [28]. Validation of the Oxley ZA FCC methodology is performed through comparison with published orthogonal cutting tests reported by Adibi et al. [29] and Guo [21]. Also, the performance of the Oxley ZA BCC/FCC dual-material model methodology is justified through comparison with orthogonal tests reported by Oxley [30] and Lalwani et al. [19]. The advanced methodology incorporates the Zerilli-Armstrong dual BCC and FCC models, and the blue brittleness model dubbed ZA-BB into the machining simulation thick shear zone approach.

H. Thick shear zone approach extension to account for the conceived analytical temperature solution

As development presented a thick shear zone machining simulation methodology applied to Zerilli Armstrong BCC/ FCC dual-material model, Oxley thick shear zone approach by substituting Boothroyd [31] empirical approach with the updated analytical temperature solution for the shear zone and tool-chip interface zone temperature model. Part of methodology validation steel AISI 1040 is evaluated and compared with cutting forces and temperatures collected using turning experiments and reported in the literature by Saglam et al. [32]. Also, the presented methodology is coupled with the conceived Drill Lip Force Prediction module (DLFPM) and used for simulating drilling flank surface temperature and validated against performed drilling experiments.

I. Thesis Organization

In addition to the introduction chapter, the thesis is organized into six chapters:

- Part one provides a literature review relating to machining force prediction models along with a description of approach followed in this thesis.
- Part two reports the implementation of complex cutting experiments using the drilling experiments as a means for machining data collection. Drilling experiments performed on pre-cored workpieces (Excluding chisel effect) to analyze the effect of cutting tool geometry and operational conditions of speed and feed on the cutting pressures of Aluminum 6061-T6 material.
- Part three conceived the use of drill bit cutting lip modeling as materials characterization tool to find through optimization scheme improved Aluminum 6061-

T6 Johnson cook material model parameter to satisfy predictably of experimentally collected drilling torque and thrust using the conceived drill bit cutting lip edge model.

- Part four updates the HCP Zerilli Armstrong Material model parameter for the AZ31B material using the conceived Oxley thick shear zone approach extended to HCP Zerilli Armstrong material model inversely based on performed orthogonal cutting experiments covering a wide range of conditions.
- Part five provides a description of the conceived thick-shear zone approach extension accounting for crystal structure-dependent material models such as BCC and FCC Zerilli Armstrong material models applied to AISI 1040 steel and A6061-T6 Aluminum alloy.
- Part six describes improved orthogonal cutting shear and tool-chip interface thermal model. Also, in this chapter presented the development of the extended shear zone model by coupling it with the conceived improved shear and interface zones temperature models.
- Part seven is a concluding chapter summarizing work done and proposing further research areas of development.

CHAPTER II

MACHINING PARAMETERS ANALYSIS EXPERIMENTAL WORKS

This research presents an investigation of the extended machining models with the application to both complex machining processes such as drilling and to simple orthogonal cutting processes such as turning. Part of achieving set targets this chapter presents development of a machining force and temperature measuring arrangement necessary for the generation of operating force and temperature validation data. Collected experimental machining forces and temperatures are generated using drilling material removal setup in addition to simple orthogonal machining tuning test arrangement.

A. Drilling Experimental Setup

Aiming to investigate the variation in cutting conditions occurring at the different zones of the drilling tool adopted a 4-component dynamometer (Kistler type model 9123) is integrated with the CNC machining center.

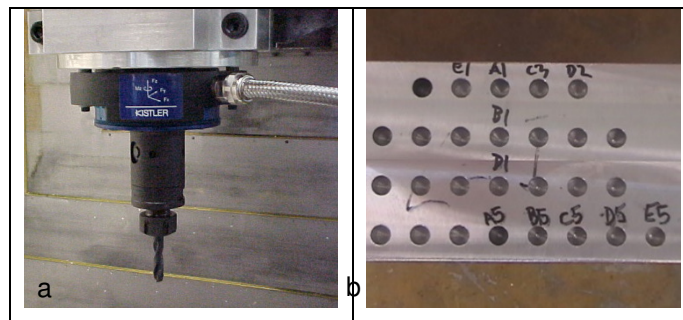


Figure 2.1 a) Drilling experimental set up b) Aluminum 60601-T6 drilled specimen

Shown in Figure 2.1a is standard drilling set up adopted for the drill lip cutting edge machining forces investigation reported in chapter 3. The presented setup consists of standard

arrangement where the cutting drill bit is fixed to a rotary 4-component dynamometer Kistler type model 9123 fixed on a 5 axis CNC milling machine type Deckel Maho machining center model DMU 80P equipped with standard SK 40 motor spindle delivering 15kW maximum power at 12000 rpm maximum spindle speed and 130Nm maximum torque

Also presented in Figure 2.1b is a rectangular Aluminum 6061-T6 workpiece utilized with this setup where each rectangular workpiece can account for multiple drilling experiments.

Targeting to measure the temperature at flank face implemented a variation of the standard drilling setup by fixing the drill in an inverted set up where thermocouples passed through the coolant holes and fixed on the flank surface using high-temperature brazing.

Presented in Figure 2.3 is the implemented force and temperature measurement realized inverted set up.

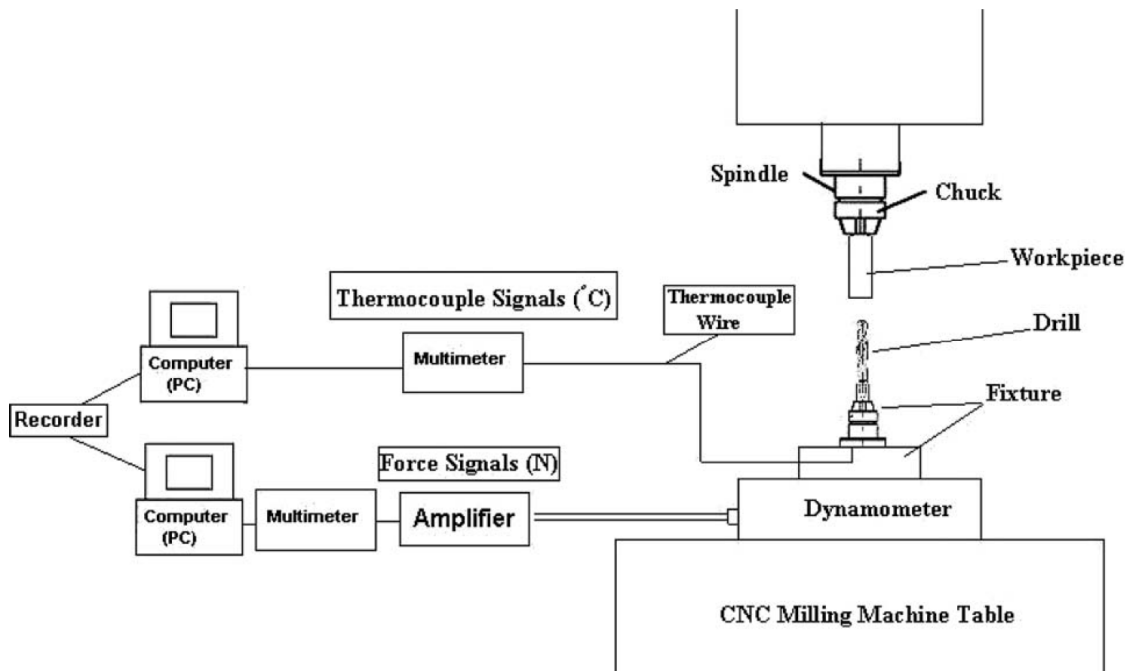


Figure 2.2 a) Drilling experimental set up b) Aluminum 60601-T6 drilled specimen

Adopted drilling depth per experiment $2.3 * D$ inline with drilling experiment reported by Hamade el al. [3]. In order to limit the study to the cutting lip zone, drilling experiments were conducted with a pre-cored hole of 2.5mm slightly larger than the chisel edge diameter.

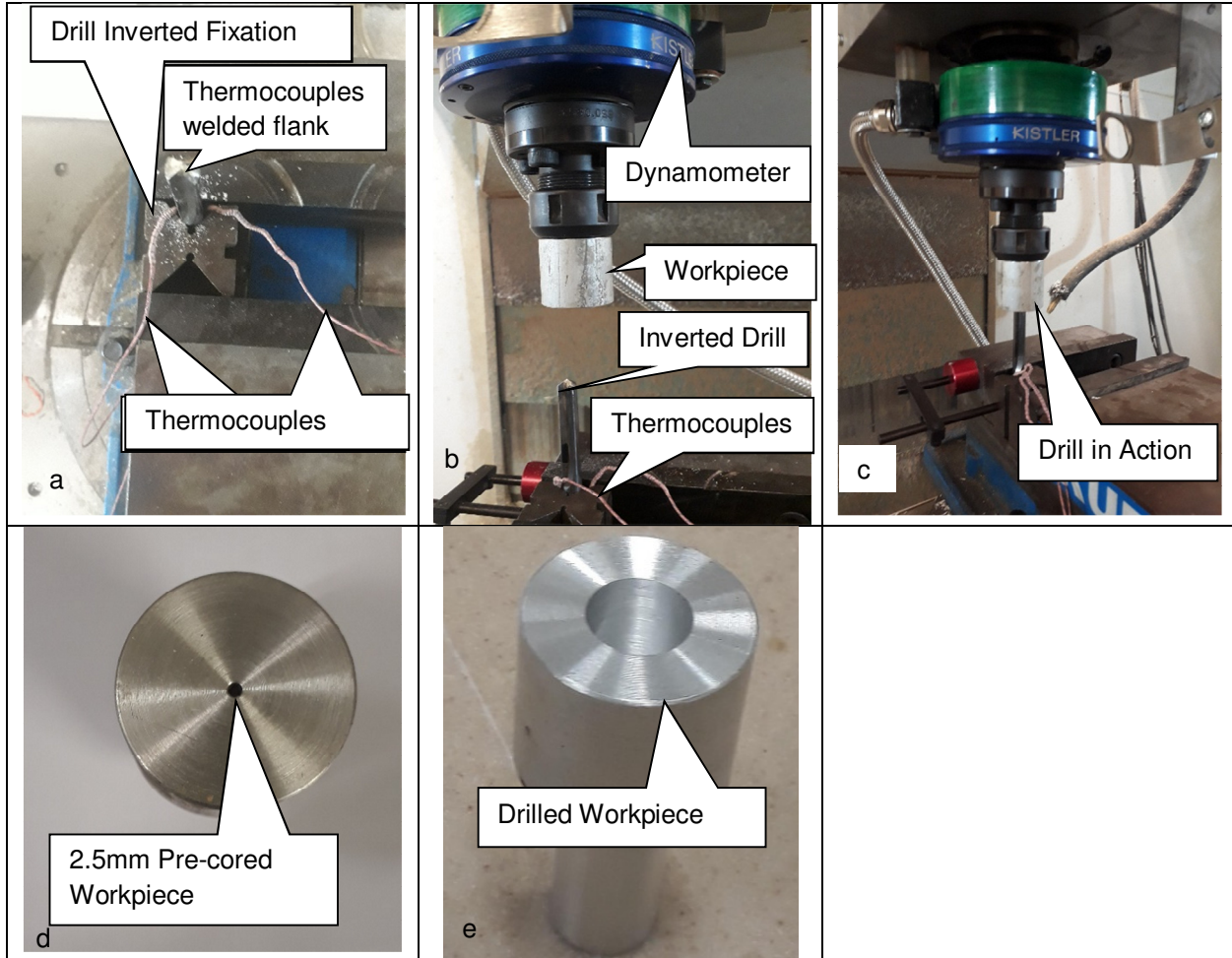


Figure 2.3 a) Inverted drill with fixed thermocouples b) Inverted drilling setup d) Photograph of drilling experiment d) Pre-cored Workpiece e) Drilled Workpiece

Shown in Figure 2.3a are photos of the inverted drilling setup presenting the implementation of the inverted arrangement where the workpiece fixed to the rotary dynamometer, and the drilling tool utilized in an inverted position. This setup allows the integration of thermocouples within the drilling coolant holes allowing to collect both force and temperature measurement data while the drilling process occurs. The advantage of the inverted

setup is highlighted by the fact that thermocouples are welded to the fixed drill enabling temperature measurements without any alteration the drilled workpiece. 2.4b is photography of pre-cored workpiece designed explicitly for this experiment, and Figure 2.4c is an image for a drilled workpiece after the experiment completion

Shown in Figure 2.4a are sample torque and thrust data collected using the 4-channel rotary dynamometer (Kistler type model 9123) at a 3000 Hz sampling rate under the action of a standard HSS drilling tool of 10mm diameter operated at a spindle speed of 9868 rpm, and 0.64mm/rev feed rate. Also shown in Figure 2.4 b are the temperature measurements based on 15 mm Drilling depth collected at 0.16mm/rev feed rate and 2228 Rpm rotational speed.

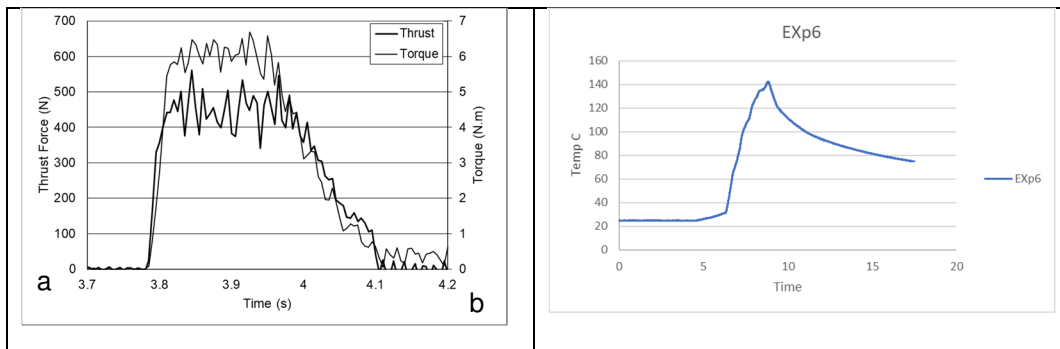


Figure 2.4. Experimental collected a) torque and thrust force profiles b) temperature profiles.

Inverted drilling experimental set up is adopted for machining forces investigation reported in chapter 3 while drilling temperature measurements experimental setup is adopted in work presented in Chapter 6

As presented in Figure 2.5a, reports Ghuring series 768 twist drills adopted for experiments collecting force measurements. Figure 2.5b presents Ghuring series 223 straight drills utilized for force and temperature measurement experiments where thermocouples are passed though the Ghuring series 223 straight drills coolant holes and brazed at the flank surface of the cutting lip.

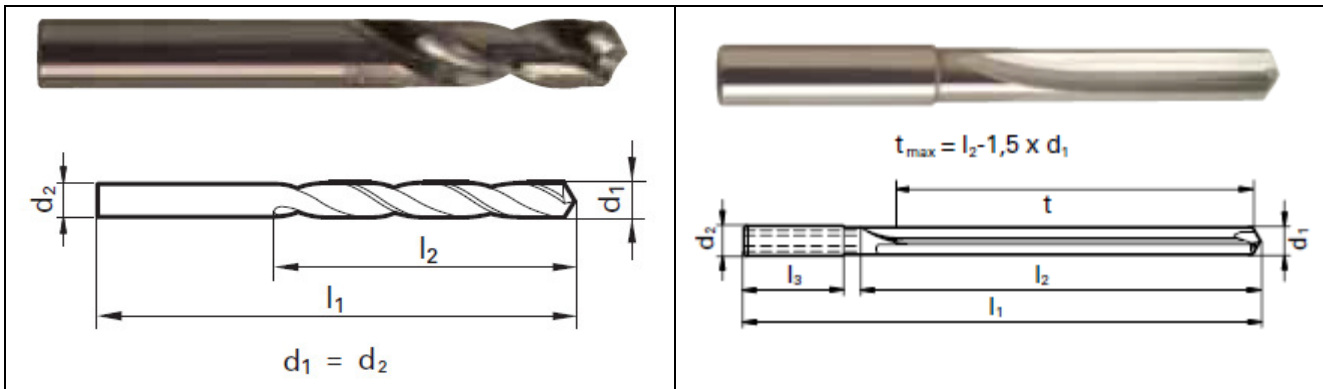


Figure 2.5 a) Guhring twist drill series 768 b) Guhring twist drill series 223

B. Orthogonal Machining Experimental Setup

Machining experiments have long been investigated to examine and characterize the material removal processes. Part of validating machining forces collected using complex drilling setup presented in this research the use of turning tests as a complementary means for machining forces data collection. Early orthogonal machining experiments were conducted by Merchant [11] to validate the thin shear plane machining approach. Turning tests commonly found as a tool to collect orthogonal cutting process data. Orthogonal machining tests set up presented a valuable data collection tool adopted for validating the work presented in this research. Presented in Figure 2.6 is a representation of the orthogonal cutting set up adopted using TCMW 16T308 triangular carbide tools inserts fixed on the SFCR1616H16 screw-On type tool holder. Kistler type 3-Component plate Dynamometer (Type 9254) utilized to provide machining force measurements; signal amplified through Multi-channel charge amplifier type 5070A

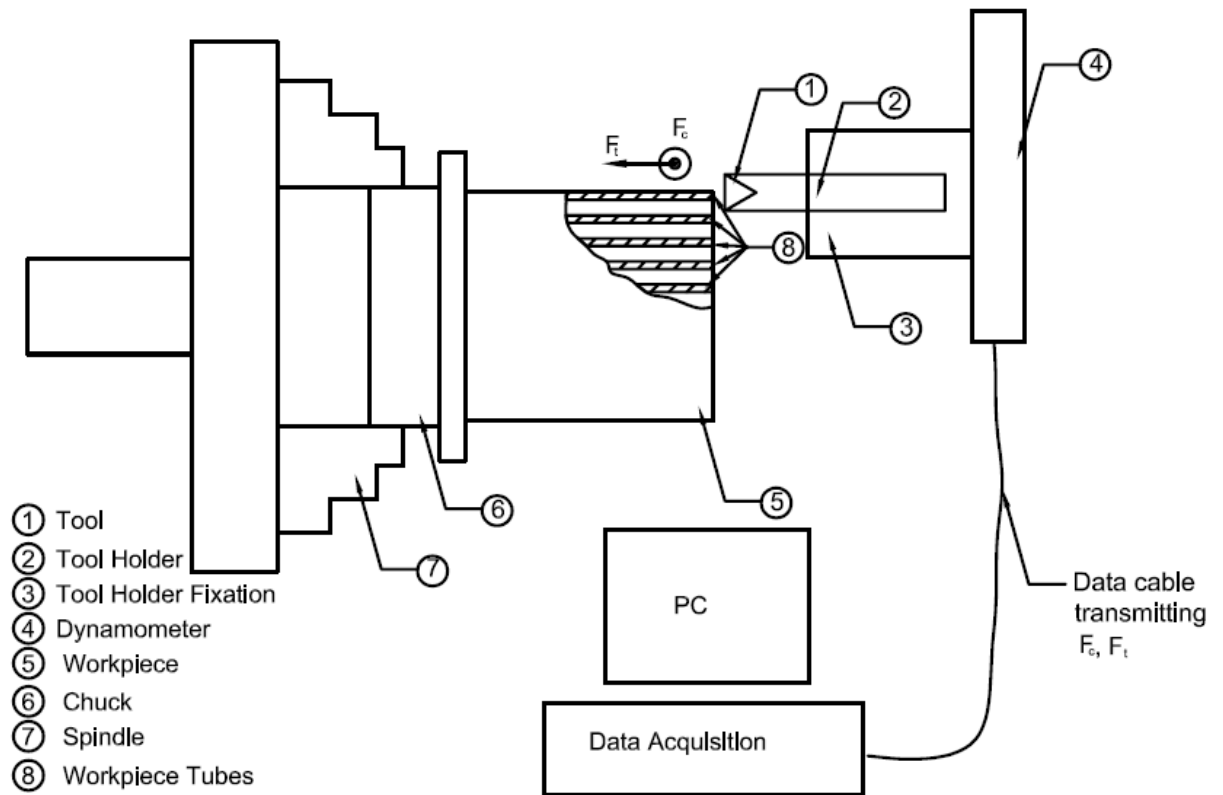


Figure 2.6 Diagram representation of the Orthogonal cutting force data collection

As presented in Figure 2.7a, aiming to collect orthogonal cutting data experimentally, conceived integration between Kistler type 3-Component plate Dynamometer (Type 9254) and lathe machine center. Tool Rake angle cutting speed and operating feed were varied, and three-component cutting force F_c , thrust force F_t , and radial force F_r collected. Figure 2.7b shows a photograph of the machined workpiece. Kistler Dynamometer signal is transmitted through Multi-channel charge amplifier type 5070A. Concentric tube workpiece geometry is implemented in order to simulate orthogonal cutting at constant cutting speed per tube.

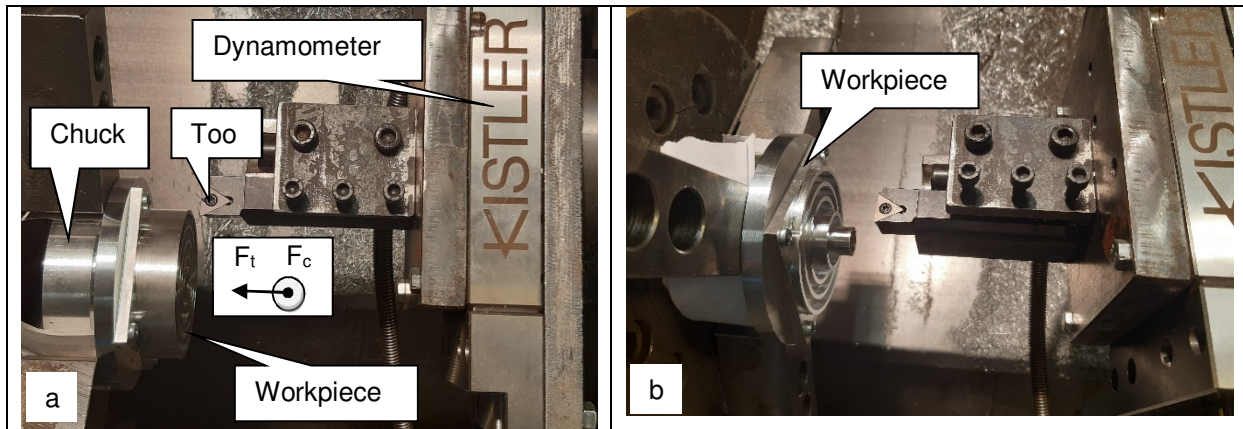


Figure 2.7 a. Photograph of orthogonal cutting force measurement set up, b. Photograph of a cut

C. Summary

Considering that this research concentrates on characterizing material using machining experiments, implementation of complex drilling and simple turning test setups was detrimental for the progress of the work. The implemented force and temperature machining data collection arrangements provided necessary data for validating the conceived machining models described in the subsequent chapters. The test setups dictated the use of machined workpiece geometries inline with the test procedures.

CHAPTER III

UTILIZING THE DRILL CUTTING LIP TO EXTRACT JOHNSON COOK FLOW STRESS PARAMETERS FOR AL6061-T6

Owing to the chisel drill lip's complex geometric configuration, the material being cut witnesses great variations in strain, strain rate, and temperature along the cutting edge. This characteristic is explored so that the drill point is utilized as a material characterization tool to extract the flow stress parameters of the material being cut. Specifically, the methodology, dubbed the Drill Lip Cutting Force Prediction Methodology (DLCFPM), utilizes a small number of pre-cored drilling experiments to extract the Johnson-Cook (JC) parameters for Aluminum Al6061-T6. Few drilling experiments are run to cover a wide range of drilling conditions: spindle speeds ranging from 1592 rpm rotational speed to 9868 rpm and drilling feed rates ranging from 0.08 mm/rev to 0.64 mm/rev.

A. Introduction

Constitutive equations have long been employed to simulate the mechanical response of solids under variable loading conditions of strain, strain rate, and temperature. In order to determine the parameters for such equations, numerous experiments employing mechanical tests (e.g., tension, compression) would need to be conducted. Considering the great efforts typically involved in generating such material models, cutting experiments have been employed as an alternative method for determining such parameters. This is due to the fact that cutting is characterized by wide ranges of operating state variables of strain, ϵ , (100-1000%), strain rate, $\dot{\epsilon}$, ($10^3 - 10^6 \text{ s}^{-1}$), and temperature (0.16 to 0.9 of T/T_{melt}) as presented by Kalpakjian [33]. This

unique characteristic of cutting operations and the resulting wide ranges of values of the encountered state variables gives rise to an opportunity to utilize cutting experiments as characterization means to extract constitutive laws parameters of the workpiece being cut (e.g., (Shrot and Bäker, [34])).

Starting from a limited number of drilling experiments, this research aims to provide a methodology that identifies Johnson-Cook (JC) material constitutive model parameters. Considering its wide use as an industrial application material, this study is concerned with Aluminum 6061-T6 as the workpiece material. In their work, Hamade and Ismail [35] studied aggressive drilling in Aluminum and reported on applicable material flow stress models. However, given how widely accepted is the Johnson-Cook (JC) formulation presented by [18], concerned with this type of material flow stress model typically reported as

$$\sigma = (A + B\epsilon^n) \left[1 + C \ln \left(\frac{\dot{\epsilon}}{\dot{\epsilon}_0} \right) \right] \left[1 - \left(\frac{T - T_r}{T_m - T_r} \right) \right]^m \quad (3.1)$$

where the first two terms are the strain and strain rate hardening terms, respectively, and the third term accounts for temperature softening. In Eq. (3.1), ϵ is the true plastic strain, $\dot{\epsilon}/\dot{\epsilon}_0$ is the normalized strain rate, and the term $\left[1 - \frac{T - T_r}{T_m - T_r} \right]$ is the material homologous temperature. A, B, C, n, m are five material parameters that need to be determined typically by fitting to experimental data.

Based on the application and the studied loading parameter ranges, different researchers utilized different experimental methods to determine the desired JC parameters. Table 3.1 lists a number of works that report the values of such parameters for Aluminum 6061-T6 including compression testing by Johnson et al. [36], Taylor impact test by Rule [37], dynamic punch tests presented by Dabboussi [38], bullet-impact test by Manes et al. [39], combined compression and

orthogonal cutting tests presented by Guo [21], and orthogonal cutting tests by Naik and Naik [22]. Also, based on orthogonal tests conducted on Aluminum 6061-T6 material, Daoud et al.[20] reported updated JC parameters based on response surface methodology optimization scheme combined with Oxley [30] machining models using reported work by Johnson et al. [36] as initially estimate values of JC parameters. While other reported values vary depending on the method, the reported parametric values in Johnson et al. [36] for Aluminum 6061-T6 JC type material flow stress are 324 MPa, 114 MPa, 0.002, 0.42, 1.34 for A, B, C, n, and m, respectively. Parameters reported by Johnson et al. [36] are applicable for strain values up to 500%, strain rates up to 103 s^{-1} , and temperatures similar to those encountered in machining operations. For all cases listed, the 6061-T6 material melting temperature is identified as $582 \text{ }^\circ\text{C}$.

Table 3.1. List of literature-reported parameters for JC-type material flow stress models

Reference	A (MPa)	B (MPa)	N	C	m	$\dot{\epsilon}_0$	Test conducted
Johnson et al., [36]	324	114	0.42	0.002	1.34	1	Compression tests
Rule [37]	164	211	0.465	0.00197	1.419	1	Taylor compression tests
Dabboussi and Nemes [38]	335	85	0.11	0.012	1	1	Punch tests
Manes et al. [39]	270	138.2	0.1792	0.1301	1.34	597.2	Bullet test
Guo[21]	275	86	0.39	0.05810- 194.091t ₀ - 0.00306V	1	0.01	Orthogonal machining / compression tests
Daoud et al. [20]	250	79.7	0.499	0.0249	1.499	1	Orthogonal machining
Naik and Naik, [22]	337	136	0.0025	0.5	1.34	1	Orthogonal machining

Utilizing Oxley's thick shear zone approach, the authors employ a drill lip model for calculating generated cutting forces based on drilling conditions and JC material model. Using

non-linear regression optimization schemes found are JC material model parameters that minimize the error between calculated drill bit cutting lip forces and experimentally measured machining forces at matching rotational speed and feed rate. In addition, the authors utilize FEM simulations for further corroboration of the accuracy of the obtained JC flow stress parameters. Using drill bit cutting lip machining data as a mean for finding material constants allows the authors to benefit from the large variations in cutting parameters encountered along the lip cutting edge. Unlike the large number of orthogonal machining tests typically required (e.g., (Daoud et al.[20], Guo [21], and Naik and Naik [22]), only a small number of drilling tests would be required for determining a material's constitutive equation.

Presented the DLCFPM methodology that incorporates drill parameters (e.g., nominal drill diameter D (mm)), web thickness to diameter ratio $2w/D$, point angle 2ϕ (degrees), nominal helix angle β_0 (degrees), chisel edge angle ψ (degrees)) and cutting conditions (rotational speed (RPM), feed (f : mm/rev)) as inputs for the material characterization methodology. The flowchart in Figure 3.1 summarizes the DLCFPM methodology. Section 3.3.1 summarizes shear zone formulations based on the thick shear zone analysis. Section 3.3.2 reports on the extension of the thick shear zone model by incorporating a JC type material flow stress model (Lalwani et al. [19]) and validates the extended analysis against literature-reported results. Developed in Section 3.3.3 is a three-dimensional (3D) cutting force prediction model using oblique cutting force transformations based on Lin [40] coupled with thick shear zone analysis (Oxley [27]). Section 3.3.4 couples the 3D oblique transformation module with extended Oxley's thick shear zone cutting prediction module (Oxley [27]).

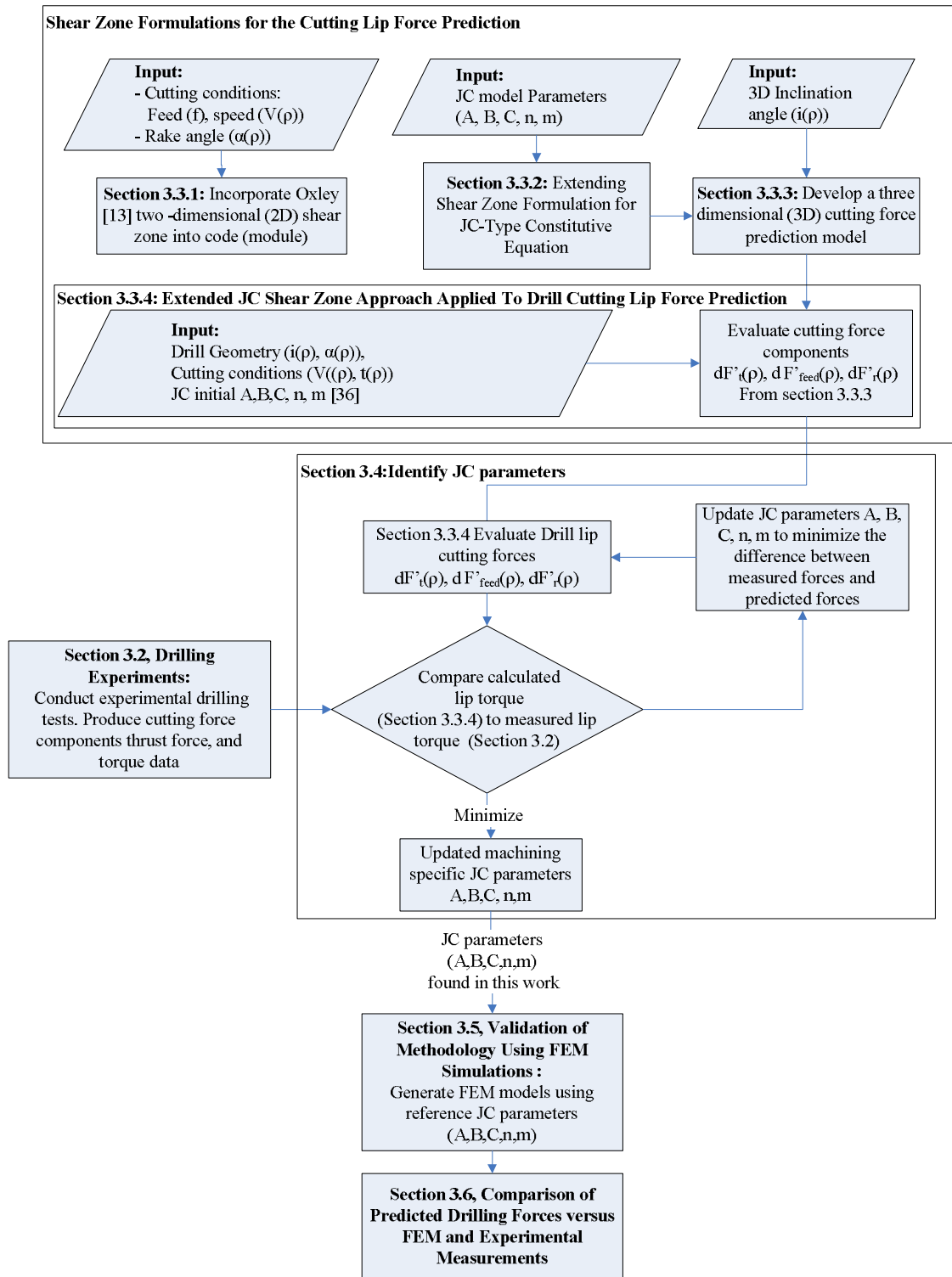


Figure 3.1. Extracting JC parameters based on the proposed DLCFPM methodology from drilling tests

The desired JC parameters are determined in Section 3.4 by minimizing differences between predicted torque values generated by the methodology and the experimental drilling torque measurements. Section 3.5 reports on FEM simulations of the drill's lip forces using the newly found JC parameters. Section 3.6 compares history profiles of torque and thrust forces covering a wide range of drilling parameters of speed and feed as calculated from DLCFPM using JC parameters found by Johnson et al. [36] and those found in Section 3.5, FEM model section, and experimentally collected torque and thrust data (Section 3.4).

B. Drilling Experiments

Drilling tests were conducted using pre-cored holes of diameters larger than the chisel. HSS classical chisel drills were utilized with geometric features of nominal diameter (D), web thickness to diameter ratio ($2w/D$), point angle ($2p$), chisel edge angle (ψ), and helix angle (β_0) at the periphery as listed in Table 3.2.

Cutting forces were collected using four-channel (F_x , F_y , F_z , and torque) Kistler rotary dynamometer (model 9124B) mounted on a Deckel Maho machining center model DMU 80P CNC milling unit having 12000 rpm maximum spindle speed and 130Nm maximum torque.

Thrust force and torque data were collected at a sampling rate of 200 Hz, and the dynamometer reported an uncertainty range of ± 4 N for measured forces and ± 0.3 Nm for measured torque. Dry (no coolant) experiments were conducted using fresh tools. Cylindrical workpieces with an outer diameter of 20mm were utilized.

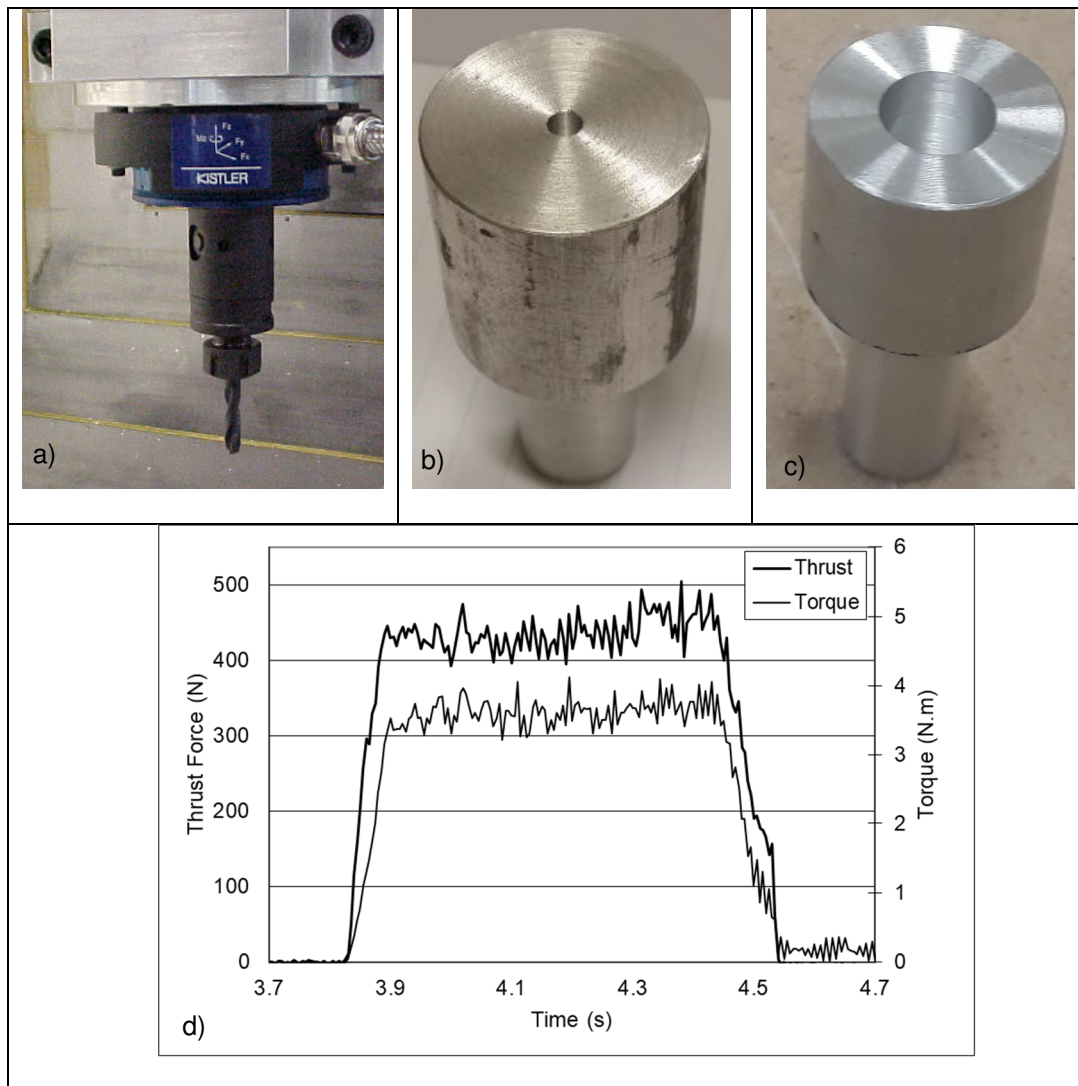


Figure 3.2. Photographs of a) drilling set up with dynamometer, b) Al 6061-T6 workpiece with pre-cored hole (diameter =3.5 mm), c) fully drilled workpiece, and d) typical torque and thrust force profiles.

A photograph of the CNC setup with the dynamometer is shown in Figure 3.2(a), and two photographs with a pre-cored 3.5 mm diameter hole and fully drilled workpiece are shown in Figures 3.2(b) and (c), respectively. Figure 3.2(d) is a typical plot of collected torque and thrust force profiles.

Table 3.2. Geometry of the utilized HSS chisel point drills

HSS drill Parameters	Values
Nominal diameter, D (mm)	10
Web thickness to diameter ratio, 2w/D	0.15
Point angle, 2p (degrees)	119
Nominal helix angle, β_0 (degrees)	17
Chisel edge angle, ψ (degrees)	125

Using a 10 mm diameter drill, cutting torque and thrust force data collected as the drill cutting lip engaged with the workpiece at a rate of 200 Hz and data (typical force profiles can be seen in Figure 3.2(d) at 2.5mm pre-core, 9868 rpm spindle speed and 0.64mm/rev feed rate) using 6061-T6 workpiece with pre-cored holes of 2.5mm, 3.5mm, 5.5mm, and 3.5 mm diameters.

Table 3.3. Drilling test cases with cutting process parameters listed.

Experiment Number	Pre-cored Hole Diameter (mm)	Feed (mm/rev)	Spindle rotation (RPM)
1	2.5	0.64	9868
2	3.5		
3	5.5		
4	7.5		
5	3.5	0.32	6838
6	5.5	0.16	3183
7	7.5	0.08	1592

Drilling torque and thrust measurements are collected for the test cases listed in Table 3.3. To reduce the signal noise, a median filter of 10 data points was applied. All experiments were conducted using fresh tools to eliminate tool wear contribution.

C. Shear Zone Formulations for the Drill's Cutting Lip Force Prediction

Discussed in this section are the formulations employed to calculate cutting forces along the lip.

1. Two-Dimensional Orthogonal Cutting Shear Zone Model

The orthogonal cutting graphics are shown in Figure 3.3 along with its salient features, including a cutting wedge and a rake face with angle (α) as it removes an uncut chip thickness (t_1). By shearing along a shear plane (AB) that makes an angle (ϕ) with the horizontal, the cut material is transformed into a chip of thickness (t_2). Shown in Figure 3.3 are the shear plane (AB), shear plane angle (ϕ), resultant cutting force (RF), cutting tool normal force (N), cutting tool friction force (P), shear plane force (F_s), normal to shear plane force (F_n), feed (F_{feed}), and tangential (F_t) force components.

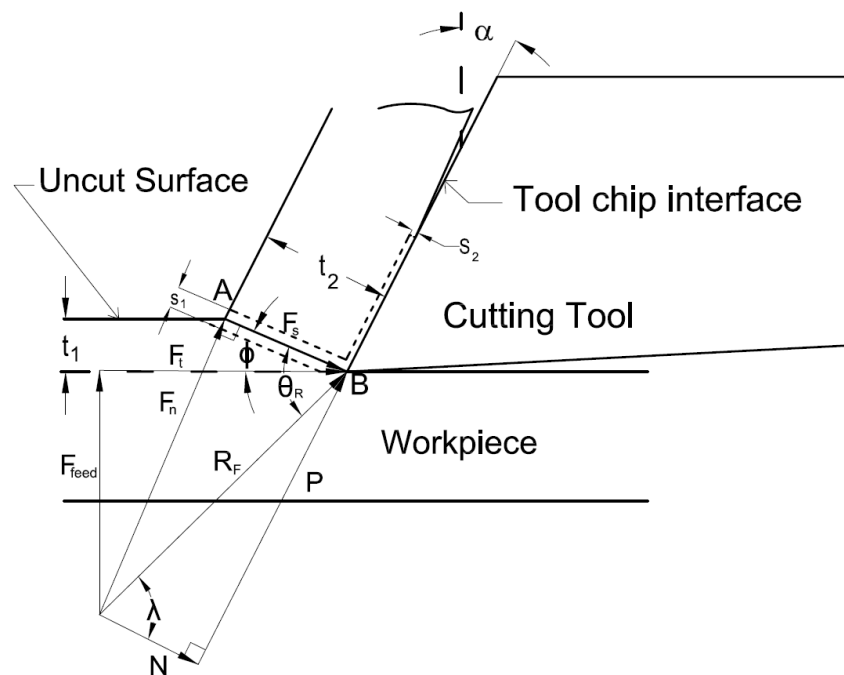


Figure 3.3. The parameters and force components involved in orthogonal cutting

Oxley's (1988) analytical cutting model is based on the parallel-sided thick shear zones where primary shear deformation zone (thickness S_1) and secondary tool chip interface deformation zone (thickness S_2) are defined and shown in Figure 3.3.

The analysis evaluates the shear stress distribution along the primary deformation zone centered at the shear plane (AB) to find balancing normal stress (evaluated along the secondary deformation zone at the tool/chip interface) by varying the shear angle (ϕ), primary deformation zone thickness ratio (C'), and secondary deformation zone thickness ratio (δ). The parameter $C' = l/S_1$ is defined as the ratio of the length of the shear plane AB (l) to the thickness of the primary shear zone (S_1). The parameter $\delta = S_2/t_2$ is estimated as the ratio of the thickness of the secondary deformation zone located at the tool chip interface (S_2) to the cut chip thickness, t_2 ($\delta = S_2/t_2$) where

$$t_2 = \frac{t_1 \cos(\phi - \alpha)}{\sin(\phi)} \quad (3.2)$$

Figure 3.4 is a flowchart that illustrates how δ , C' , and ϕ are varied Oxley [30] for each iteration. For each condition of cutting speed, V , and feed, f , the values of parameters δ , C' , ϕ are varied between 0.005 and 0.2, 2 and 10, and 5 and 45 degrees, respectively, at increments shown in Figure 3.4.

The analysis is performed at all combinations of δ , C' , ϕ and solutions for subject parameters are found for the case that satisfies the balance of forces between the primary deformation and secondary deformation zones.

The angle between the resultant force RF and shear plane direction is θ_R and is defined as

$$\tan(\theta_R) = 1 + 2 \left(\frac{\pi}{4} - \phi \right) - C'n' \quad (3.3)$$

where n' is the material-specific strain hardening exponent found from the material power equation $\sigma = \sigma_1 \varepsilon^n$ [30] and is a function of the shear zone average temperature, T_{AB} , and shear zone deformation speed, V_s . For each value of the calculated resultant angle, θ_R , a corresponding friction angle λ is estimated by Stabler [41] as

$$\theta_R = \phi + \lambda - \alpha \quad (3.4)$$

The resultant cutting force R_F , is found from Oxley [30]

$$R_F = \frac{F_s}{\cos(\theta_R)} = \frac{k_{AB} t_1 w}{\sin(\phi) \cos(\theta_R)} \quad (3.5)$$

Using the constitutive model of the work material, average shear stress, k_{AB} , occurring at the shear plane (AB) is estimated as a function of average strain, γ_{AB} , strain rate, $\dot{\gamma}_{AB}$, and temperature, T_{AB} , of the shear zone.

Average shear strain, γ_{AB} , is a function of cutting tool rake angle, α , and shear angle, ϕ , as

$$\gamma_{AB} = \frac{\cos(\alpha)}{2 \sin(\phi) \cos(\phi - \alpha)} \quad (3.6)$$

Average strain rate, $\dot{\gamma}_{AB}$, at the parallel-sided thick shear zone is a function of the primary deformation zone thickness ratio, C' , shear plane deformation speed, V_S , and shear plane length, l , as

$$\dot{\gamma}_{AB} = \frac{C' V_S}{l} \quad (3.7)$$

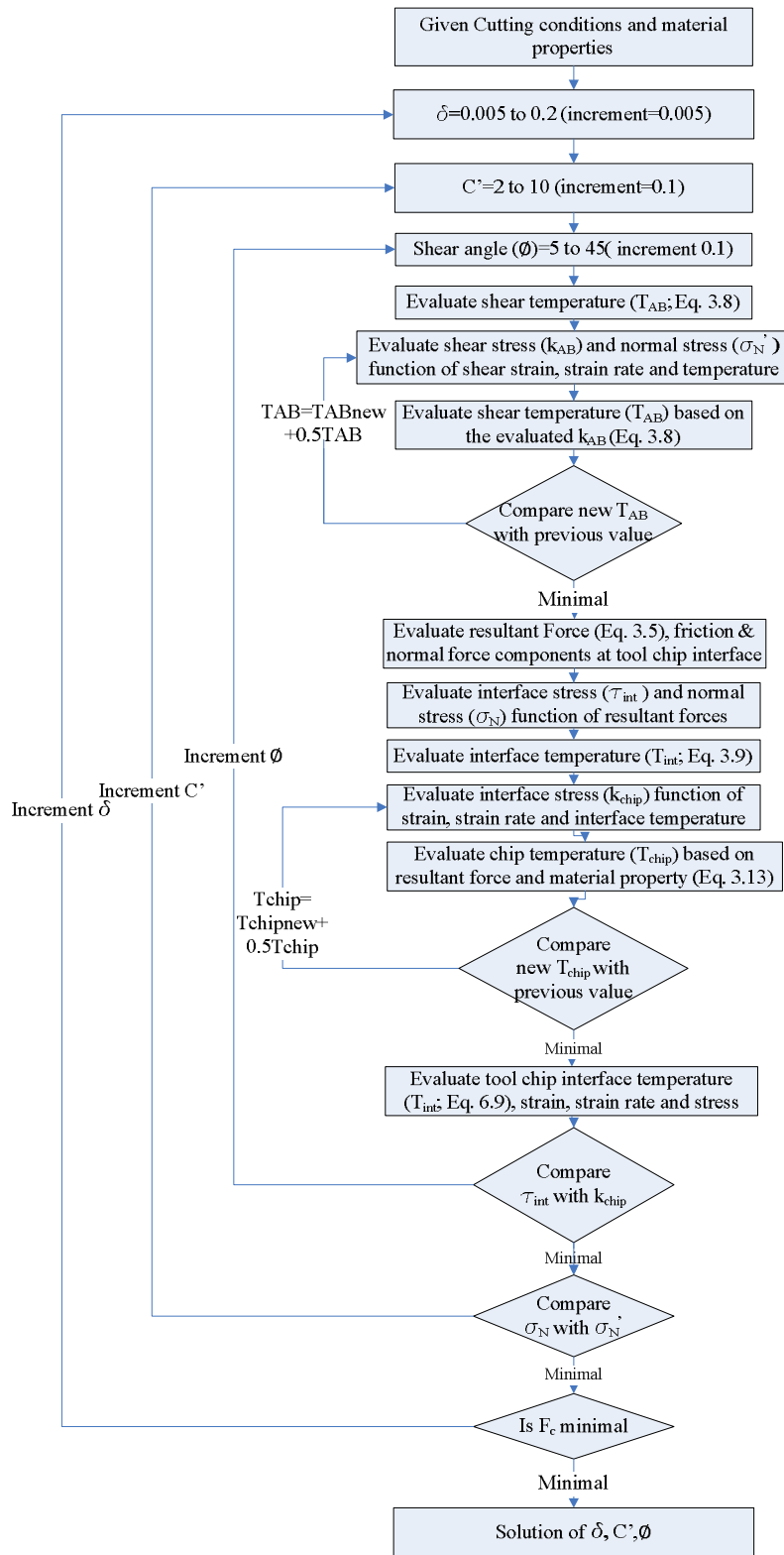


Figure 3.4 Flow chart for the shear zone solution following Oxley [30]

Average machining temperatures along the primary shear zone, T_{AB} , and secondary (tool chip interface) zone, T_{int} , are evaluated utilizing Boothroyd [31]

$$T_{AB} = T_w + \eta \frac{(1-\beta_T)F_s \cos\alpha}{\rho_d C_p t_1 w \cos(\theta-\alpha)} \quad (3.8)$$

$$T_{int} = T_w + \frac{(1-\beta_T)F_s \cos\alpha}{\rho_d C_p t_1 w \cos(\theta-\alpha)} + \psi \Delta T_m \quad (3.9)$$

Where T_w is the initial work temperature, $\eta=0.7$ is a factor accounting for plastic deformation occurring outside the shear zone utilized by Oxley [30]. ΔT_m is the maximum temperature rise in the chip, and the factor ψ defining the tool chip heat partition ratio adopted with a value of 0.6 inline with Lalwani et al. [19].

The density and specific heat of the work material are ρ_d and C_p , respectively. The term β_T is the proportion of heat conducted into the work and is estimated using the Boothroyd [31] empirically determined equations

$$\beta_T = 0.5 - 0.35 \log(R_T \tan\phi) \text{ for } 0.04 < R_T \tan\phi < 10 \quad (3.10)$$

$$\beta_T = 0.3 - 0.15 \log(R_T \tan\phi) \text{ for } R_T \tan\phi > 10 \quad (3.11)$$

with R_T being a non-dimensional thermal number function of density, ρ_d , specific heat, C_p , cutting speed V , uncut chip thickness, t_1 , and workpiece thermal conductivity, K .

$$R_T = \frac{\rho_d C_p V t_1}{K} \quad (3.12)$$

The ratio of the average (ΔT_c) to maximum (ΔT_m) chip temperature rise is defined Boothroyd [31] as

$$\log\left(\frac{\Delta T_m}{\Delta T_c}\right) = 0.06 - 0.195 \delta \left(\frac{R_T t_2}{h}\right)^{0.5} + 0.5 \log\left(\frac{R_T t_2}{h}\right) \quad (3.13)$$

Where $\delta = S_2/t_2$ is the secondary deformation zone thickness ratio, t_2 the chip thickness shown in Figure 3.3, R_T the non-dimensional thermal number Eq. (3.12), ΔT_c is the average chip temperature rise by Oxley[42]

$$\Delta T_c = \frac{P \sin(\phi)}{(\rho C_p t_1 w \cos(\phi - \alpha))} \quad (3.14)$$

and h is the tool/chip contact length as presented by Oxley [42] following Eq. 3.15 by satisfying the condition that the moment of the normal force about the tool nose point equals the moment of the resultant force along plane AB.

$$h = \frac{t_1 \sin \theta}{\cos \lambda \sin \phi} \left[1 + \frac{C' n'}{3(1 + 2(\pi/4 - \phi) - C' n')} \right] \quad (3.15)$$

The force components F_c , F_T , P , N (Figure 3.3) are determined by Stabler [41] as a function of the resultant force, RF , cutting rake angle, α , and friction angle, λ , at the δ , C' , and ϕ iteration as described in Figure 3.4. For each combination value for δ , C' , a solution for the shear angle, ϕ , is found for the corresponding shear angle that provides equilibrium between resultant forces transmitted through the shear plane and the chip tool interface forces where $\tau_{int} = k_{chip}$ condition is satisfied. The shear stress generated by friction forces at the tool /chip interface, τ_{int} , is estimated based on dividing the cutting tool friction force (P) by the tool chip contact area ($h \cdot w_c$) where h is the tool chip contact length Eq. (3.15) and w_c is the chip width. The term k_{chip} is calculated using material flow stress model of

$$\sigma = \sigma_1 \epsilon^{n'} \quad (3.16)$$

based on the chip's strain velocity-modified temperature occurring at the tool/chip interface secondary deformation zone. The terms σ_1 , ϵ , and n' are material effective stress,

effective strain, and material-specific temperature-modified strain hardening exponent, respectively.

For each δ value, Figure 3.4 illustrates the solution of the primary deformation zone thickness ratio, C' , which is found when the condition of $\sigma'_N = \sigma_N$ is met. The term σ_N is the uniform normal stress at the chip tool interface based on calculated cutting tool normal force, N , and the tool-chip contact area ($h \cdot w_c$).

The normal stress, σ'_N , is determined using stress boundary at point B (Figure 3.3) function of material stress at the shear plane, k_{AB} , rake angle, α , and the temperature modified strain hardening index n' as reported by Oxley [42] where the normal stress at the tool-chip interface is found from the stress boundary condition at B by working from A along AB, and it can be expressed as

$$\sigma'_N = k_{AB} \left(1 + 0.5\pi - 2\alpha - 2 \left(\frac{\delta k}{\delta s_1} \right) \frac{1}{2k_{AB}} \right) = k_{AB} (1 + 0.5\pi - 2\alpha - 2C'n') \quad (3.17)$$

Considering the plastic zone caused by friction work at the tool/chip interface and assuming that the thickness S_2 of the secondary deformation zone is determined from minimum work principle, secondary deformation zone thickness ratio, δ , is obtained for the case where a combination of strain rate and temperature results in minimum value of cutting force, F_c .

The combined solution for d , C' , and ϕ is found for the case where values meet the criteria simultaneously described by (Figure 3.4)

- 1- Minimum K_{chip}
- 2- $\sigma'_N = \sigma_N$
- 3- $\tau_{int} = k_{chip}$

Oxley [30] validated the thick shear zone model by comparing his findings against orthogonal cutting experiments employing 0.2% and 0.38% carbon steels. To corroborate our findings, Oxley's results were replicated with near-perfect match and are reported in the supplementary Tables S-1-a, and S-1-b (Appendix 1).

2. Extending Shear Zone Formulation for JC-Type Constitutive Equation (e.g., Al 6061-T6)

In order to utilize Oxley thick shear zone approach using standard material models reported in literature such as formulation presented by Johnson and Cook [18], in his work Lalwani et al. [19] conceived a methodology that uses Johnson Cook Material model to substitute the use of Oxley Power form material model along with the velocity-modified temperature term, T_{mod} , defined as

$$T_{\text{mod}} = T[1 - 0.09\log(\dot{\epsilon})] \quad (3.18)$$

The temperature modified term T_{mod} was initially advanced by Oxley [30] to account for combined strain rate ($\dot{\epsilon}$) and temperature, T , effects on material properties. Utilizing low carbon steel, high order curve-fitting equation was used to describe the relation between T_{mod} and both uniaxial flow stress, σ_0 at $\epsilon=1$, and the strain hardening index, n' , where shear stress is expressed as

$$k = \frac{\sigma_0 \epsilon^{n'}}{\sqrt{3}} \quad (3.19)$$

In his work, Lalwani et al. [19] extended Oxley [13] thick shear zone model by utilizing a material flow stress model of the JC form. The extension follows the algorithm described in the

flowchart in Figure 3.4 and substitutes the need for modified temperature, T_{mod} , by introducing a strain-hardening exponent parameter

$$n_{\text{eq}} = \frac{nB\varepsilon_{AB}^n}{A+B\varepsilon_{AB}^n} \quad (3.20)$$

where A, B, and n are the JC parameters and ε_{AB} is the shear plane strain.

Having discarded strain rate modified temperature, the JC material model is now available to accommodate utilizing strain, strain rate, and temperature as independent parameters. Solutions for δ , C' , and ϕ are then found using the convergence criteria described in section 3.3.1. For validation of the numerical code of this module, the comparison is made between the cutting forces predicted by the extended shear zone utilizing JC constitutive formulation and results reported by Lalwani et al. [19] corresponding to the same cutting conditions and work material (0.38% carbon steel). Values generated of the cutting force components in the velocity direction (F_t) and thrust force (F_{feed}) are found to be in good agreement with cutting force values reported by Lalwani et al. [19] as summarized in the supplementary Table S-2 (Appendix 1).

3. Oblique cutting Model (based on Lin [40])

In order to utilize the JC extended shear zone approached advanced by Lalwani et al. [19] in modeling three dimensional drilling forces, analytical transformation from 2D orthogonal forces to oblique 3D oblique forces is necessary. Lin [40] developed kinematical and geometrical transformations allowing for extending the thick shear zone orthogonal model application for oblique cutting. The flow chart in Figure 3.5 illustrates the logic of this development.

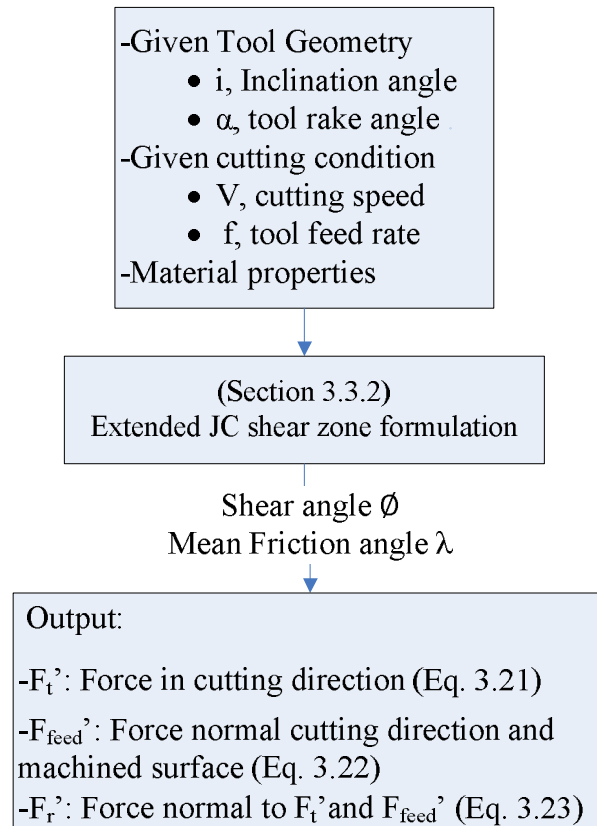


Figure 3.5. Oblique cutting model based on the shear zone formulation Lin [40]

The analysis considers the chip flow in the plane normal to the cutting edge as

orthogonal (plain strain) flow. The oblique machining processes may then be divided into two simultaneous steps

- Orthogonal cutting in the tool normal plane.
- Chip sliding and shearing in a direction parallel to the cutting edge.

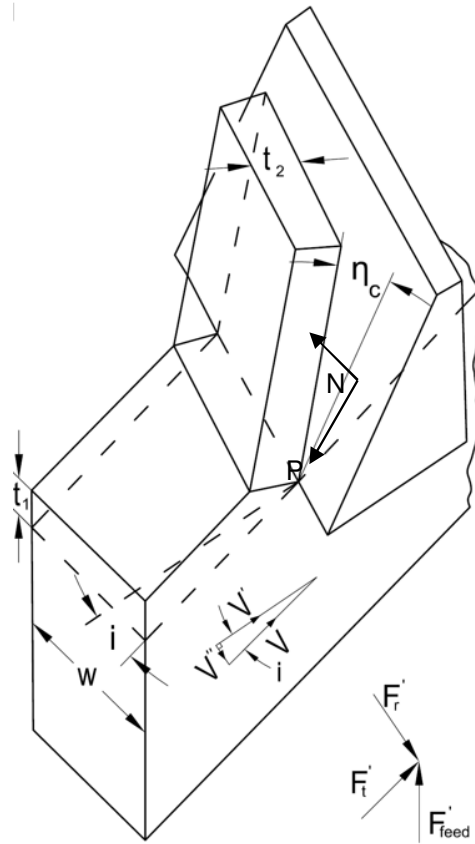


Figure 3.6. Oblique cutting parameters and force components Lin [40]

Shown in Figure 3.6, cutting velocity (V) is resolved into two components in terms of tool inclination angle, i , $V' = V \cos(i)$ and $V'' = V \sin(i)$ being velocity components normal and parallel to the cutting edge, respectively. Force components F_t , F_{feed} , and P are the cutting force, thrust force, and friction force components in the tool normal plane, respectively, are calculated based on extended shear zone formulation described in section 3.3.2.

Based on geometrical relations, the oblique forces including oblique cutting force, F'_t , oblique thrust force, F'_{feed} , and F'_r force components normal to F'_t and F'_{feed} are denoted in Figure 3.6 and defined respectively in equations 3.21, 3.22, and 3.23 as

$$F'_t = F_t \cos(i) + P \tan(\eta_c) \sin(i) \quad (3.21)$$

$$F'_{\text{feed}} = F_{\text{feed}} \quad (3.22)$$

$$F'_r = F_t \sin(i) - P \tan(\eta_c) \cos(i) \quad (3.23)$$

The chip flow angle, η_c , is determined by Stabler [41]

$$\tan(\eta_c) = \frac{\tan(i)\cos(\alpha)}{\tan(\phi+\lambda)} + \sin(\alpha)\tan(i) \quad (3.24)$$

as a function of geometric features consisting of the rake angle, α , inclination angle, i , and cutting conditions dependent feature consisting of shear angle, ϕ , mean friction angle along the tool chip interface, λ .

4. Extended JC Shear Zone Approach Applied To Drill Cutting Lip Force Prediction

Having adopted the Lin [40] orthogonal to oblique force transformation, identifying the drill bit cutting lip varying obliquity parameters become necessary for cutting lip force estimation. Figure 3.7(a, b) shows the salient features of the classical twist drill, where the chisel edge is located at the drill's center with width, $2W$, and helical cutting lips having a point angle, $2p$, that meets the drill bit flute at a helix angle, β_0 . For calculating cutting forces at the drill cutting lip, Williams [1] and Wiriyacosol and Armarego [2] subdivided the cut material into a finite series of discrete elements (each representing an oblique cut) with common chip flow direction. Each element is associated with characteristic cutting speed, web angle, local helix angle, inclination angle, rake angle, and non-dimensional radial coordinate, ρ , defined as the ratio of drill lip elemental radius r divided by the drill bit radius, R , as

$$\rho = \frac{r}{R} \quad (3.25)$$

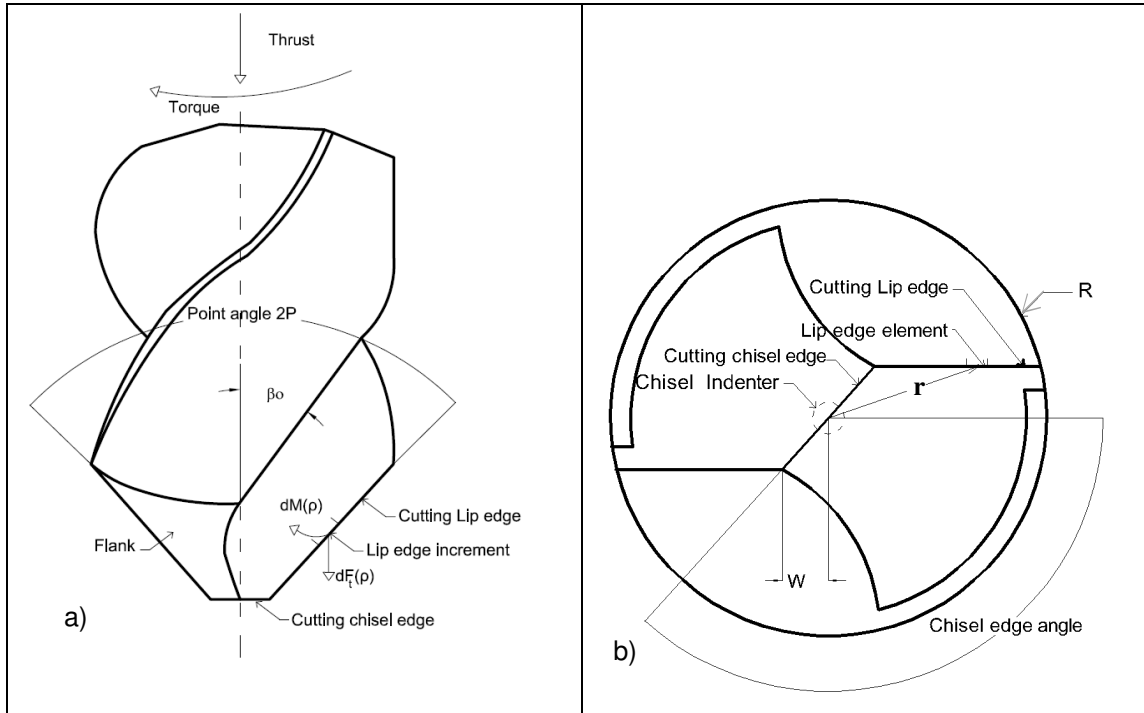


Figure 3.7 Features and geometry of the cutting point of the traditional chisel drill (a) front view, (b) and top view.

The cutting speed along the lip is a function of rotational speed, ω , and varies as a function of normal radius

$$V(\rho) = \omega R \rho \quad (3.26)$$

Web angle, $\theta(\rho)$, is related to w , R , and ρ as

$$\theta(\rho) = \sin^{-1} \left(\frac{w}{R\rho} \right) \quad (3.27)$$

Local helix angle, $\beta(\rho)$, is a function of nominal helix angle β_0 and ρ

$$\beta(\rho) = \tan^{-1}(\rho \tan(\beta_0)) \quad (3.28)$$

The oblique cutting angle, $i(\rho)$, varies along the lip and defined as the angle formed between the cutting velocity and the normal to the cutting edge velocity (Pal et al., 1965) as related to drill bit half-point angle (p) and to $\theta(\rho)$ as

$$i(\rho) = \sin^{-1} \left(\sin(p) \sin(\theta(\rho)) \right) \quad (3.29)$$

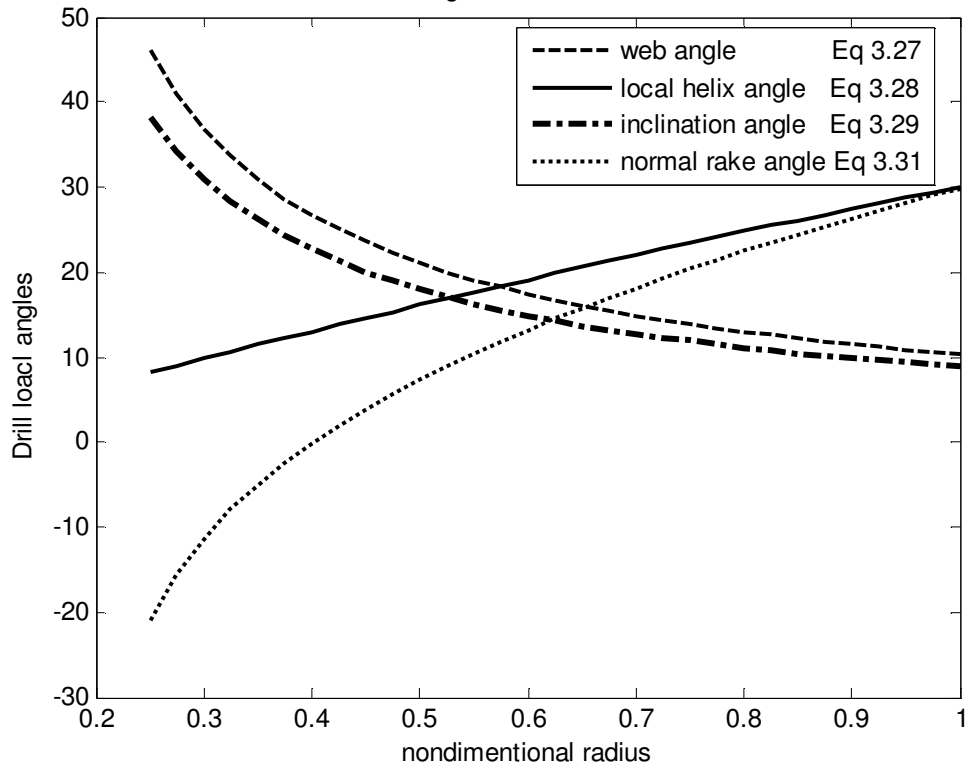


Figure 3.8. Variations of the geometric angles along the cutting lip as function of non-dimensional radius

Measured in a plane normal to the cutting edge, the effective rake angle, α_f , is defined as Shin and Waters [43] the angle between the plane parallel to the drill axis containing cutting edge and the plane tangent to the flute face at the cutting edge as

$$\alpha_f(\rho) = \tan^{-1} \left(\frac{\tan(\beta(\rho)) \cos(\theta(\rho))}{\sin(p) - \tan(\beta(\rho)) \cos(p) \sin(\theta(\rho))} \right) \quad (3.30)$$

Normal rake angle is described by

$$\alpha_n(\rho) = \alpha_f(\rho) - \gamma_d(\rho) \quad (3.31)$$

where the angle $\gamma_d(\rho)$ results from projecting the velocity vector onto the normal plane and is determined from

$$\gamma_d(\rho) = \tan^{-1} \left(\tan(\theta(\rho)) \cos(p) \right) \quad (3.32)$$

Figure 3.8 illustrates the variations of the salient geometric angles as a function of non-dimensional radius along the drill bit cutting lip edge as predicted by equations 3.27, 3.28, 3.29 and 3.31. Cutting action is more efficient at the lip margin where large positive rake angle and higher cutting velocities coincide contrary to the region adjacent to the chisel edge where concurrent negative rake angle and low cutting velocity reduces cutting efficiency. Taking advantage of the geometric tool variability along the drill lip, Hamade et al.[3] successfully extracted material-specific cutting force parameters for Aluminum 6061-T6. The different geometric lip parameters are defined and are then combined with modified oblique cutting thick shear zone approach (as described in Section 3.3.3) based on Lalwani et al. [19] extended Oxley [13] thick shear zone approach ((Section 3.3.2).

Estimates of incremental torque $dM(\rho)$ and incremental thrust force values $dF_t(\rho)$ become possible as a function of lip incremental edge oblique cutting force (F'_t), oblique thrust force (F'_{feed}) and F'_R force components normal to F'_t and F'_{feed} components as

$$dM(\rho) = \rho R F'_t(\rho) \quad (3.33)$$

$$dF_t(\rho) = F'_{feed}(\rho) \sin(p) - F'_R(\rho) \cos(p) \quad (3.34)$$

Illustrated in Figure 3.9 is the incremental force prediction coding flowchart, according to Williams [1].

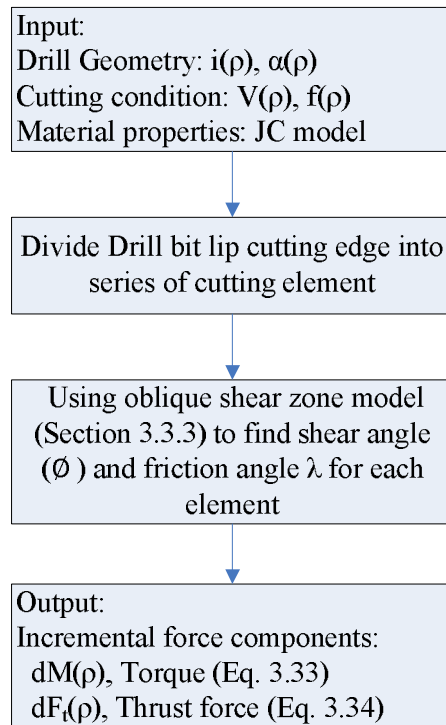


Figure 3.9. Lip force prediction module Williams [1].

D. Determining the Johnson-Cook Equation Parameters for Al 6061-T6

Having developed a drill bit Drill Cutting Lip Force Prediction based on the material model and drilling condition described in section 3.3.4; Presented is to update material model parameters by matching DLCFPM prediction lip torque versus experimentally collected lip torque reported in section 3.4. The DLCFPM numerical (MATLAB®) code divides the lip into a series of cutting edges (segments) with variable geometric cutting conditions. Assigned to each segment are individual geometric attributes (Table 3.2) and cutting parameters (e.g., cutting speed and uncut chip thickness). Considering drilling parameters (Table 3.1) and utilizing the combined extended JC shear zone module with JC parameters (Section 3.3.3), cutting forces were determined along the lip for 2.5mm, 3.5mm, 5.5mm, 7.5mm pre-cored-holes. As the code runs and the lip progressively engages the pre-cored work, JC parameters are automatically

adjusted (Figure 3.1) to minimize the difference between the predicted and measured torque values according to

$$\min \left[\sqrt{\sum \left((M(\rho)_{\text{measured}} - M(\rho)_{\text{predicted}})^2 \right)} \right] \quad (3.35)$$

Curve fitting is done using a custom MATLAB® code based on a nonlinear least-squares optimization tool with a convergence criterion of 10⁻⁹ and a maximum iteration number of 1000. For a defined search range, the optimization code identifies parameters that meet the global minimum criteria for the objective function Eq. (3.35) by establishing global and local quadratic convergence targets.

Table 3.4. Ranges, initially assigned values, and optimized JC parameter values.

JC Parameters		A	B	C	n	m
Searching range	Lower limit	290	90	0.0005	0.3	1.1
	Upper limit	350	140	0.004	0.6	1.4
Case #1	Initializing parameters from Johnson et al., (1994)	324	114	0.002	0.42	1.34
	Found parameters	317.54	108.90	0.0015	0.43	1.29
Case #2	Random initial parameter values	350	100	0.001	0.4	1.2
	Found parameters	317.54	108.91	0.0015	0.43	1.29
Case #3	Random initial parameter values	270	130	0.005	0.2	1.2
	Found parameters	317.53	108.89	0.0015	0.43	1.29
Case #4	Random initial parameter values	100	400	1	0	2
	Found parameters	317.54	108.91	0.0015	0.43	1.29

The top rows in Table 3.4 list the lower and upper limits for the searching range for the five JC parameters: A, B, C, n, and m. Also reported in Table 3.4 are the results of four run cases (case #1 through #4) utilized while DLCFPM searches for the optimum JC parameters. For the control case #1, the values for the five parameters reported by Johnson et al. [36] for Aluminum

6061-T6 are used as initial parameters. For cases #2, 3, and 4, used were randomly assigned initial sets of JC parameters.

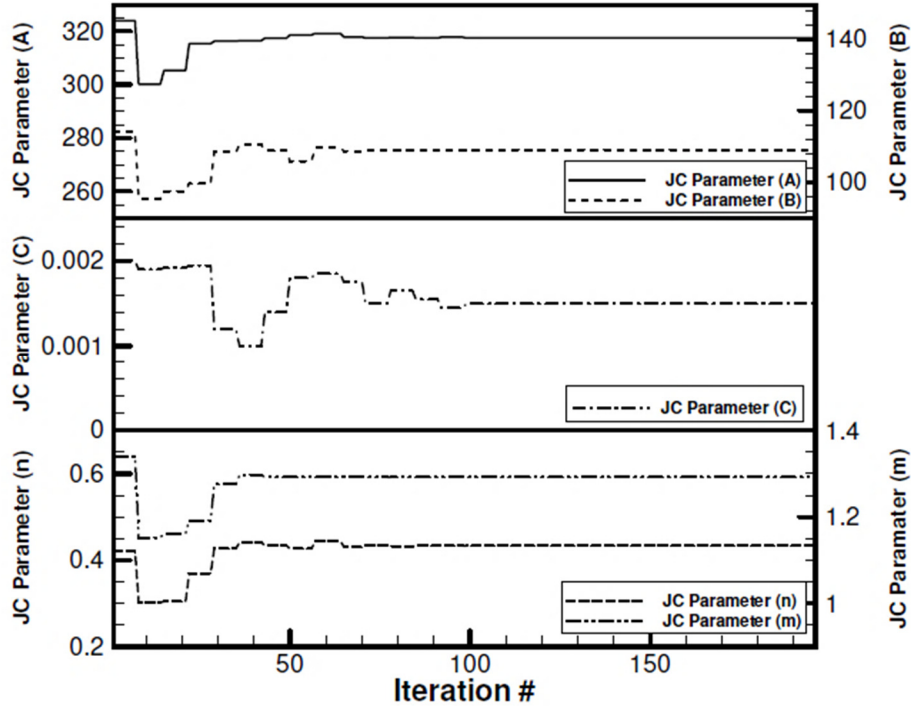


Figure 3.10. Conversion histories of the Equation 3.1, JC parameters A, B, C, n, and m versus iteration number.

Utilizing Eq. (3.35) with the searching ranges subject to the convergence criteria, the DLCFPM methodology converged to one set of parameter values for the five JC parameters A, B, C, n, m of 317.54, 108.90, 0.0015, 0.43, 1.29, respectively. These optimal JC parameter values resulted in numerical cutting forces profiles that duplicate the experimentally recorded data (Figures 3.13,3.15).

It is worth noting that changing the convergence parameters would induce minor changes in the results. In addition, using initializing values from outside this range would induce changes in these results. As compared to the control case and although converging to the same set of parameters, other runs did so at increased computational cost (time). Shown in Figure 3.10

are typical conversion histories of the five (5) JC parameters, A, B, C, n, and m versus iteration number (case #1). shown in Figure 3.10

E. Validation of Methodology Using FEM Simulations

In order to validate the effectiveness of the newly found JC parameters, the updated material model has been utilized to predict cutting forces using finite element simulations. Matching with the said target FEM (using DEFORM® software) simulations utilizing an updated JC material model for workpiece characterization, were produced as replicas of the drilling experiments (Table 3.3) of pre-cored holes of 2.5 mm, 3.5 mm, 5.5 mm, and 7.5 mm.

1. FEM model setup

The chisel point drill (Table 3.2) and the pre-cored cylindrical workpieces were digitally replicated using 3D CAD and the geometry imported into the preprocessor of DEFORM®. Workpiece geometry with the pre-cored pilot hole (3.5 mm diameter) is shown in Figure 3.11(a). Outer and pre-cored hole diameter dimensions of the model workpiece are selected to match the dimensions of the actually tested workpieces while the digital model workpiece thickness is designed to be 10mm larger than twice the drilling depth making the workpiece thick enough for accurate cutting force FEM calculation without increasing the computation time. Tetrahedral elements were used for mesh generation with an aspect ratio of 7 and maximum size equal to 30% of the feed. The workpiece was meshed using 17354 elements with a minimum element size of 0.00014 mm. The tool was meshed with 14354 elements of a minimum element size of 0.005 mm. DEFORM® uses adaptive re-meshing to continuously update the mesh as it deforms. Boldyrev et al. [44] demonstrated the applicability of the JC type material model for cutting

processes via FEM numerical modeling. The JC Al6061-T6 material parameters are considered as those found in Table 3.4.

Contact conditions between the drill tool and workpiece control the friction and heat transfer at the interface between the two bodies. Based on DEFORM® recommendations, a sticking-friction criterion of 0.55 was adopted. To ensure stable simulation, a time step of 10^{-6} s was utilized. Material separation is controlled by DEORM® by mesh element split, which occurs when the element reaches a critical plastic strain value.

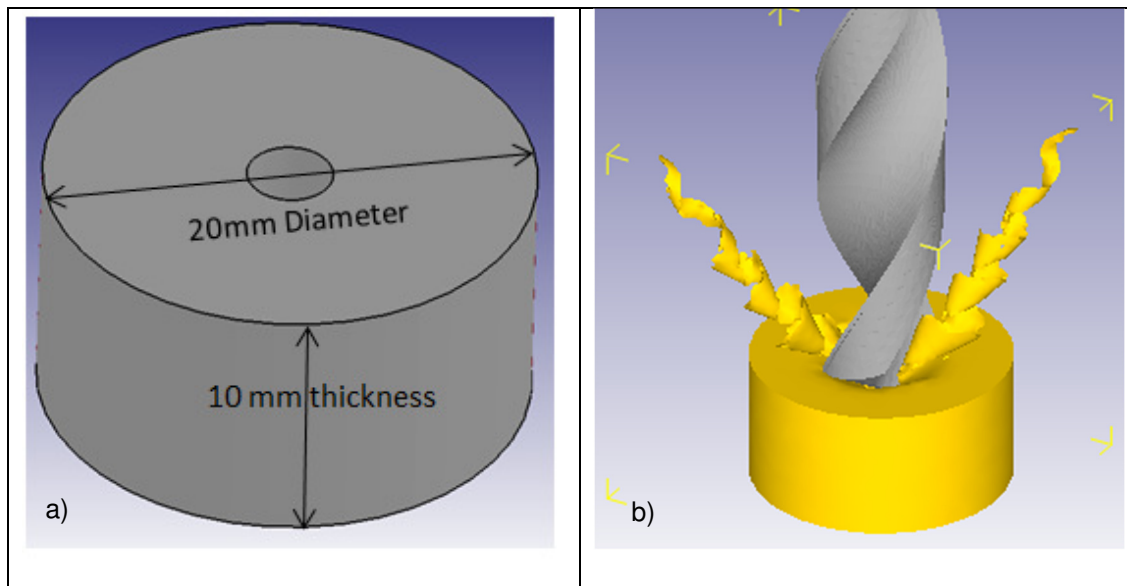


Figure 3.11. Workpiece a) showing the pre-cored pilot hole and b) while being drilled in FEM (showing chip generation).

2. FEM results

Matching with experimental set up reported in section 3.2, drilling simulations were conducted on workpieces with pre-cored holes of 2.5mm, 3.5mm, 5.5mm, and 7.5mm up to a drilling depth of 4 mm, ensuring full lip engagement. Figure 3.11(b) shows the generated chip in the drilling simulation run on DEFORM® for a 3.5mm pre-cored workpiece.

Figures 3.12 (a-d) are plots of temperature, effective stress, strain, and strain rate, respectively, for the 2.5 mm pre-cored workpiece simulation (rotational speed of 9868 rpm and feed of 0.64 mm/revolution). The maximum values of effective stress and temperature are about 476 MPa and 434 °C, respectively, occurring at the tool-chip interface (FEM-generated torque and thrust profiles are reported in Figure 3.13).

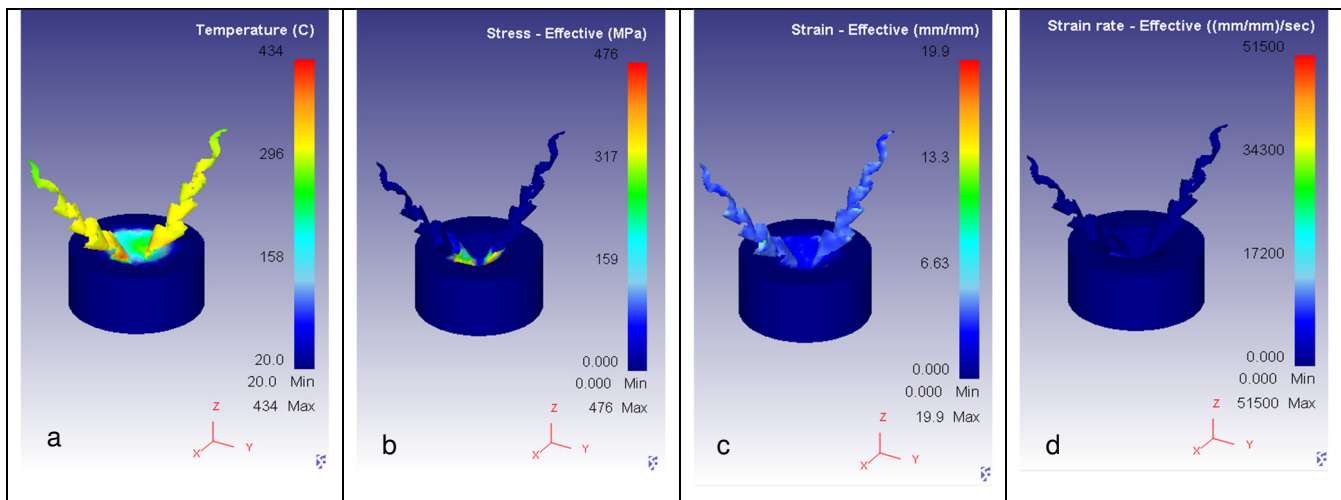
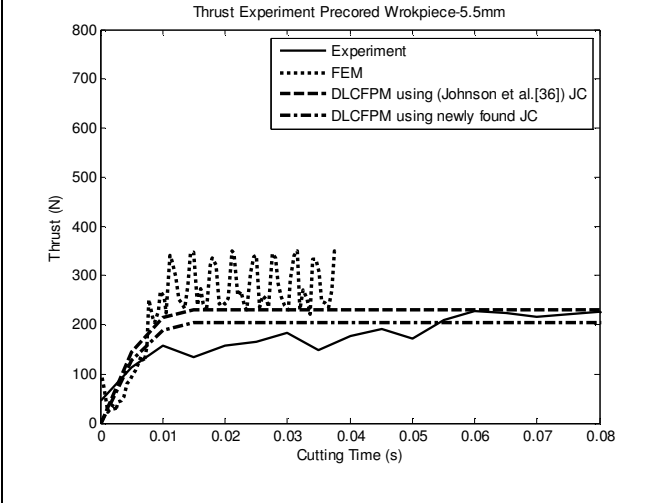
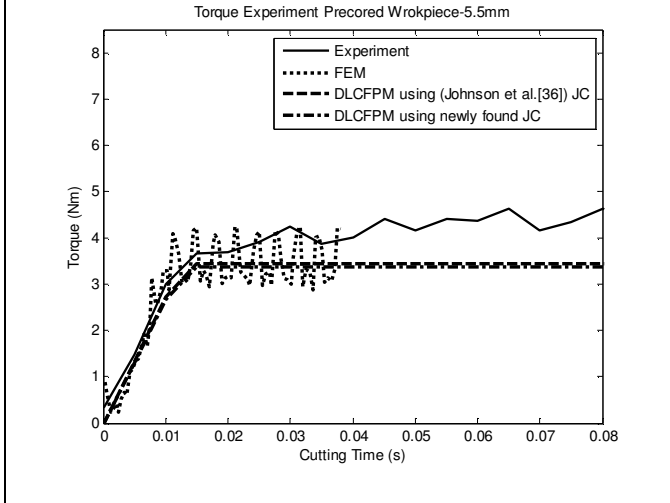
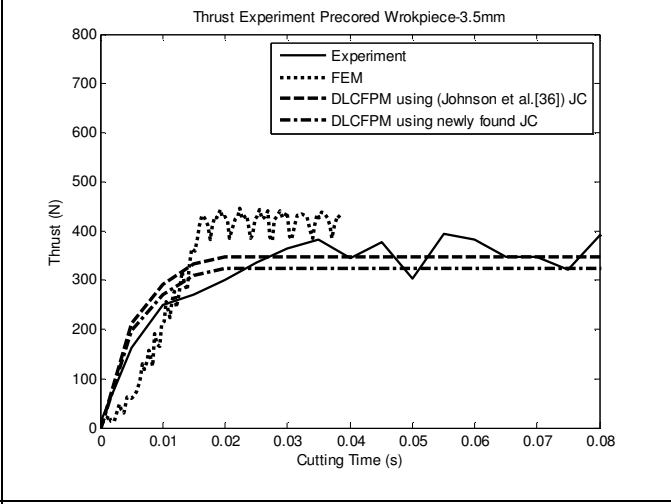
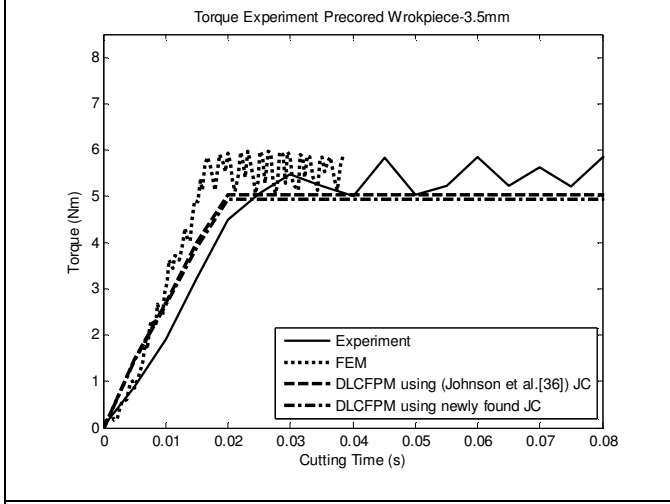
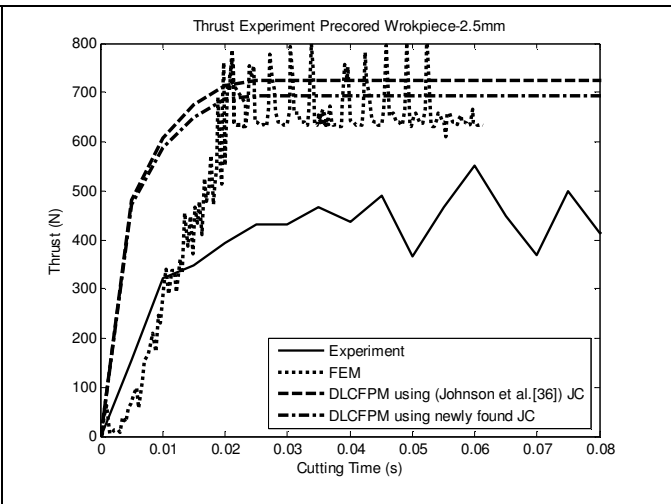
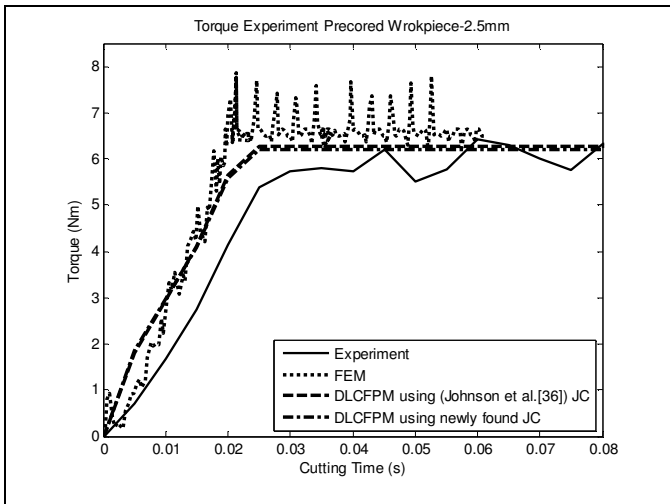


Figure 3.12. FEM results for plots of (a) temperature, (b) effective stress, (c) strain, and (d) strain rate for the 2.5 mm pre-cored workpiece simulation (rotational speed of 9868 rpm and feed of 0.64 mm/revolution).

F. Comparison of the Drill Lip Cutting Force Prediction Methodology versus FEM and Experimental Drilling Measurements

Aiming to report the improved performance of developed DLCFPM using the newly found JC parameter in modeling drilling forces reported in Figure 3.13 plots of torque and thrust force evolution profiles (spindle speed 9868 rpm, tool feed = 0.64mm/rev) generated methodology for 2.5 mm, 3.5 mm, 5.5 mm, and 7.5 mm pre-cored holes.



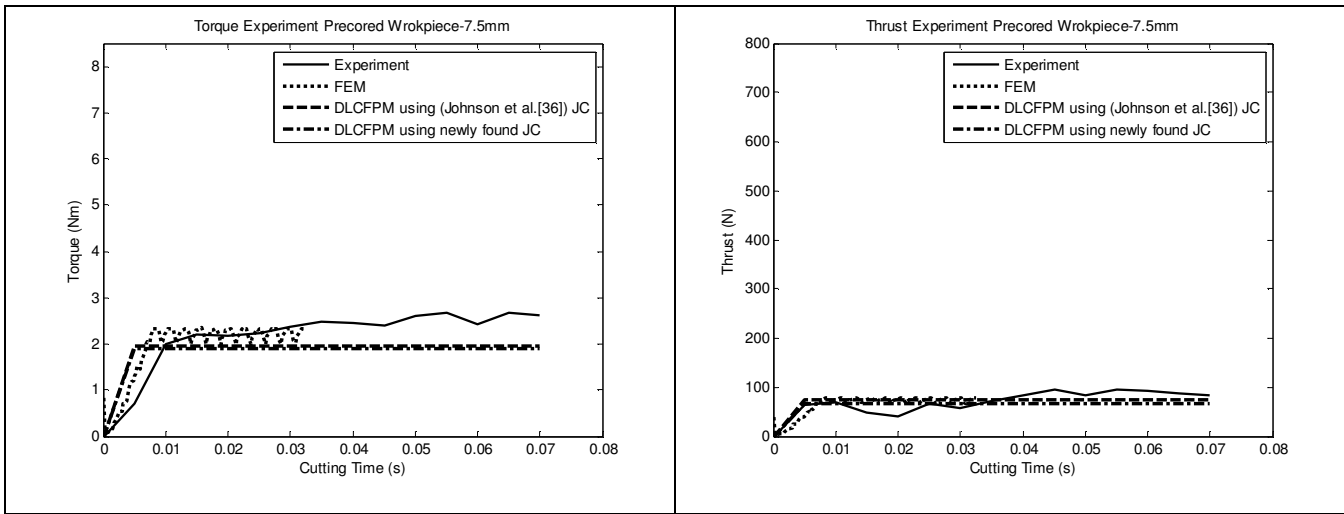


Figure 3.13. Comparative plots of (L) torque and (R) thrust force profiles generated by DLCFPM and compared to experiments and FEM (spindle speed 9868 rpm, tool feed = 0.64mm/rev). From top to bottom pre-cored holes = 2.5 mm 3.5 mm, 5.5 mm, and 7.5 mm, respectively.

These numerical results are compared versus the results of FEM simulations and experiments for the same cutting parameters. DLCFPM-predicted profiles are calculated two ways: once employing JC flow stress parameters Aluminum 6061-T6 as reported by Johnson et al. [36] and another using the JC parameters found (317.54, 108.90, 0.0015, 0.43, and 1.29 for A, B, C, n, and m, respectively). These profiles show good agreement against each other and against the FEM simulations results and with the experiments.

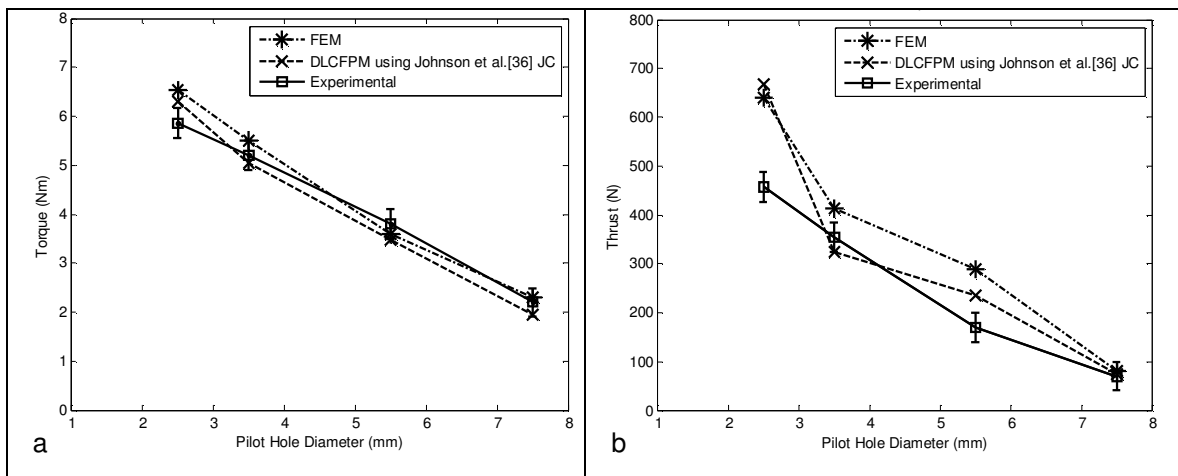


Figure 3.14. Full engaged lip (a) Torque and (b) Thrust force results for experimental, FEM, and DLCFPM numerical results at varying pre-cored diameter results

Plotted in Figures, 3.14(a) and (b) are torque and thrust force values, respectively, recorded at full lip engagement versus pilot hole diameter in pre-cored holes of 2.5mm, 3.5mm, 5.5mm, and 7.5mm. The data include the torque and thrust profiles (Figure 3.13) collected from experimentally recorded forces, FEM, DLCFPM simulation results for reference (Johnson et al.,1994) JC, and JC parameters found at performed drill bit tool feed of 9868 rpm and 0.64 mm/rev. For the experimental torque and thrust shown are error bars with respect to the arithmetic mean of conducted repeated experimental tests using t-student distribution at a 95% confidence interval. Figure 3.14 shows good agreement between the developed methodology and FEM simulation generated lip incremental torque and thrust forces. Observed is a deviation from the experimental thrust force value for a pilot-hole of 2.5 mm. The reason of the combined effect of high negative rake angle and slow cutting speed involved, caused deviation from the thick shear zone approach utilized to generate DLCFPM cutting forces.

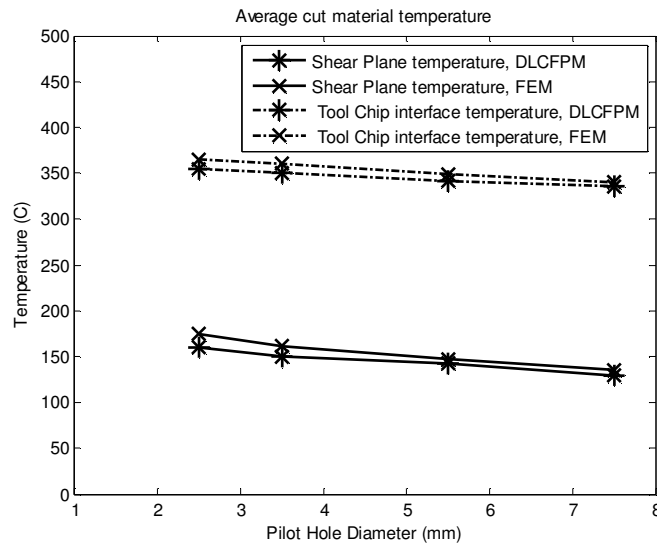
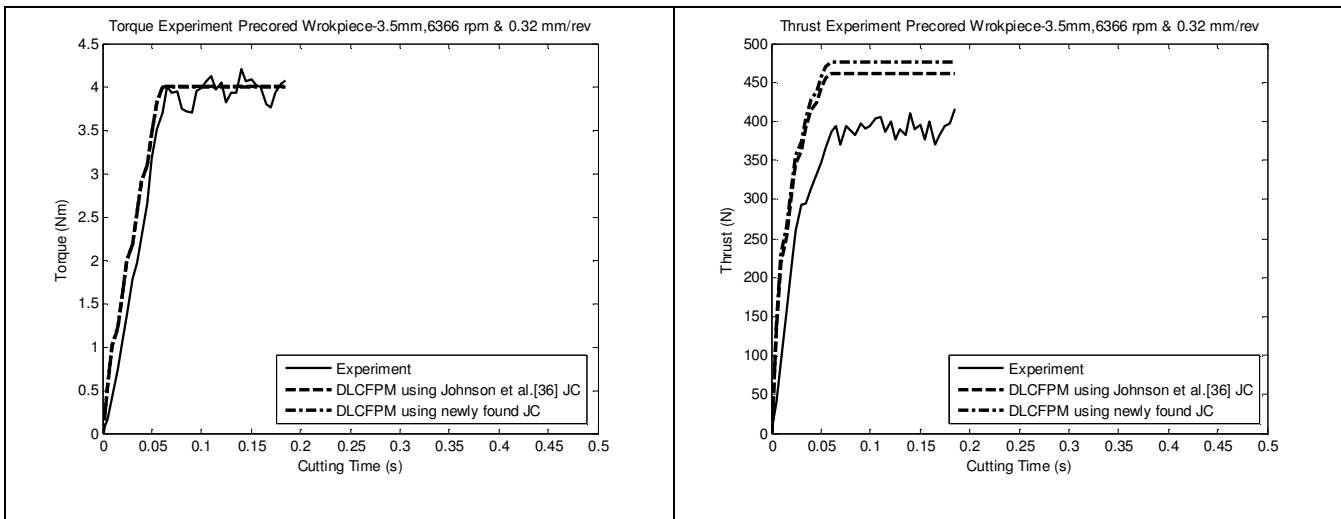


Figure 3.15. Shear plane and tool-chip interface temperatures: DLCFPM versus FEM results reported at (rotational speed of 9868 rpm and feed of 0.64 mm/revolution).

For the same cutting parameters used to produce Figures 3.13 and 3.14, Figure 3.15 plots values from DLFPM's using JC parameters found from calculated average shear plane temperature (T_{AB}) and tool-chip interface temperature (T_{int}) versus pilot hole diameters of 2.5mm, 3.5mm, 5.5mm, and 7.5mm. Temperature values were recorded at full lip engagement with the workpiece.

Co-plotted in Figure 3.15 are average shear plane (T_{AB}) and tool-chip interface temperature (T_{int}) found by FEM simulations and DLCFPM using the newly found Al 6061-T6 JC parameters. The FEM values are determined by averaging found temperatures for nodes constituting the relevant primary and secondary deformation zones. While drilling pilot holes of diameter 2.5 mm and 7.5 mm, shear plane temperatures decreased from 176 °C to 133 °C while average tool-chip interface temperatures decreased from 365 °C to 328 °C. As cutting action approaches the drill bit outer diameter, the effective rake angle of the engaged lip becomes more positive (Figure 3.8), leading to more effective cutting.



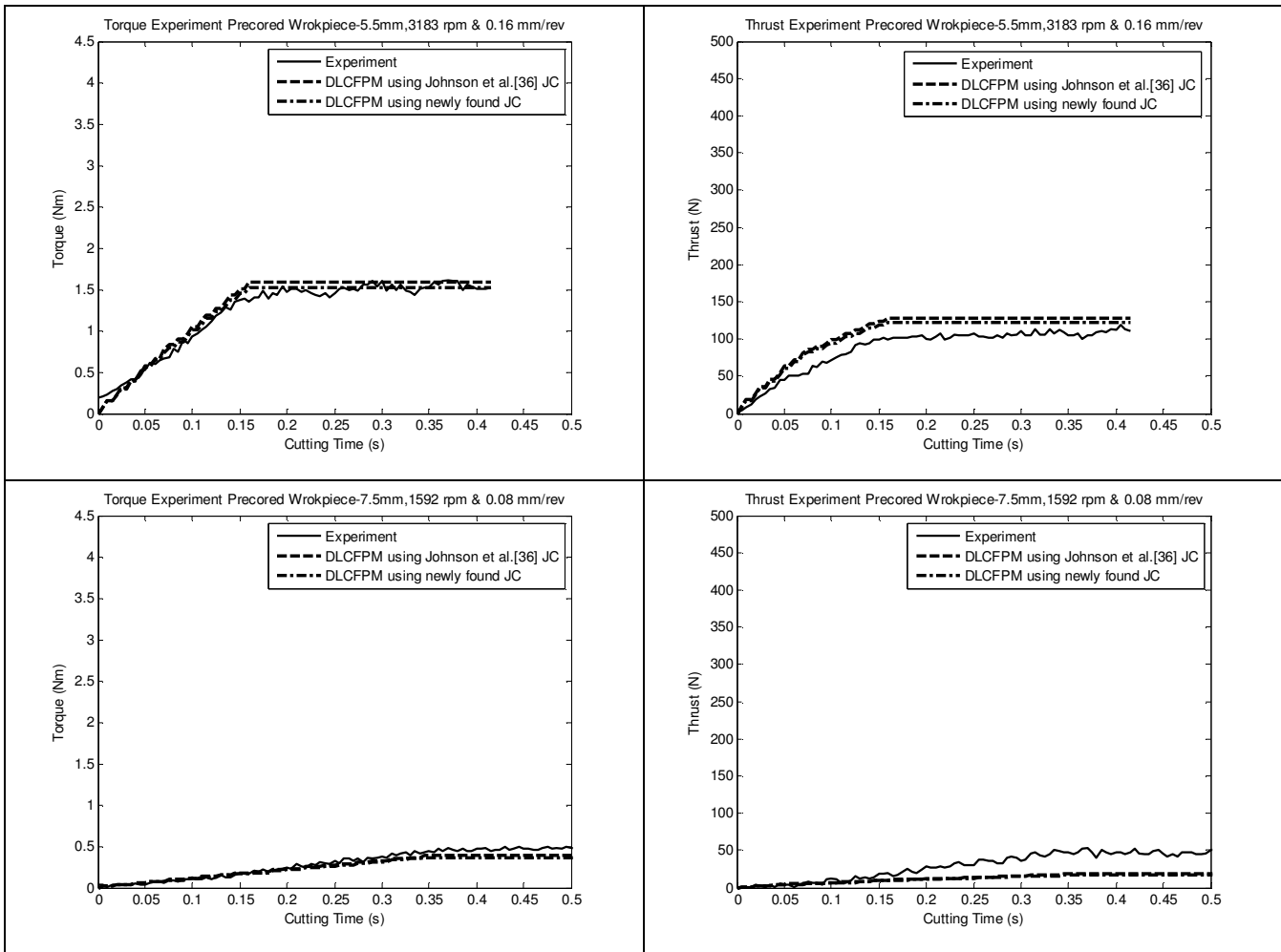


Figure 3.16. Comparative plots of (L) torque and (R) thrust force profiles generated by DLCFPM and compared to experiments and FEM. Drilling parameters of pre-cored hole diameter, spindle speed, and tool feed rate are: (top) 3.5 mm, 6366 rpm, 0.32 mm/rev, (middle) 5.5 mm, 3183 rpm, 0.16 mm/rev, and (bottom) 7.5 mm, 1592 rpm, 0.08 mm/rev.

G. Summary and Conclusions

Based on Oxley's extended thick shear zone formulation, developed is a methodology dubbed the Drill Lip Cutting Force Prediction Methodology (DLCFPM). The methodology implemented utilizing a custom-written code is applied to extract optimized Johnson-Cook (JC) flow stress parameters from a small number of drilling experiments. As application to the current methodology would be the investigation of phase change during machining process which is further addressed in Chapter 5. Experimental torque and thrust force profiles are generated from

drilling tests in AL6061-T6 workpieces containing pilot-holes with diameters of 2.5 mm, 3.5 mm, 5.5 mm, and 7.5 mm so that only the cutting lip is engaged during the cut. The drilling experiments cover a wide range of drilling conditions with spindle speeds ranging from 1592 rpm to 9868 rpm and feeds ranging from 0.08 mm/rev to 0.64 mm/rev. The methodology solves for the JC parameters so that as the drill's lip engages with the pre-cored work, the JC parameters are automatically adjusted in order to minimize the difference between predicted and experimentally measured torque values. This is done incrementally for each segment of the lip to which it is numerically subdivided. Curve fitting is performed based on the nonlinear least-squares optimization tool with convergence criterion of 10^{-9} and a maximum iteration number of 1000. Using initial randomly guessed values, all considered cases converged to the same set of JC parameter A, B, C, n, m of 317.54, 108.90, 0.0015, 0.43, 1.29, respectively, as compared with Johnson Cook [36] reported values of 324 MPa, 114 MPa, 0.002, 0.42, 1.34, respectively. The methodology robustness is demonstrated by comparing torque and thrust evolution profiles using the DLCFPM-found JC parameter versus experimental torque and thrust profiles. DLCFPM was shown to predict the drilling torque accurately but, to a lesser extent, the drilling thrust forces where some deviations from the experimental thrust values are observed. Future development of DLCFPM is planned to include the chip flow effect on thrust forces in the hope of improving the accuracy of the predicting capabilities for thrust forces.

CHAPTER IV

EXTRACTING HCP ZERILLI-ARMSTRONG MATERIAL PARAMETERS FROM ORTHOGONAL CUTTING TESTS ON AZ31B MAGNESIUM

This work reports on extending Oxley's analysis of the thick shear zone to account for HCP materials while utilizing Zerilli-Armstrong (ZA) constitutive law formulations. Ultimately, the work extracted the material coefficients for AZ31B, a magnesium-based alloy. First, orthogonal cutting tests were conducted using 0-degree rake angle inserts. Tests were run at uncut chip thickness and cutting speed values varying between 0.05 and 0.4 mm/rev and 50 to 250 mm/min, respectively. Extrapolated values of cutting and thrust parasitic forces were then subtracted from the measured forces. AZ31B magnesium alloy, HCP material model parameters are updated by minimizing the difference between the methodology-predicted forces and those experimentally collected with achieved predictability of R^2 of 0.91 and 0.93 for cutting and thrust forces, respectively. Although the simulations cover wide ranges of state variables, further validations were conducted by comparing numerical predictions of stress-strain for AZ31B against literature-published histories at operating strain (0 mm/mm to 0.1 mm/mm), strain rate (1000 s^{-1} to 3000 s^{-1}), and temperature (35C to 315 C) ranges with achieved mean predictability error of 8.5%.

A. Introduction

Given their specific mechanical properties and low material density, magnesium alloys are attractive for many industrial and structural purposes [45]. Therefore, it is important to be

able to characterize the mechanical response of magnesium materials under service loading conditions. This work reports turning tests using inserts so that orthogonal cutting conditions are setup (similar to Ozel [46]). Such experimentally measured orthogonal cutting forces include both cutting and parasitic force components [47]. For these force components and their corresponding cutting pressures, separating parasitic from cutting components are typically performed by extracting to zero-feed, and parasitic forces are subtracted from the measured forces (Guo and Chou [48]). Pure cutting and thrust pressures are then processed as per the methodology presented by Hamade et al. [3]. Cutting pressures were found to decrease with increasing cutting speed and uncut chip thickness inline with data reported by Seif et al. [49].

Considering that magnesium alloys have an HCP crystal structure, this research the use of a crystal structure-dependent material model of the HCP Zerilli Armstrong (ZA) material constitutive law reported by Zerilli [50] modified form reported by Ammouri and Hamade [24] applicable to AZ31B material response modeling.

This work reports on an extension of Oxley's thick shear zone analysis [27] by accounting for HCP materials utilizing Zerilli-Armstrong constitutive law reported applicable to AZ31B by Ammouri and Hamade [24]. Other conceived extensions include those reported by Lalwani et al. [19] and Adibi and Madhavan [51] to account for popular material models such as Johnson Cook and Maekawa models, respectively. Seif et al. [52] recently reported on another extension to account for the BCC/FCC crystal structure-dependent material model of the Zerilli-Armstrong type. This proposed extension adopts AZ31B thermo-physical properties presented by Valencia and Queded [53] following cutting thermal response at shear and tool chip interface for temperature modeling presented by Boothroyd [31] and used in Oxley [13]. The work develops an inverse scheme of orthogonal cutting experiments to update AZ31B Zerilli-

Armstrong HCP material model for predicting cutting and thrust machining forces. The inverse scheme uses the conceived thick shear zone HCP extension to update for finding AZ31B material model parameters that minimize the difference between the simulation forces and the experimentally collected cutting and thrust forces. The method also outputs the updated ZA constitutive law's parameters based on state variable ranges typically seen in cutting operations. This adopted inverse method is inline with work presented by Seif et al. [54] where based on utilizing drilling experiments, Johnson-Cook material model parameters are updated through an inverse methodology (based on Lalwani et al. [19]). To the authors' best knowledge, no reported work exists on utilizing orthogonal cutting of magnesium to extract such a material model. The updated AZ31B material model is validated by reporting a mean error of 8.5% achieved by comparing the numerically-calculated stress-strain response against response reported by Feng et al. [55] and Hasenpouth [25] at encountered strain, strain rate, and temperature conditions occurring in cutting operation. The advancement presented consist on adopting machining inverse methodology to update crystal structure dependent material model of Zerilli Armstrong type based on machining experiments as complementary substitute to standard tension compression tests necessary for material characterization.

This manuscript is organized into four sections:

Section 4.2 presents orthogonal cutting tests for measuring cutting and thrust forces using AZ31B workpiece material at varying cutting speed and uncut chip thickness conditions. For identifying forces related only to material removal action, parasitic forces are discarded out of the measured machining forces following extracting to the zero-feed method. Cutting pressures are, consequently, determined.

Section 4.3 reports on the extension of Oxley's [13] thick shear zone force analysis to account for HCP Zerilli Armstrong (ZA) material model as applicable to AZ31B. Thermo-physical properties of AZ31B are identified and utilized to estimate the operating shear and tool chip interface temperatures in accordance with empirical thermal loads, according to Boothroyd [31].

Section 4.4 delineates the methodology to determine the AZ31B material model parameters for the ZA form. Material model parameters are determined to satisfy the predictability of experimentally collected cutting and thrust forces using the Oxley ZA HCP model.

Section 4.5 presents the validation of this research methodology by comparing the found HCP Zerilli Armstrong material model against literature reported stress-strain data at varying operating ranges of strain, strain rate, and temperature. These values are of comparable magnitudes to those encountered in machining processes.

B. Experimental Force Collection and Processing

1. Force Collection

Orthogonal cutting tests are performed on workpieces made from AZ31B magnesium alloy pre-machined as five concentric tubes inline with workpiece multiple tubes arrangement adopted by Akram et al.[56] for turning experiments with each of concentric tubes having a thickness of 2.05 mm. Figure 4.1 shows the workpiece geometric characteristics and dimensions. Concentric tubes are pre-machined into thin cylinders ranging in inner diameter from 70 mm for the outer tube to 14 mm for the inner tube.

Part of experimentally collecting orthogonal cutting data implemented an integrated setup using Kistler type 3-Component plate Dynamometer (Type 9254) installed on HAAS SL20 CNC turning center having a 20 hp main drive and a maximum spindle speed of 4000 RPM.

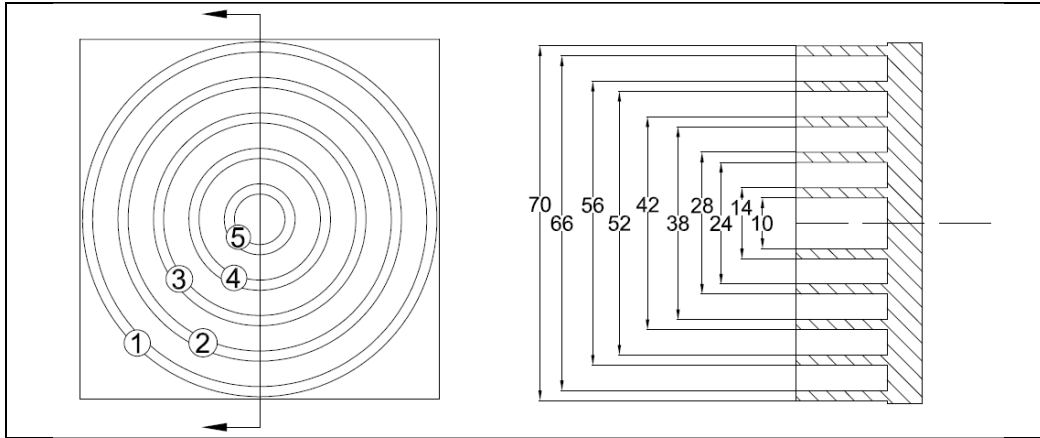


Figure 4.1 Workpiece configuration (left) arrangement and dimensions and (right) photograph revealing ring arrangement.

Figure 4.2a is a photograph of the experimental setup. Kistler dynamometer (Type 9254) mounted on HAAS SL20 CNC turning center. During machining, cutting and thrust forces are collected using the dynamometer where the signal is transmitted through multi-channel charge amplifier Type 5070A. Data is collected at a sampling rate of 2000Hz. Figure 4.2b shows a photograph of the machined workpiece where adopted for each combination of cutting speed and uncut chip thickness, a constant cutting length equal to 1700mm per experiment is performed. Conducted 7.96, 10.02, 13.53, 20.81, 45.09, cutting revolutions for experiments conducted on rings 1, 2, 3 4, 5 respectively.

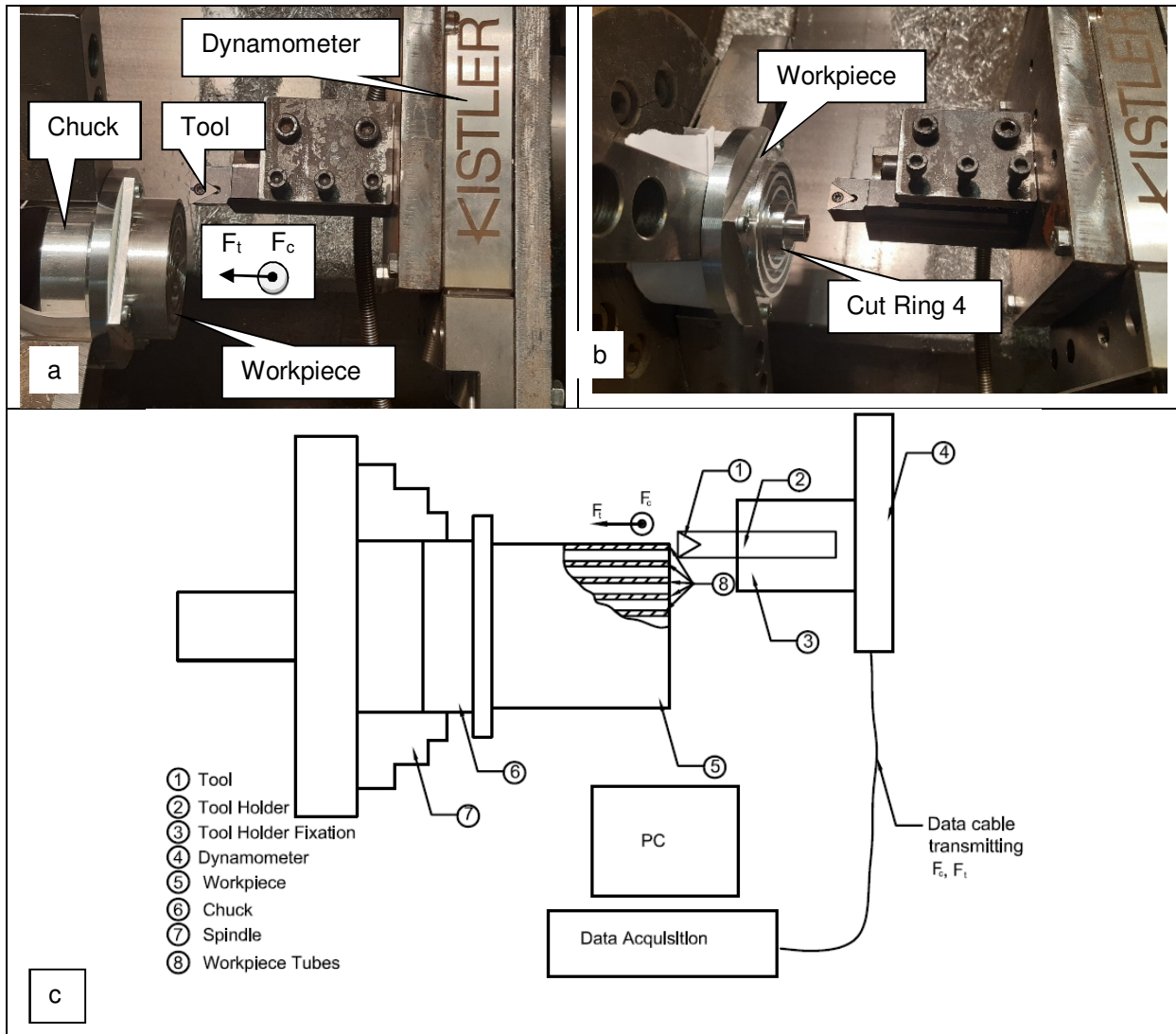


Figure 4.2. (a) Photograph of orthogonal cutting force measurement set up, (b) Photograph of a cut specimen. (c) Diagram representation of the orthogonal cutting force setup

Cutting speed and operating uncut chip thickness were varied and machining forces defined as cutting force F_c , thrust force F_t , and radial force F_r collected at measurement uncertainty of less than 1%. Figure 2c is a diagram illustrating the implemented orthogonal cutting setup.

Orthogonal cutting tests performed using triangular carbide inserts of type TCMW16T308. The utilized carbide inserts have a flat rake surface with no chip breaker. Each

insert is dotted with six operating cutting edge of 16.5mm length. Fresh cutting edges are employed with every cut, having an operating rake angle of zero degrees, clearance angle of 7 degrees, and cutting-edge radius (CER) of $5\mu\text{m}$ (0.005 mm).

Figure 4.3a is a photograph of the AZ31B workpiece with five concentric tubes machined. Figure 4.3b reports sample collected cutting and thrust forces at a condition of 400m/min cutting speed, and 0.3mm uncut chip thickness experimental data are processed using the median filter. Considering the sampling rate of 2000 Hz, the median filter with a data size of 40 samples proved to be effective in reducing signal noise and hysteresis in experimentally collected data, as presented in Figure 4.3b.

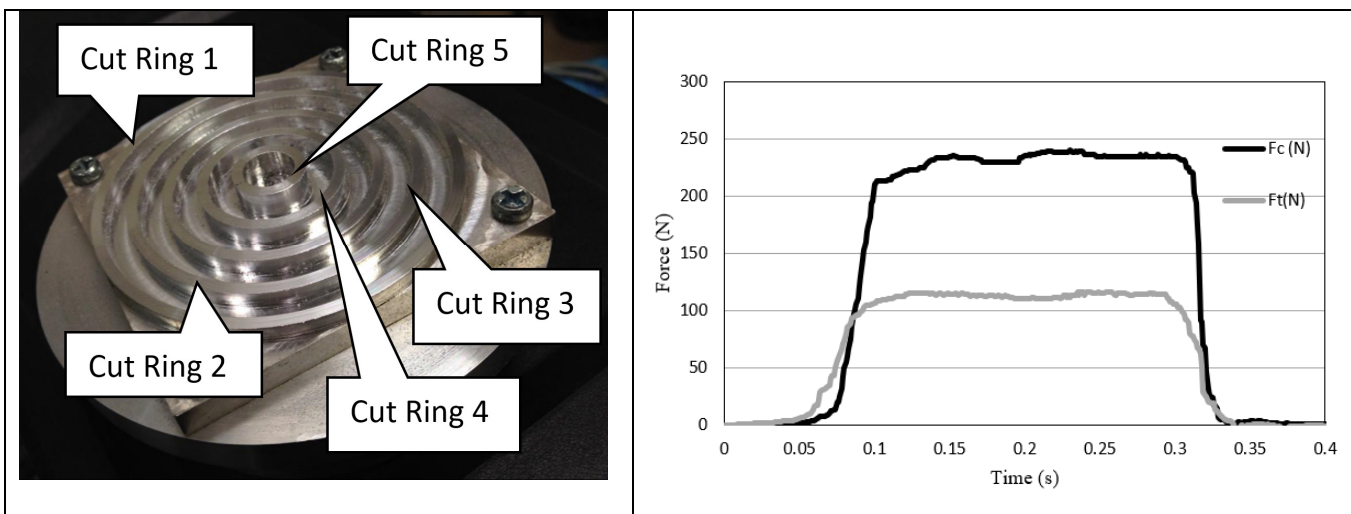


Figure 4.3. (left) photograph of AZ31B cut concentric tubes specimen; (right) sample of collected cutting and thrust forces: at 2000Hz sampling rate, $V=400$ m/min, $t_1=0.3$ mm.

Tubes are turned at constant conditions of cutting speed and uncut chip thickness (feed).

Experiments were designed so that cutting speed is constant throughout the cut. Reported in Table 4.1 is a summary of the experimental conditions encountered for the 25 conditions performed. Cutting tests used fresh TCMW 16T308 triangular carbide tools inserts fixed to SFCR1616H16 screw-on type tool holder. Cutting speed and uncut chip thickness were varied, with a total of 25 combinations of cutting parameters were performed. Uncut chip thickness is

varied from 0.05 mm/rev to 0.4 mm/rev, cutting speed from 50 to 400 mm/rev, all experiments conducted using zero rake angle tools, and at fixed cutting width of 2.05mm. Experiments were performed based on a fixed cutting length of 1.7 m resulting in total tool travel along the feed direction ranging from 2.25 mm to 3.18 mm for diameter tubes of 12 mm and 68 mm.

The cutting inserts have a fresh cutting-edge radius (CER) of 5 micrometers. Listed also in Table 4.1 are values of ratios of cutting-edge radius (CER) to uncut chip thickness t_1 ratio (in percentage). These values varied from 10% to 1.25% for uncut chip thickness of 0.05mm to 0.4mm, respectively.

Table 4.1. Experimental orthogonal cutting test results

Exp #	Cut length (mm)	Uncut chip thickness (mm)	CER ratio to t_1 %	Cutting speed (m/min)	Tube dia. (mm)	Number of revolutions	Time of cutting (s)	Rpm	Total feed length (mm)	Cutting Force F_c (N)	Thrust Force F_t (N)
1	1700	0.05	10.0%	50	12	45.1	2.0	1326.3	2.3	73.3	73.3
2				100	12	45.1	1.0	2652.6	2.3	72.0	71.0
3				132	12	45.1	0.8	3501.4	2.3	72.8	71.6
4		0.1	5.0%	50	26	20.8	2.0	612.1	2.1	118.5	86.5
5				100	26	20.8	1.0	1224.3	2.1	120.5	88.6
6				200	26	20.8	0.5	2448.5	2.1	110.5	78.5
7		0.2	2.5%	300	26	20.8	0.3	3672.8	2.1	103.5	73.5
8				50	40	13.5	2.0	397.9	2.7	189.5	103.0
9				100	40	13.5	1.0	795.8	2.7	170.1	101.0
10				200	40	13.5	0.5	1591.6	2.7	175.9	98.8
11				300	40	13.5	0.3	2387.3	2.7	162.5	88.5
12		0.3	1.67%	400	40	13.5	0.3	3183.1	2.7	152.5	79.5
13				50	54	10.0	2.0	294.7	3.0	239.7	111.0
14				100	54	10.0	1.0	589.5	3.0	272.5	111.5
15				200	54	10.0	0.5	1178.9	3.0	242.2	110.5
16				300	54	10.0	0.3	1768.4	3.0	241.5	103.0
17		0.4	1.25%	400	54	10.0	0.3	2357.9	3.0	210.5	94.5
18				50	68	8.0	2.0	234.1	3.2	298.5	107.5
19				100	68	8.0	1.0	468.1	3.2	289.5	108.5
20				200	68	8.0	0.5	936.2	3.2	261.5	100.5
21				300	68	8.0	0.3	1404.3	3.2	250.6	90.5
22		400	68	8.0	0.3	1872.4	3.2	230.0	88.6		

The contribution of the parasitic forces to the measured cutting and thrust forces is significant for large ratios (10%) but wanes for small ratio values (1.25%). Cutting force hysteresis is controlled using a median filter. Also listed in Table 4.1 are the measured orthogonal cutting and thrust forces for the corresponding cutting speed and operating uncut chip thickness. Each test was repeated twice under identical conditions. Each force value being the average measured cutting and thrust value over the full engagement time.

2. Cutting pressures

Plotted against cutting speed, presented in Figures 4.4 a and 4.4b are cutting, and thrust pressure (N/mm²) values calculated by dividing the measured forces by cut width (w) and uncut chip thickness (t_1). Pressures decrease are generally attributed to material softening at higher speeds.

Both pressures decrease with increasing uncut chip thickness due to the contribution of feed (size effect), where cutting becomes more efficient large feeds. Cutting and thrust pressure plots indicate a major effect of parasitic forces for cuts with low values of feed (uncut chip thickness). The considered CER to t_1 ratio values reflects the dominant contribution of parasitic edge forces at low feeds (see Table 4.1 for ratio values).

Of the many methods utilized (e.g., Albrecht [57], Stevenson [47], Guo, and Chou [48]) for isolating the contribution of edge forces from total measured forces, one is the zero feed extrapolation technique. Measured forces are plotted at constant cutting speed versus uncut chip thickness and extrapolated to zero feed. The resulting zero feed intercept values (typically positive) are identified as the parasitic forces.

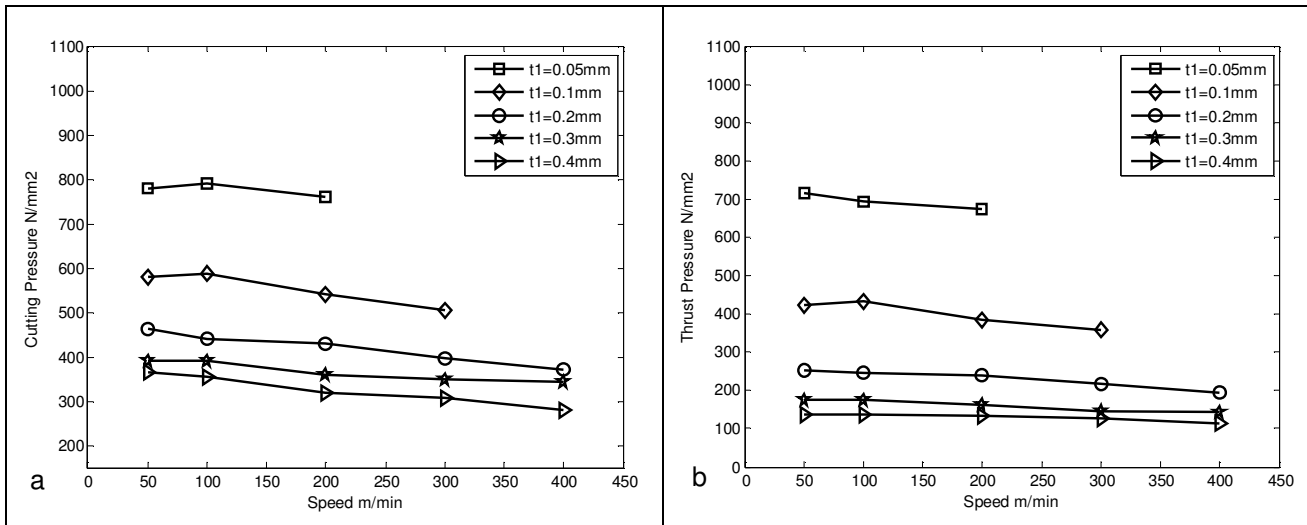


Figure 4.4 Raw experimental machining (a) cutting and (b) thrust pressures versus cutting speed for uncut chip thickness = 0.05, 0.1, 0.2, 0.3, and 0.4 mm.

Figure 4.5a and 4.5b show such plots for the experimentally collected cutting and thrust forces, respectively, at cutting speed of 50, 100, 200, 300, and 400 m/min grouped by operating cutting speed versus five levels of uncut chip thickness. As presented in Figures 4.5a and 4.5b, the zero-feed intercept representing parasitic cutting forces and parasitic thrust forces are estimated at about 53N and 65N, respectively. Machining parasitic forces are caused by the plastic deformation caused by the cutting-edge radius in addition to the rubbing action happening at the tool flank and the tool chip interface surfaces. Parasitic force values were found to range from 75% to 20% of the measured cutting and thrust forces as the uncut chip thickness increased from 0.05mm/rev to 0.4mm/rev.

The values of parasitic forces were subtracted from the total measured cutting and thrust forces (Table 4.1). Shown in Figures 4.6a and 4.6b are edge-force-corrected cutting and thrust pressures defined as K_c and K_t , respectively. These pressures were calculated using the experimental cutting (F_c), and thrust (F_t) forces by subtracting the edge cutting (F_{ce}) and thrust (F_{te}) forces [3] according to:

$$K_c = \frac{F_c - F_{ce}}{t_1 w} \quad (4.1)$$

$$K_t = \frac{F_t - F_{te}}{t_1 w} \quad (4.2)$$

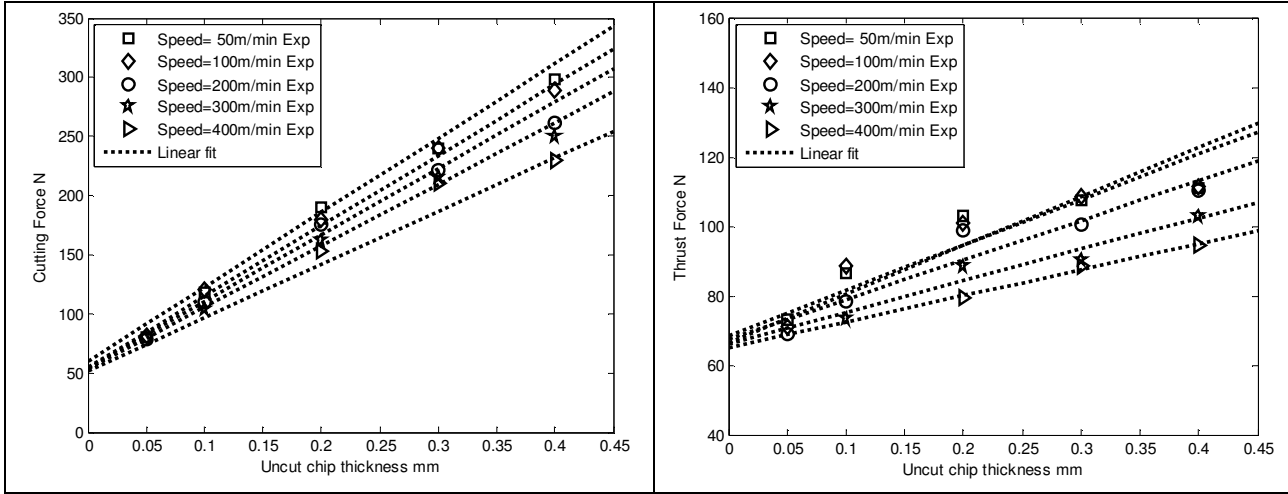


Figure 4.5. Zero feed extrapolation a. Cutting forces. b. Thrust

Figures 4.6a and 4.6b show a decreasing trend of edge-force-corrected cutting pressures with increased cutting speed caused by thermal softening encountered at higher cutting speeds. A slight size effect can still be seen in the figures but may be perhaps due to the zero-feed correction technique utilized.

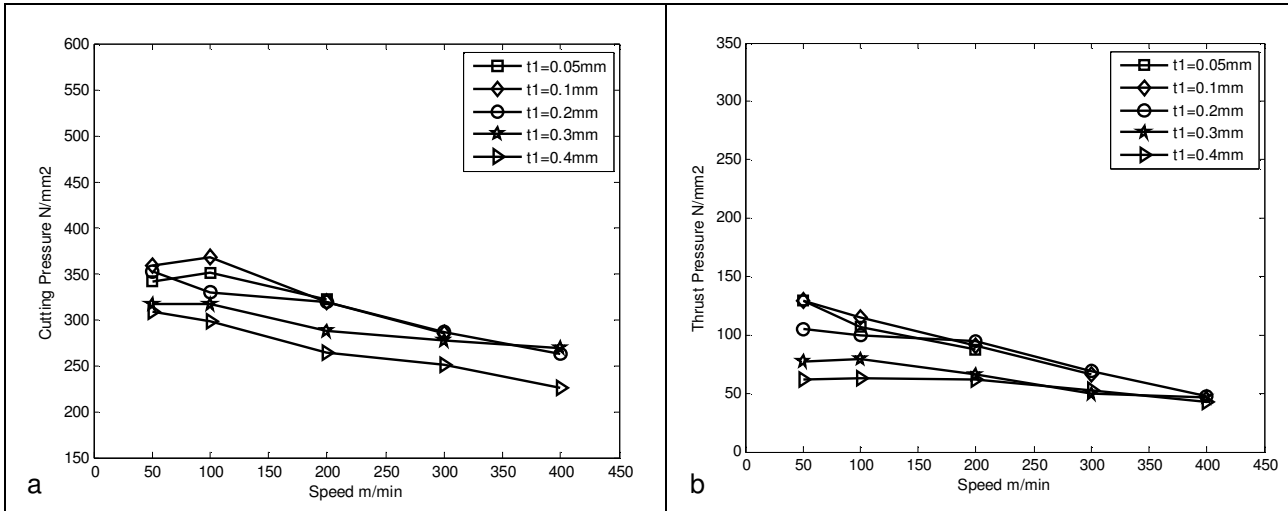


Figure 4.6 Corrected experimental machining (a) cutting and (b) thrust pressures versus cutting speed for uncut chip thickness = 0.05, 0.1, 0.2, 0.3, and 0.4 mm.

B. Oxley shear zone approach extension to Zerilli Armstrong constitutive law for HCP materials

In orthogonal machining, the material is removed under the linear motion of the cutting tool at fixed rake and clearance angles. Merchant in [11] was one of the first to provide a quantitative study for orthogonal cutting where he provided a methodology based on the thin shear plane approach to predict the shear angle, cutting, and thrust forces function of known shear stress and tool chip friction angle. Utilizing a material flow stress model of the form $\sigma = \sigma_1 \epsilon^{n'}$, Oxley [27] introduced an analytical scheme based on the thick shear zone approach that predicts the shear angle, tool chip friction angle, and cutting forces. The analysis determines the resultant shear angle, ϕ , primary deformation zone thickness, S_1 , and secondary deformation zone of thickness, S_2 , at conditions that satisfy equilibrium between shear transmitted forces and tool chip interface forces.

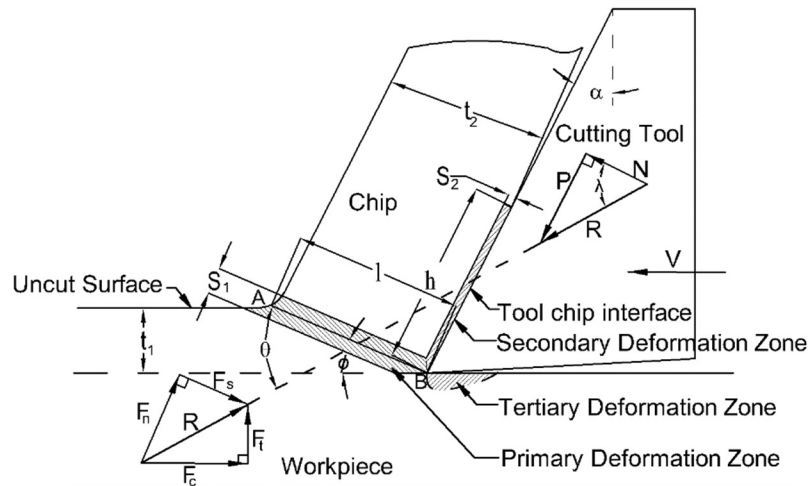


Figure 4.7. Shear zone's orthogonal cutting parameters and force components ([52]).

Figure 4.7 shows the three main deformation zones associated with orthogonal cutting

1. Primary deformation zone at the shear deformation zone.

2. Secondary deformation zone at the chip tool contact zone.
3. Tertiary deformation zone at the newly formed workpiece surface.

To incorporate other material constitutive equations, Lalwani et al. [19] and Adibi and Madhavan [51] proposed extensions to Oxley's analysis to account for Johnson cook and Maekawa types of material models, respectively. Recently, Seif et al. [52] extended the Oxley shear zone approach to incorporate the Zerilli Armstrong material model for dual-phase BCC/FCC materials. Considering the increasing utilization of HCP crystal structure magnesium-based alloys, this work presents an extension of Oxley's analysis to incorporate Zerilli Armstrong constitutive law for HCP materials [50] applicable for AZ31B solid-phase AZ31B and valid up to melting temperature of 650 C [53].

$$\sigma = C_0 + B \exp\left(-\beta_0 T + \beta_1 T \ln\left(\frac{\dot{\epsilon}}{\dot{\epsilon}_0}\right)\right) + B_0 \epsilon^n \exp\left(-\alpha_0 T + \alpha_1 T \ln\left(\frac{\dot{\epsilon}}{\dot{\epsilon}_0}\right)\right) \quad (4.3)$$

Where C_0 is activation stress, B and B_0 are thermal stress constants, and β_0 , β_1 , α_0 and α_1 are Peierls interaction parameters coupled with the forest dislocation interaction parameters [50] and are experimentally determined material constants

Ammouri and Hamade [24] introduced a modification to this material model via a modified version of Eq. 4.3 by incorporating a strain recovery term, ϵ_r ,

$$\sigma = C_0 + B \exp\left(-\beta_0 T + \beta_1 T \ln\left(\frac{\dot{\epsilon}}{\dot{\epsilon}_0}\right)\right) + B_0 \sqrt{\epsilon_r \left(1 - \exp\left(\frac{-\epsilon}{\epsilon_r}\right)\right)} \exp\left(-\alpha_0 T + \alpha_1 T \ln\left(\frac{\dot{\epsilon}}{\dot{\epsilon}_0}\right)\right) \quad (4.4)$$

This form was shown [9] to exhibit improved fitting capabilities to experimental stress-strain data of AZ31B.

1. ZA-extended Oxley's for HCP materials

Extending Oxley's analysis starts by defining the flow stress variation across the primary deformation zone thickness, S_1 . Estimation of average shear stress at the primary deformation zone based on HCP Zerilli Armstrong with strain recovery (Eq. 4.4) and satisfying the Von Mises flow rule, shear stress k_{AB} is described by

$$k_{AB} = \frac{C_0 + B \exp\left(-\beta_0 T + \beta_1 T \ln\left(\frac{\dot{\varepsilon}}{\dot{\varepsilon}_0}\right)\right) + B_0 \sqrt{\varepsilon_r \left(1 - \exp\left(\frac{\varepsilon}{\varepsilon_r}\right)\right) \exp\left(-\alpha_0 T + \alpha_1 T \ln\left(\frac{\dot{\varepsilon}}{\dot{\varepsilon}_0}\right)\right)}{\sqrt{3}} \quad (4.5)$$

Linking shear stress variation to primary deformation zone thickness, Adibi and Madhavan [51] reported the term $C' n_{eq}$ as made equivalent to $\left(\frac{\delta k}{\delta s_1}\right) \frac{1}{2k_{AB}}$ where the primary deformation zone thickness ratio, C' , and equivalent strain hardening index, n_{eq} , are found through iterating.

The flow diagram in Figure 4.8 illustrates this work's methodology for utilizing an equivalent strain hardening index, n_{eq} , compatible with Zerilli Armstrong [19] while extending Oxley's [13] thick shear zone analysis. A closed-form solution for n_{eq} is

$$n_{eq} = \left(\frac{d\sigma_{AB}}{d\varepsilon_{AB}}\right) \left(\frac{\varepsilon_{AB}}{\sigma_{AB}}\right) \quad (4.6)$$

Invoking Zerilli-Armstrong constitutive model for HCP materials (Eq. 4.4), the derivative of the material model with respect to operating strain is

$$\frac{d\sigma_{AB}}{d\varepsilon_{AB}} = \left(\frac{d\sigma}{d\varepsilon} \frac{d\varepsilon}{d\varepsilon}\right)_{AB} + \left(\frac{d\sigma}{d\dot{\varepsilon}} \frac{d\dot{\varepsilon}}{d\varepsilon}\right)_{AB} + \left(\frac{d\sigma}{dT} \frac{dT}{d\varepsilon}\right)_{AB} \quad (4.7)$$

Applying derivative rules to HCP Zerilli-Armstrong constitutive model Eq. 4.4, the derivative terms of Eq. 4.6 yield

$$\left(\frac{D\sigma}{d\varepsilon}\right)_{AB} = \frac{0.5B_0 \exp\left(-\alpha_0 T + \alpha_1 T \ln\left(\frac{\dot{\varepsilon}}{\dot{\varepsilon}_0}\right)\right) \exp\left(\frac{-\varepsilon}{\varepsilon_r}\right)}{\sqrt{\left(\varepsilon_r \left(1 - \exp\left(\frac{-\varepsilon}{\varepsilon_r}\right)\right)\right)}} \quad (4.8)$$

$$\left(\frac{d\sigma}{dT}\right)_{AB} = B \left(-\beta_0 + \beta_1 \ln\left(\frac{\dot{\varepsilon}}{\dot{\varepsilon}_0}\right)\right) \exp\left(-\beta_0 T + \beta_1 \ln\left(\frac{\dot{\varepsilon}}{\dot{\varepsilon}_0}\right) T\right) + B_0 \sqrt{\left(\varepsilon_r \left(1 - \exp\left(\frac{-\varepsilon}{\varepsilon_r}\right)\right)\right)} \left(-\alpha_0 + \alpha_1 \ln\left(\frac{\dot{\varepsilon}}{\dot{\varepsilon}_0}\right)\right) \exp\left(-\alpha_0 T + \alpha_1 T \ln\left(\frac{\dot{\varepsilon}}{\dot{\varepsilon}_0}\right)\right) \quad (4.9)$$

$$\left(\frac{dT}{d\varepsilon}\right)_{AB} = \frac{\beta_T \sigma_{AB}}{\rho C_p} = \frac{\beta_T \left(C_0 + B \exp\left(-\beta_0 T + \beta_1 T \ln\left(\frac{\dot{\varepsilon}}{\dot{\varepsilon}_0}\right)\right) + B_0 \sqrt{\left(\varepsilon_r \left(1 - \exp\left(\frac{-\varepsilon}{\varepsilon_r}\right)\right)\right)} \exp\left(-\alpha_0 T + \alpha_1 T \ln\left(\frac{\dot{\varepsilon}}{\dot{\varepsilon}_0}\right)\right) \right)}{\rho C_p} \quad (4.10)$$

The term $\left(\frac{dT}{d\varepsilon}\right)$ vanishes from Eq. 4.5 due to the shear plane maximum strain-rate principle. Substituting Eqs, 4.8, 4.9, 4.10 and $\left(\frac{dT}{d\varepsilon}\right) = 0$ in Eq. 4.7 yields

$$\frac{d\sigma_{AB}}{d\varepsilon_{AB}} = \frac{0.5C_5 \exp\left(-\alpha_0 T + \alpha_1 T \ln\left(\frac{\dot{\varepsilon}}{\dot{\varepsilon}_0}\right)\right) \exp\left(\frac{-\varepsilon}{\varepsilon_r}\right)}{\sqrt{\left(\varepsilon_r \left(1 - \exp\left(\frac{-\varepsilon}{\varepsilon_r}\right)\right)\right)}} + \frac{\beta_T}{\rho C_p} \left(B \left(-\beta_0 + \beta_1 \ln\left(\frac{\dot{\varepsilon}}{\dot{\varepsilon}_0}\right)\right) \exp\left(-\beta_0 T + \beta_1 \ln\left(\frac{\dot{\varepsilon}}{\dot{\varepsilon}_0}\right) T\right) + B_0 \sqrt{\left(\varepsilon_r \left(1 - \exp\left(\frac{-\varepsilon}{\varepsilon_r}\right)\right)\right)} \left(-\alpha_0 + \alpha_1 \ln\left(\frac{\dot{\varepsilon}}{\dot{\varepsilon}_0}\right)\right) \exp\left(-\alpha_0 T + \alpha_1 T \ln\left(\frac{\dot{\varepsilon}}{\dot{\varepsilon}_0}\right)\right) \right) \left(C_0 + B e^{\left(-\beta_0 T + \beta_1 \ln\left(\frac{\dot{\varepsilon}}{\dot{\varepsilon}_0}\right) T\right)} + B_0 \sqrt{\left(\varepsilon_r \left(1 - \exp\left(\frac{-\varepsilon}{\varepsilon_r}\right)\right)\right)} \exp\left(-\alpha_0 T + \alpha_1 \ln\left(\frac{\dot{\varepsilon}}{\dot{\varepsilon}_0}\right) T\right) \right) \quad (4.11)$$

Considering that $1/C_p \sim 0$ and using Eqs. 4.7 and 11, the Oxley [13] equivalent strain hardening index $n_{eq}(\text{HCP})$ for Zerilli–Armstrong HCP material can be described by

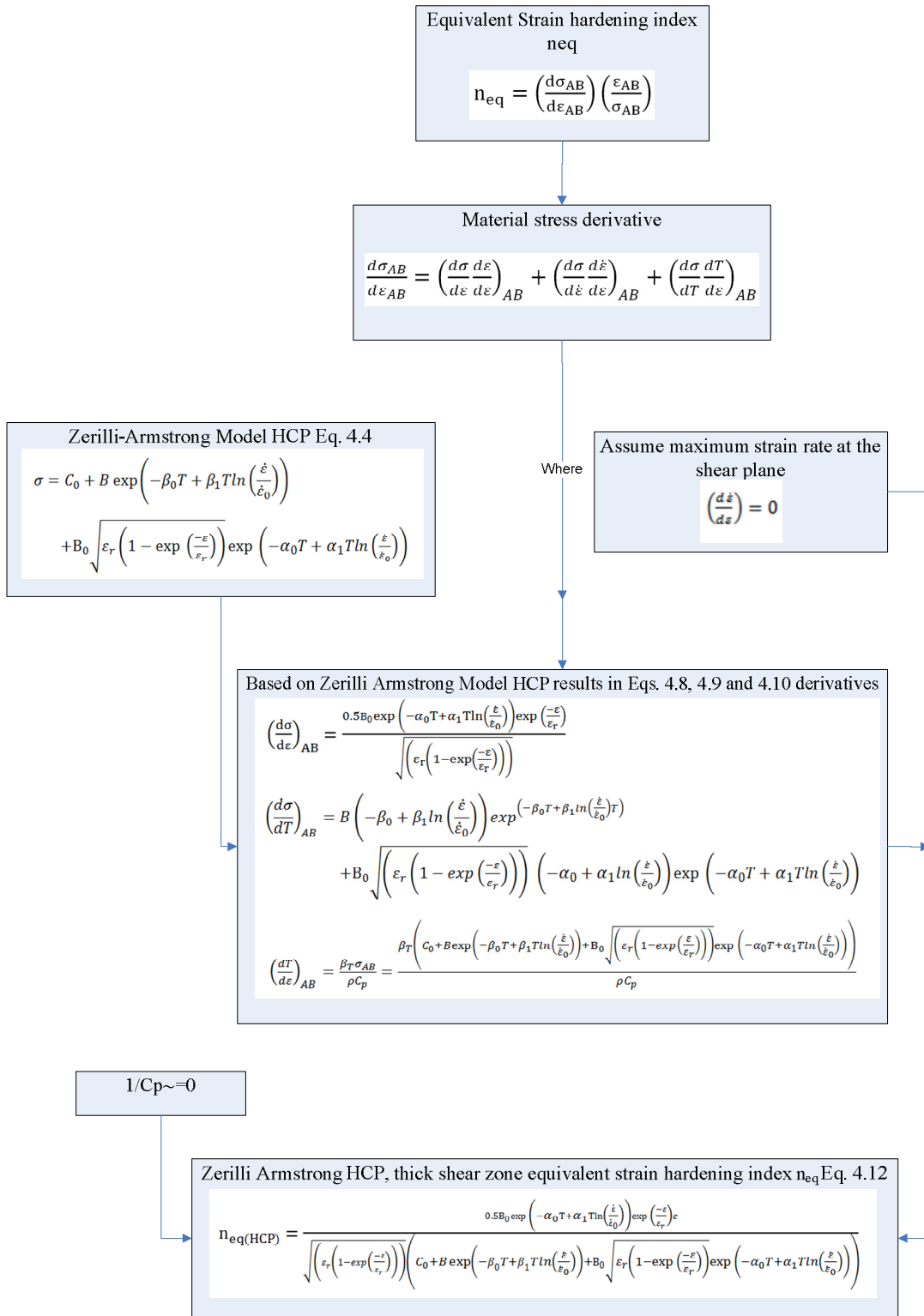


Figure 4.8. Flowchart illustrating the Zerilli-Armstrong thick shear zone extension methodology

$$n_{\text{eq(HCP)}} = \frac{0.5B_0 \exp\left(-\alpha_0 T + \alpha_1 T \ln\left(\frac{\dot{\varepsilon}}{\dot{\varepsilon}_0}\right)\right) \exp\left(\frac{-\varepsilon}{\varepsilon_r}\right) \varepsilon}{\sqrt{\left(\varepsilon_r \left(1 - \exp\left(\frac{-\varepsilon}{\varepsilon_r}\right)\right)\right) \left(C_0 + B \exp\left(-\beta_0 T + \beta_1 T \ln\left(\frac{\dot{\varepsilon}}{\dot{\varepsilon}_0}\right)\right) + B_0 \sqrt{\varepsilon_r \left(1 - \exp\left(\frac{-\varepsilon}{\varepsilon_r}\right)\right) \exp\left(-\alpha_0 T + \alpha_1 T \ln\left(\frac{\dot{\varepsilon}}{\dot{\varepsilon}_0}\right)\right)}\right)} \quad (4.12)$$

Applying Eq. 4.4, the strain hardening index in Eq. 4.12 is employed in extending Oxley's thick shear zone analysis [13] as per Lalwani et al. [19] for HCP AZ31B material, which was found appropriate by Ammouri and Hamade [24].

2. AZ31B Thermo-physical Properties

Oxley [13], Lalwani et al. [19], and Seif et al. [52] relied on empirical relations reported by Boothroyd [31] to assign average machining temperatures along the primary shear zone, TAB,

$$T_{AB} = T_w + \eta \frac{(1-\beta_T)F_s \cos\alpha}{\rho_d C_p t_1 w \cos(\theta-\alpha)} \quad (4.13)$$

and secondary (tool chip interface) zone, T_{int},

$$T_{int} = T_w + \frac{(1-\beta_T)F_s \cos\alpha}{\rho_d C_p t_1 w \cos(\theta-\alpha)} + \psi \Delta T_m \quad (4.14)$$

where the initial operating temperature is represented by the working temperature, T_w . The term η is equal to 0.7 and represent the proportion of plastic deformation transformed to heat within the shear zone, the term product defined by $\psi \Delta T_m$ is the average chip temperature rise at the secondary deformation zone with maximum to average transformation factor ψ of 0.6 reported by Oxley [13]. For AZ31B and as to be used in equations (4.13-4.14), temperature-dependent specific heat and thermal conductivity were reported [53] as

$$c_p (J/(K * Kg)) = \frac{4.184}{24.305} (5.33 + 2.45 * 10^{-3} T - 0.103 * 10^{-5} T^{-2}) \quad (4.15)$$

$$k_s(W/(m * K)) = 67.12 + 655.7 * 10^{-4}T \quad (4.16)$$

D. Determining ZA material model via the inverse method

The edge-force-corrected cutting and thrust forces (Figure 4.6) attributed to the cutting action only are utilized to extract the HCP Zerilli Armstrong material model parameters for AZ31B. Material coefficients C_0 , B , β_0 , β_1 , B_0 , α_0 , α_1 , and ε_r are found based on the inverse method utilizing MATLAB® for nonlinear fitting of pressure data. Found are the values combination of these coefficients that minimize the error in Eq.4.17 between the conceived inverse method and those measured cutting and thrust forces with a mean error of 5%:

$$\min \left[\sqrt{\sum \left((F_{measured} - F_{predicted})^2 \right)} \right] \quad (4.17)$$

Table 4.2 lists searching ranges (upper and lower limits) and four different cases that were numerically run to estimate the coefficients. Material parameters were updated using the convergence criterion of 10-9 and adopted the maximum iteration number of 1000 with random initializing parameters.

Table 4.2. ZA parameters: ranges, initially assigned values, and determined values.

ZA Parameters		C_0	B	β_0	β_1	B_0	ε_r	α_0	α_1
Searching range	Lower limit	0	0	0	-0.01	0	0	0	-0.01
	Upper limit	260	1600	0.3	0.02	1100	10	0.01	0.002
Case #1	Initializing parameters from Ammouri and Hamade [24]	0	1532	0.0063	0.000016	1015	0.071	0.0004	0.0003
	Found parameters	163.53	324.2	0.0341	-0.0002	304.82	2.264	0.0015	-0.00024
Case #2	Random initial parameter values	90..5	326.2	0.0193	-0.0014	287.63	1.137	0.0005	-0.0017
	Found parameters	163.5	324.2	0.0341	-0.0002	304.82	2.264	0.0015	-0.00024
Case #3	Random initial parameter values	100	250	0.2	0.1	200	8	0.005	-0.0005
	Found parameters	163.53	324.2	0.0341	-0.0002	304.82	2.264	0.0015	-0.00024
Case #4	Random initial parameter values	200	300	0.25	0.15	250	1	0.075	0.005
	Found parameters	163.53	324.2	0.0341	-0.0002	304.82	2.264	0.0015	-0.00024

MATLAB® nonlinear least-square optimization scheme is utilized, and found are updated HCP ZA parameters that minimize the objective function Eq. 4.17 and meeting the global and local quadratic convergence targets. Reference strain rate $\dot{\epsilon}_0 = 100 \text{ s}^{-1}$ adopted smaller by two orders in relation to the operating strain rate to enhance the robustness of the model identification optimization scheme inline with Guo et al. [58] for the adopted searching range for the different HCP ZA parameters.

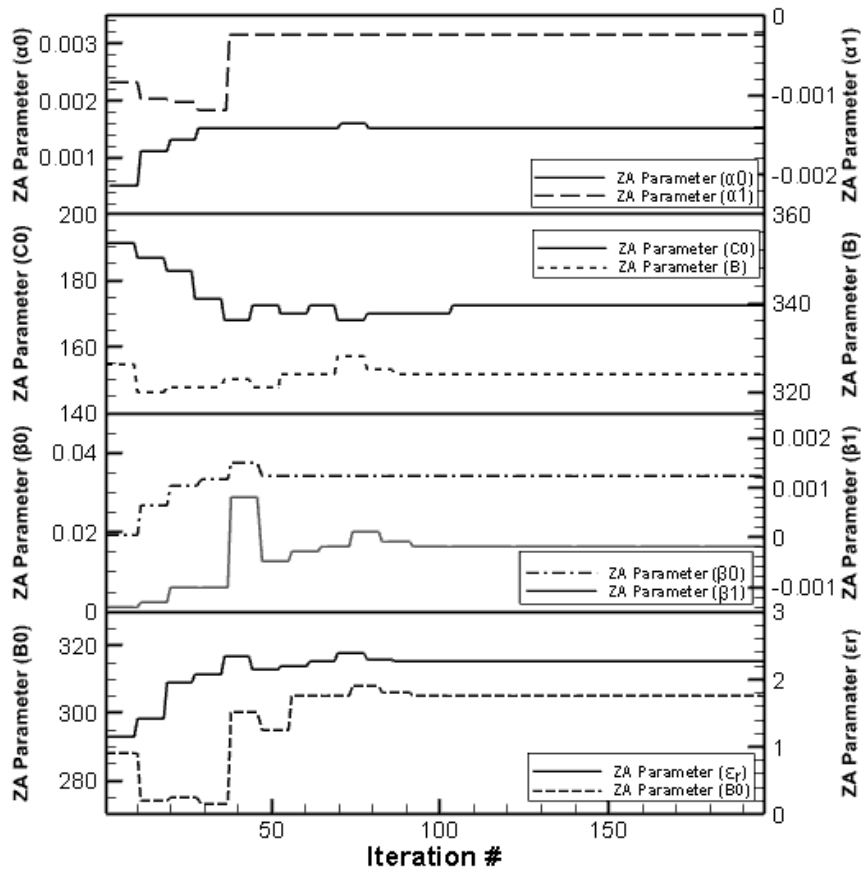


Figure 4.9 Case#2: Conversion records of ZA parameters

E. Validation of ZA-extended Oxley's for AZ31B: Cutting forces and state variables

For each case, HCP Zerilli Armstrong parameter initial values were varied. For the search ranges listed, the updated AZ31B material model coefficients were determined with all cases converging identical set of coefficients. After 200 iterations, the converged HCP model

parameters were found to be: $C_0=163.53$, $B=324.2$, $\beta_0=0.0341$, $\beta_1=-0.0002$, $B_0=304.82$, $\epsilon_r=2.264$, $\alpha_0=0.0015$, $\alpha_1=-0.00024$. The table lists these values of the converged HCP ZA coefficients. Figure 4.9 presents the coefficient conversion records for a typical case (Case#2).

Table 4.3. Estimated generated state variables.

Exp #	Uncut chip thickness (mm)	Cutting speed (m/min)	Cutting length (mm)	t_2 (mm)	ϵ_{AB} (mm/mm)	$\dot{\epsilon}_{AB}$ (s^{-1})	ϵ_{int} (mm/mm)	$\dot{\epsilon}_{int}$ (s^{-1})	T_{AB} (C)	T_{int} (C)
1	0.05	50	1700	0.103	0.73	13,141	3.147	11,445	68.61	117.53
2	0.05	100	1700	0.103	0.73	28,159	3.154	22,891	74.80	134.88
3	0.05	151	1700	0.103	0.73	48,828	3.150	45,790	79.68	152.40
4	0.1	50	1700	0.196	0.71	6,374	3.112	12,491	78.72	139.92
5	0.1	100	1700	0.196	0.71	13,728	3.118	24,982	83.68	159.01
6	0.1	200	1700	0.196	0.71	31,379	3.112	49,963	87.42	178.38
7	0.1	300	1700	0.196	0.71	40,010	3.117	74,945	89.30	193.07
8	0.2	50	1700	0.376	0.70	3,070	3.079	6,801	89.10	166.38
9	0.2	100	1700	0.376	0.70	6,651	3.084	13,602	92.75	187.70
10	0.2	200	1700	0.393	0.71	14,709	3.118	24,982	96.51	219.78
11	0.2	300	1700	0.393	0.71	23,534	3.121	37,472	97.82	238.54
12	0.2	400	1700	0.393	0.71	33,340	3.117	49,963	97.39	251.21
13	0.3	50	1700	0.541	0.68	1,956	3.054	4,928	95.35	183.65
14	0.3	100	1700	0.564	0.70	4,434	3.075	9,068	98.86	209.63
15	0.3	200	1700	0.564	0.70	9,551	3.086	18,136	100.77	240.75
16	0.3	300	1700	0.564	0.70	15,349	3.084	27,204	99.91	259.37
17	0.3	400	1700	0.589	0.71	20,919	3.122	33,309	100.81	289.01
18	0.4	50	1700	0.722	0.68	1,467	3.048	3,696	100.52	199.22
19	0.4	100	1700	0.722	0.68	3,200	3.051	7,391	102.74	223.41
20	0.4	200	1700	0.752	0.70	7,163	3.078	13,602	103.48	260.37
21	0.4	300	1700	0.752	0.70	11,512	3.076	20,403	102.37	280.91
22	0.4	400	1700	0.785	0.71	15,689	3.113	24,982	103.20	314.30

Updated AZ31B HCP Zerilli Armstrong material model parameters of C_0 , B , β_0 , β_1 , B_0 , α_0 , α_1 , and ϵ_r reported in Table 2 are found for the operating range of temperature, strain, and strain rates ranges reported in Table 3. For the 22 experiments performed (Table 4.1), Table 4.3 lists the operating conditions of strain, strain rate, and temperature values occurring at the primary and secondary deformation zones for the machining conditions of cutting speed and uncut chip thickness. Estimated numerical values of generated temperatures, strains, and strain rates varied between 68 C and 315 C, 0.73 and 3.13 mm/mm, and between 1,956 s^{-1} and

49,963s¹. Researchers may find these corresponding values of use in deformation applications of comparable state variables of temperature, strain, and strain rates.

The ZA found parameters are applicable for modeling of machining forces for AZ31B for cutting conditions of speed and uncut chip thickness (Table 4.1). The HCP coefficients found using the extended thick shear zone approach yield numerical values of forces that compare well with edge-forces-corrected values of cutting and thrust forces, as shown in Figure 4.10. The figure shows good agreements of cutting speed (50 to 400 m/min) and uncut chip thickness (0.05, 0.1, 0.2, 0.3, and 0.4 mm) with predictability R square achieved for cutting (Figure 4.10.a) and thrust (Figure 4.10.a) forces of 0.94 and 0.91, respectively.

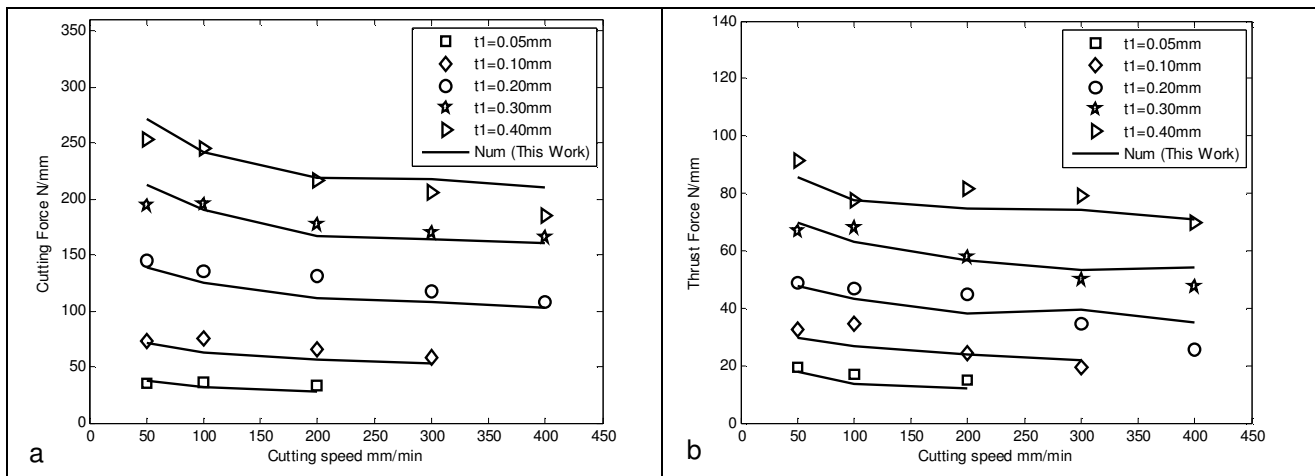


Figure 4.10 Numerical (solid lines) and experimental (data points) machining results for (a) cutting and (b) thrust forces versus cutting speed for uncut chip thickness = 0.05, 0.1, 0.2, 0.3, and 0.4 mm.

Figure 4.11 shows the inverse method's shear and tool chip interface operating temperature results. Shear plane temperature calculations are found to be fairly constant in cutting speed, increasing between 60 C and 103 C with uncut chip thickness.

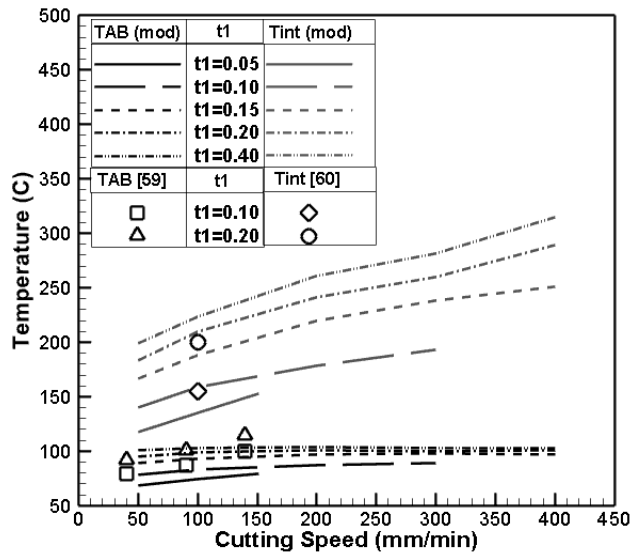


Figure 4.11 Shear and tool-chip interface temperatures: numerical versus those reported by [59] and [60]

Figure 4.11 shows the calculated shear zone temperatures to be in agreement with experimentally collected temperature measurements reported by Viswanathan et al. [59] for cutting speeds (ranging from 40mm/min to 140mm/min) and uncut chip thickness (from 0.1 and 0.2 mm/rev). Tool/chip interface temperatures increase with operating cutting speed and uncut chip thickness ranging between 117C and 314 C for the investigated cases. Figure 4.11 plots these calculated interface temperature values and are found in agreement with values reported by (Nasr and Outeiro in [60]) from finite element simulations for dry machining of AZ31B material at cutting speed of 100 mm/min and uncut chip thicknesses of 0.1 and 0.2 mm/rev (using cutting tool with CER = 2 μ m).

F. Validation of ZA-extended Oxley's for AZ31B: Stress-Strain behavior

For validation, the found ZA constitutive law parameters are found to predict the stress-strain behavior of AZ31B very well. Found literature mechanical response histories lie well within the studied state variables of strain (0.68 to 3.150mm/mm), strain rate (1,956 s⁻¹ to

49,963s⁻¹), and temperature (68C to 315 C). These values are validated against material flow stress data from Split-Hopkinson Tension Bar (Feng et al. [55]) for AZ31B material at conditions of strain (0 mm/mm to 0.1mm/mm), strain rate (1100 s⁻¹ to 3000 s⁻¹), and temperature (100 C to 250 C) similar to conditions encountered in the machining process.

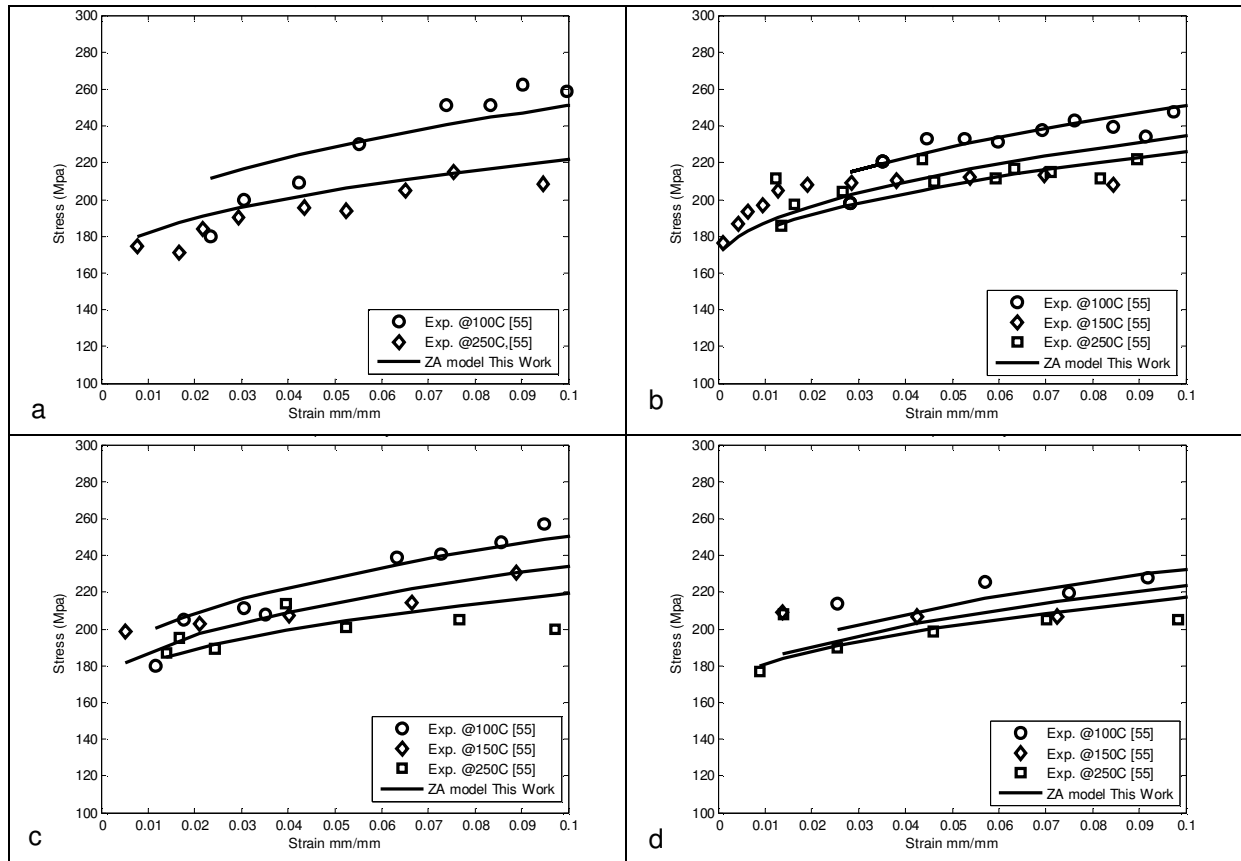


Figure 4.12 Validation of the found AZ31B Zerilli Armstrong model plotted against strains for 100, 150, and 250 C at strain rates of: a) 1000, b) 1400, c) 1500, and d) 3000 s⁻¹. Data from [55] co-plotted as points.

Figure 4.12 shows the found AZ31B material model to predicted well the material response for operating temperature range from 100C to 250C, strain, and strain rate ranges of 0 to 0.1mm/mm and 1000 to 3000 s⁻¹, respectively. The found ZA HCP material model archived a mean error of 8% when predicting Feng et al.[55] flow stress data for AZ31B.

For additional validation, comparisons are made between the found ZA flow stress model and data reported by Hasenpouth [25] (tensile split Hopkinson tests) at operating range of strain 0 to 0.1, strain rate 500 s⁻¹ to 1500 s⁻¹ and temperature of 45 C to 250 C. Figure 4.13 shows the found material model to track well against the reported [25] material response with a maximum error of 6% for the said operating conditions.

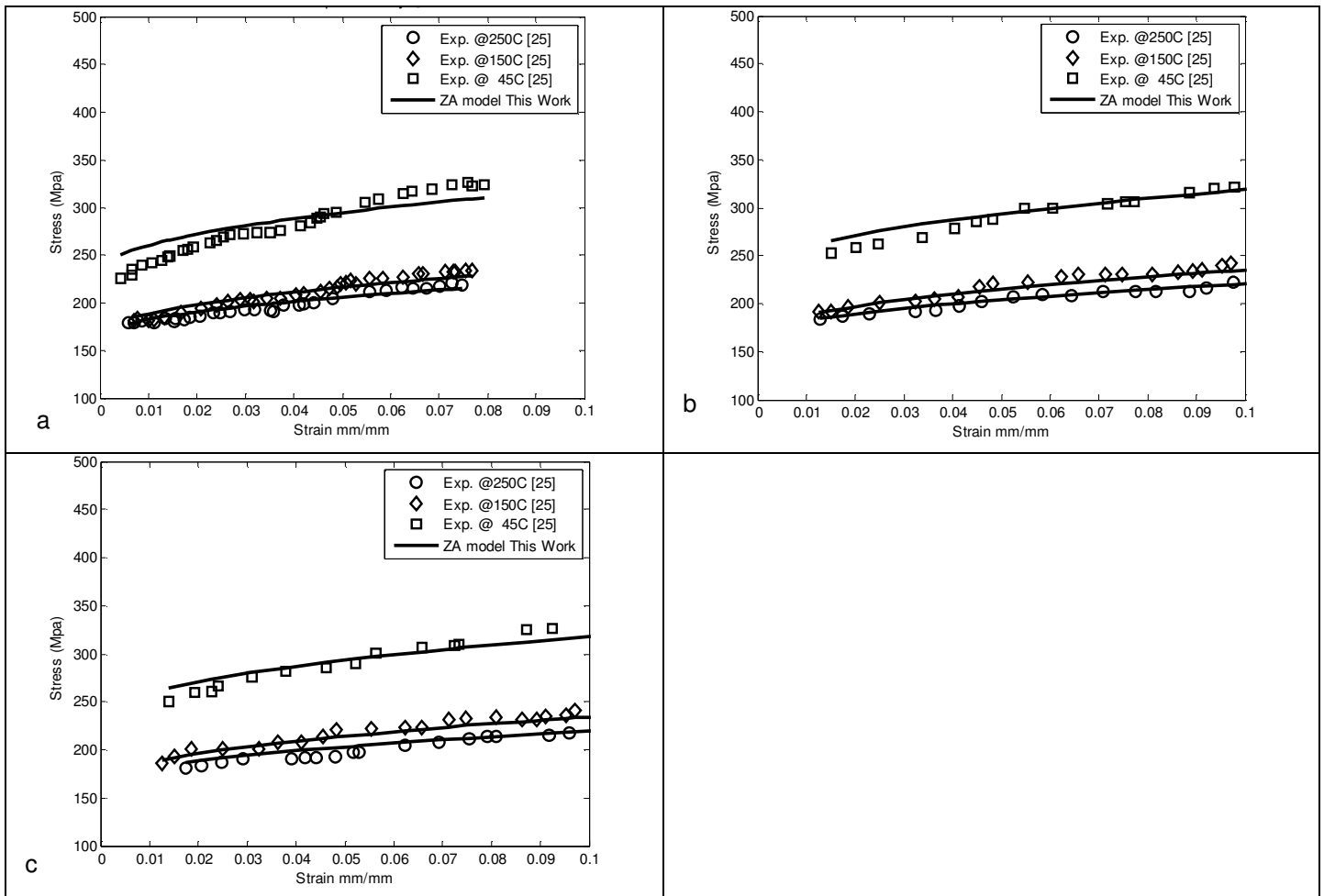


Figure 4.13 Validation of the found AZ31B Zerilli Armstrong model plotted against strains for 45, 150, and 250 C at strain rates of: a) 500 s⁻¹, b) 1000 s⁻¹, and c) 1500 s⁻¹. (Data from [25] co-plotted as points).

Figures 4.12 and 4.13 show the updated AZ31B ZA material model to achieve good predictability when compared with material flow stress data generated by Feng et al. [55] and

Hasenpouth [25] at operating temperatures ranging from 45C to 250C, strains from 0.01 to 1 mm/mm, strain rates ranging from 0.001s⁻¹ to 1500 s⁻¹.

G. Discussion

To determine updated constants for the Zerilli Armstrong for AZ31B HCP material model [50], Kurukuri et al. [61] utilized tension-compression tests that yielded effective stress model as follows:

$$\sigma = 152.7 + (28.7 + 17.6\sqrt{\varepsilon})\exp\left(-0.0039T + 0.00089T\ln\left(\frac{\dot{\varepsilon}}{\dot{\varepsilon}_0}\right)\right) + 389.4\varepsilon^{0.4} \quad (4.18)$$

For AZ31B, Hasenpouth [25] reported another model and related constants

$$\begin{aligned} \sigma = 177.452 + 160.095 \exp\left(-0.0131T + 0.00139T\ln\left(\frac{\dot{\varepsilon}}{\dot{\varepsilon}_0}\right)\right) \\ + (573.813\varepsilon^n)(1.17 - 0.00324T + 2.66 * 10^{-6}T^2) \end{aligned} \quad (4.19)$$

For AZ31B, this work Equation 4.20 reports the found parameters following the Zerilli Armstrong constitutive law

$$\begin{aligned} \sigma = 163.53 + 324.2 \exp\left(-\left(0.0341T + 0.0002T\ln\left(\frac{\dot{\varepsilon}}{\dot{\varepsilon}_0}\right)\right)\right) \\ + 304.82\sqrt{\varepsilon_r\left(1 - \exp\left(\frac{-\varepsilon}{2.264}\right)\right)} \exp\left(-\left(0.0015T + 0.00024T\ln\left(\frac{\dot{\varepsilon}}{\dot{\varepsilon}_0}\right)\right)\right) \end{aligned} \quad (4.20)$$

Table 4 lists the parameters reported by Kurukuri et al. [25] and Hasenpouth [18] from tension-compression tests and compares against values found in this work (Eq 4.20) from orthogonal cutting tests. The values generally compare well over the applicable ranges of state variables.

Table 4.4. ZA parameters comparison against Kurukuri et al. [61] and Hasenpouth [25].

	HCP ZA (This work)	Kurukuri et al. [61]	Hasenpouth [25]
C_0	163.53	152.7	177.452
B	324.2	349.5	160.095
B_0	304.82	from 287 to 304	573.813
β_0	0.0341	0.0039	0.0131
β_1	-0.0002	8.90E-04	1.39E-03

H. Conclusion

Oxley [27] thick shear zone analytical model is extended by utilizing a modified (to include a strain recovery term ε_r) HCP-Zerilli-Armstrong material constitutive law. This method extension resulted in the adaptation of the Oxley [27] thick shear zone approach by presenting an equivalent strain hardening index, n_{eq} , compatible with modified Zerilli Armstrong HCP-Zerilli-Armstrong material constitutive law. As an application for HCP metals, the method is applied via orthogonal cutting of AZ31B (a magnesium alloy considering its current popularity). A battery of orthogonal cutting tests was conducted on tubes made from AZ31B (a magnesium alloy) under a number of ranges cutting conditions of speeds and feeds.

Consequently, determined were a new set of ZA material parameters for AZ31B that were found to be capable of simulating the mechanical response of AZ31B under different conditions of state variables of strain, strain rates, and temperatures. Reported operating mean shear and tool chip interface temperatures for the investigated ranges of uncut chip thickness and cutting speed proved to be in agreement with machining temperatures reported by Nasr and Outeiro in [60] and Viswanathan et al. [59]. The newly found set of ZA material constitutive law parameters for AZ31B predicted well material flow stress data for the operating range of strain (0.01 to 0.1mm/mm), strain rate (500 s^{-1} to 300 s^{-1}) and temperature (45C to 250 C) reported by Feng et al. [55] and Hasenpouth [25] based on mechanical tests. The presented methodology for

inversely updating HCP- Zerilli -Armstrong material model parameters based on orthogonal cutting tests may serve as a complementary alternative to time-consuming mechanical flow stress experiments.

CHAPTER V

INCORPORATING DUAL BCC/FCC ZERILLI-ARMSTRONG AND BLUE BRITTLENESS CONSTITUTIVE MATERIAL MODELS INTO OXLEY'S MACHINING SHEAR ZONE THEORY

Presents an extension of Oxley's shear zone theory by substituting the original velocity-modified power form by the widely used constitutive material model developed by Zerilli and Armstrong (ZA). Used are variations of ZA constitutive laws capable of accounting for operating strains, strain rates, and temperatures as well as the appropriate crystal structure such as body-centered cubic (BCC) and face-centered cubic (FCC). This latter feature is useful in cutting simulations of metal alloys with complex phase diagrams (e.g., carbon steels) having temperature-dependent crystal structures.

Loss of ductility encountered at elevated temperatures, dubbed Blue brittleness (BB), adds another challenge to the simulations.

A. Introduction

Various forms of constitutive models that are capable of describing the mechanical response of materials have long been reported by Hamade and Ismail [35]. While incorporating a velocity-modified power form to describe material flow stress, Oxley in his analytical model presented in [27] of the 'thick shear zone' employed a material constitutive model that takes into account operating variables such as strain, strain rate, and temperature to predict the generated machining cutting forces. This analysis constituted an improvement to the geometric approach

based on the earlier thin shear plane analysis by Merchant [11]. Oxley [30] employed cutting tests of 0.2 % and 0.38 % Carbon steels to validate the thick shear zone analysis.

Incorporating proper constitutive models into cutting mechanics analyses plays an important role in returning sound predictions for such relevant outputs as generated cutting forces, chip thickness, and temperatures. Starting from force values generated from a limited number of drilling experiments, Seif et al. [54] utilized Oxley's [30] analysis to inversely identify Johnson and Cook [18] material model coefficients for Aluminum 6061-T6. Utilizing finite element simulations of steel orthogonal machining, Iqbal et al. [62] reported improved predictability of cutting forces using Oxley's [30] power form and Johnson-Cook formulation [18] compared to other constitutive model forms by Maekawa et al. [63] and Zerilli – Armstrong (for BCC crystalline material) [26]. Fang [64] reported on a sensitivity analysis considering these four material models and concluded that a slight change in the chemical composition and microstructure due to heat treatment could affect the constitutive equation parameters.

Steels, characterized for having multi-crystalline structures at different operating temperatures Long and Leighty [65], are particularly challenging to model. As an added complication, steels exhibit loss of ductility (dubbed blue brittleness) at elevated temperatures by Long [28]. As reported by Ding and Shin [66], Oxley power form [30] for the material model can account for effects emanating from both blue brittleness and crystal structure evolution.

Incorporating more commonly used models into Oxley's [30] shear zone formulations would provide for a suitable alternative to predicting cutting forces in metal machining. For example, Lalwani et al. [19] incorporated the Johnson-Cook [18] material model in Oxley's thick shear zone formulation.

Grounded in the crystal structure's physical aspects of thermodynamics, slip, and dislocation dynamics, the Zerilli-Armstrong (ZA) constitutive model [26] accounts for such salient state variables as operating strain, strain rate, and temperature. This model is attractive since its formulations are readily available for many commonly machined materials with BCC, FCC, and HCP crystalline structures. As originally proposed, ZA flow stress formulation for body-centered cubic (BCC) is described by

$$\sigma = c_0 + c_1 \exp\left(-c_3 T + c_4 \ln\left(\frac{\dot{\varepsilon}}{\dot{\varepsilon}_0}\right)\right) + c_5 \varepsilon^n \quad (5.1)$$

Where the terms presented by σ , ε , $\dot{\varepsilon}/\dot{\varepsilon}_0$ and T are the operating stress, strain, normalized strain rate, and temperature. The normalized strain rate is a ratio of the equivalent strain rate $\dot{\varepsilon}$ to reference strain rate $\dot{\varepsilon}_0$. The terms c_0 , c_1 , c_2 , c_3 , c_4 , c_5 , and n are Zerilli – Armstrong material constants are determined by fitting against experimental mechanical response data.

The ZA flow stress formulation for face-centered cubic (FCC) materials originally reported in [26] by

$$\sigma = c_0 + c_2 \varepsilon^n \exp\left(-c_3 T + c_4 \ln\left(\frac{\dot{\varepsilon}}{\dot{\varepsilon}_0}\right)\right) \quad (5.2)$$

Lesuer [67] assessed the deformation of Aluminum 6061-T6 under large strains and high strain rates and found that ZA to fit the response better than other tested constitutive models (Gurson void growth [68] and Johnson-Cook [18] models). Jaspers et al. [69] in their work reported ZA BCC model coefficients for AIS1045 steel operating temperature lower than 650 °C matching with complete ferrite BCC solid solution. Mirzaie et al. [70] studied the material response of AIS1045 steel at elevated temperature matching with the complete austenite FCC solid solution to find steel ZA FCC coefficients. Considering blue brittleness encountered in

AISI 1045 steel, Zaeh et al. [71] suggested an additive term (σ_B) to ZA BCC constitutive equation function of operating temperature, T, and material-specific peak blue brittleness temperature, T*, of the form

$$\sigma_B = c_6 \exp(-c_7(T - T^*)^2) \quad (5.3)$$

Where c_6 and c_7 are material-specific parameters experimentally determined. Zerilli – Armstrong constitutive models [26] used for modeling a wide range of metals in manufacturing processes, also Zerilli – Armstrong [26] provide different material models function of the metal crystal structure, proposed in this manuscript the extension of Oxley [30] machining prediction methodology accounting for both Zerilli – Armstrong body-centered cubic (BCC) and face-centered cubic (FCC) type material models.

The Oxley [27] methodology extension performed through finding thick shear zone parameters compatible with Zerilli-Armstrong BCC and FCC material models and accounting for blue brittleness caused by localized precipitate formation Long [28]. Validation of the Oxley ZA FCC methodology performed through comparison with published orthogonal cutting tests reported by Adibi et al. [29] and Guo [21], also performance of the Oxley ZA BCC/FCC dual-material model methodology is justified through comparison with orthogonal tests reported by Oxley [30] and Lalwani et al. [19]. The methodology advanced incorporates the Zerilli-Armstrong dual BCC and FCC models, and blue brittleness model dubbed ZA-BB.

B. Oxley's thick shear zone analytical model

Metal cutting involves large material plastic deformation at the primary deformation zone in the vicinity of the shear plane, at the secondary deformation zone occurring at the tool-chip interface, and at the tertiary deformation zone occurring at the clearance side of the tool

Okushima and K. Hitom [72] and Zorev [73]. Considering the dominant magnitude of plastic deformation occurring at the primary and secondary deformation zones, Oxley [30] developed an analytical model for the shear zone based on the continuous flow principle of the material throughout the shear plane to the formed chip. For predicting the cutting force components, the model requires a material constitutive model and process variables such as tool geometry and cutting parameters (e.g., feed and speed).

Identification of the state variable values of strain, strain rate, and temperatures occurring at the primary and secondary deformation zones are needed for determining the corresponding flow stress using Oxley [30] defined a power form flow stress. As illustrated in Figure 5.1, Oxley [30] analysis aims to determine the resultant shear angle, ϕ , primary deformation zone of thickness, S_1 , and secondary deformation zone of thickness, S_2 , at conditions that satisfy equilibrium between shear transmitted forces and tool-chip interface forces.

Both shear plane-transmitted forces and tool-chip interface forces are found using the material flow stress model estimated function of operating strain, strain rates, and temperatures at the primary and secondary deformation zones, respectively.

Oxley [30] assumed a perfectly sharp tool, thus neglecting plowing forces and deformations occurring at the tertiary zone. The primary deformation zone thickness ratio, $C' = l/S_1$, is defined as the ratio of shear plane AB length is (l) to the thickness of the primary shear zone (S_1).

The secondary deformation zone boundary thickness ratio $\delta = S_2/t_2$ defined as the ratio of the thickness of secondary deformation zone located at the tool-chip interface (S_2) to the chip

thickness, t_2 , and shear angle are found at the state where these conditions are simultaneously satisfied

- 1- Minimum k_{chip}
- 2- $\sigma'_N = \sigma_N$
- 3- $\tau_{chip_{int}}$

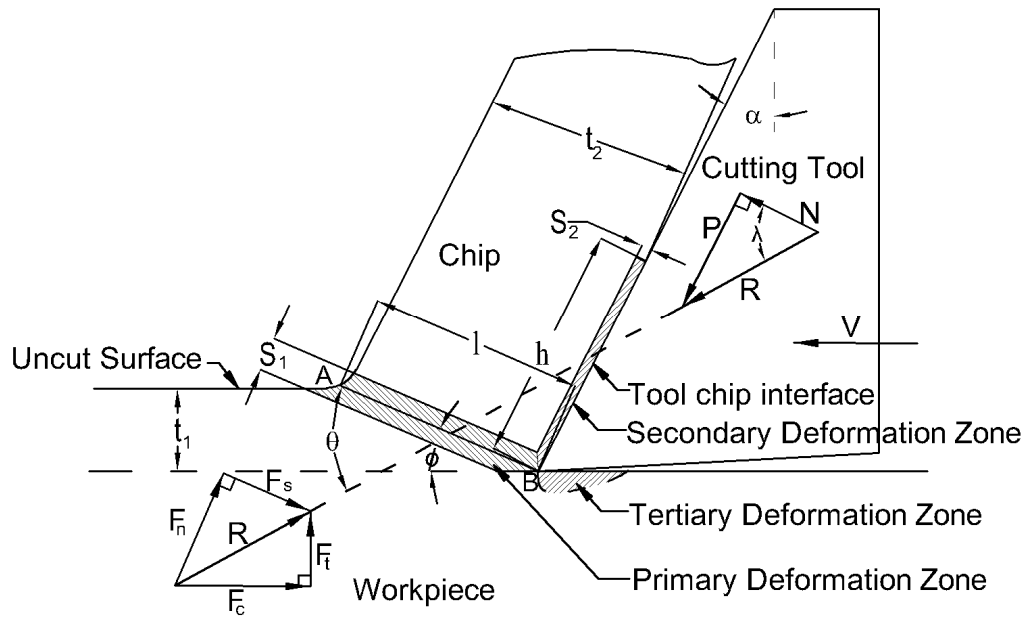


Figure 5.1. Shear zone's orthogonal cutting parameters and force components.

Where k_{chip} is the material shear stress at the tool-chip interface calculated based on chip strain and velocity modified temperature occurring at the tool/chip interface secondary deformation zone. Illustrated in Figure 5.2 flowchart Oxley's [30] thick shear zone analysis.

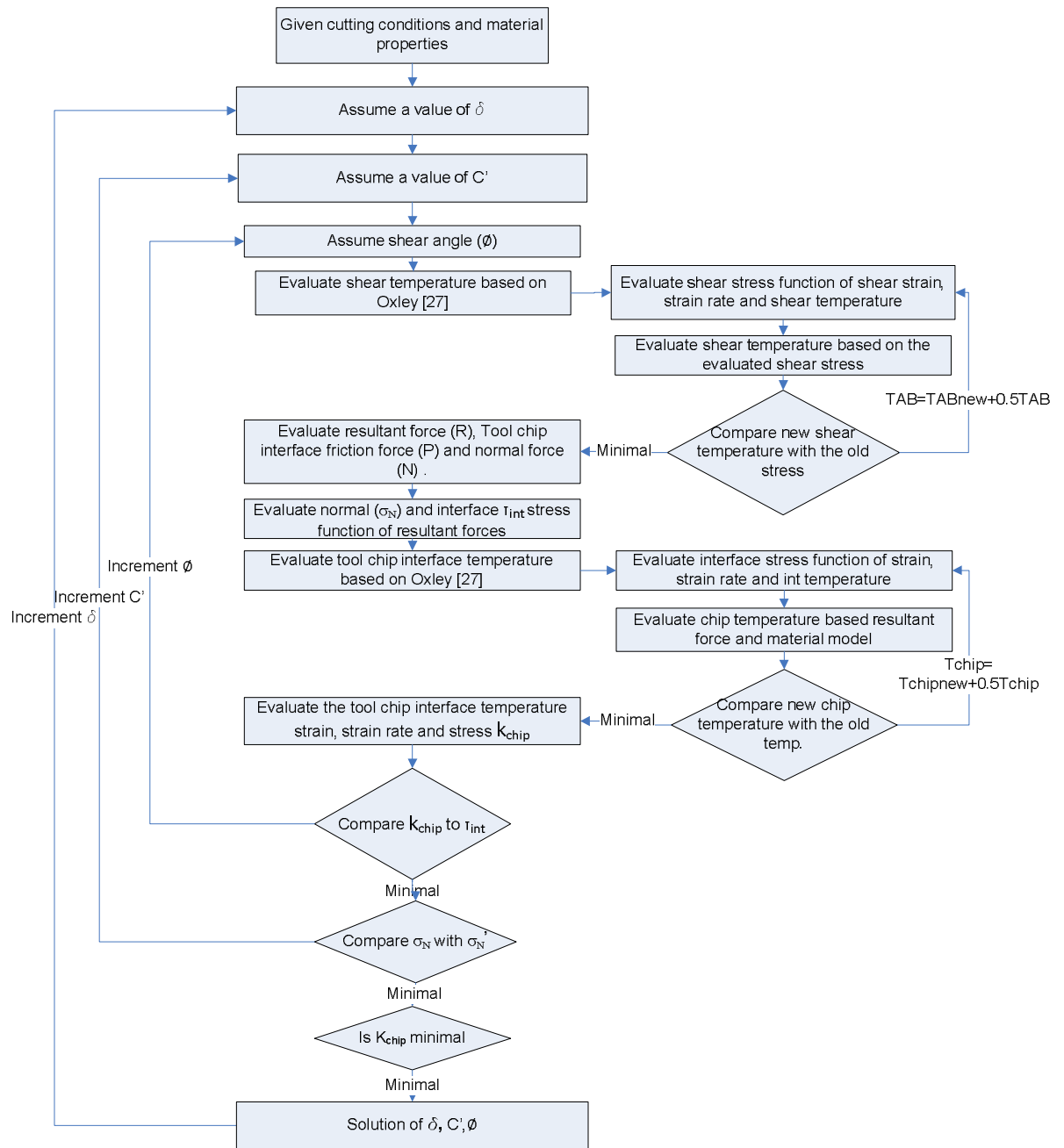


Figure 5.2. Flowchart for Oxley's [30] thick shear zone analysis

The tool-chip interface shear stress, τ_{int} , is calculated using cutting tool friction force (P) divided by the tool-chip contact area ($h \cdot w$) where h is the tool-chip contact length (as determined later in Eq. (5.4), and w is the chip width.

$$h = \frac{t_1 \sin \theta}{\cos \lambda \sin \phi} \left[1 + \frac{C'n'}{3(1 + 2(\pi/4 - \phi) - C'n')} \right] \quad (5.4)$$

The terms denoted t_1 and t_2 are the uncut and cut chip thicknesses, respectively. The cutting angles terms reported as α , λ , and θ are as follows: tool rake angle, tool-chip interface friction angle, and the angle between resultant force R and shear plane angle, respectively reported in Figure 5.1.

The cutting force terms F_c , F_t , P , N , F_s , and F_n also shown on Figure 5.1 are defined as the cutting force in tool velocity (V) direction, thrust force perpendicular to tool velocity (V) direction, friction force and normal force at the tool-chip interface, shear force and normal force at the shear plane, respectively.

The mean normal stress σ_N at the chip-tool interface is a function of tool-chip interface normal force (N), tool-chip contact length (h), chip width (w) and calculated as:

$$\sigma_N = N/(hw) \quad (5.5)$$

And the normal stress is σ'_N found using the stress boundary at point B function of rake angle, α , primary deformation zone thickness ratio C' , and temperature modified strain hardening index n_{eq}

$$\sigma'_N = k_{AB} (1 + 0.5\pi - 2\alpha - 2C'n_{eq}) \quad (5.6)$$

Based on the solution shear angle, ϕ , the chip thickness, t_2 , and force components shown in Figure 5.1 are determined from orthogonal machining geometric relation described by Oxley [30] and Stabler [41].

C. Tasks Involved In Executing The Methodology

Presented a methodology for extending Oxley's [30] thick shear zone approach to account for Zerilli – Armstrong [26] body-centered cubic (BCC) and/or face-centered cubic (FCC) type material models. To this end, the required tasks are listed in Figure 5.3, which presents a flowchart illustrating the development and validation tasks for extending a thick shear zone approach to include ZA flow stress models for dual FCC/BCC materials.

Task 1 Formulation of the ZA-extended Oxley's for single (BCC or FCC) phase materials (detailed in Section 5.4)

In this task, the re-formulation of the Oxley analysis requires identifying a suitable BCC or FCC type Zerilli-Armstrong strain hardening index (n_{eq}) as per either Eq. 5.8 or 9. The appropriate n_{eq} equation must be chosen depending on whether BCC or FCC type crystals are used based on derivative evaluation of the shear flow stress (k_{AB}) variation across the shear zone thickness (S_1 in Eq. A1).

Task 2 Validation of ZA-extended Oxley's for single (BCC or FCC) phase materials: Aluminum 6061-T6 (detailed in Section 5.5)

Considering that Aluminum 6061-T6 is widely used and considering that its crystal structure is of the FCC type, cutting this material is used as validation for the Oxley-FCC Zerilli-Armstrong extended methodology. Cutting forces found using the developed methodology compared well with force values reported in the literature for orthogonal tests at the same cutting conditions.

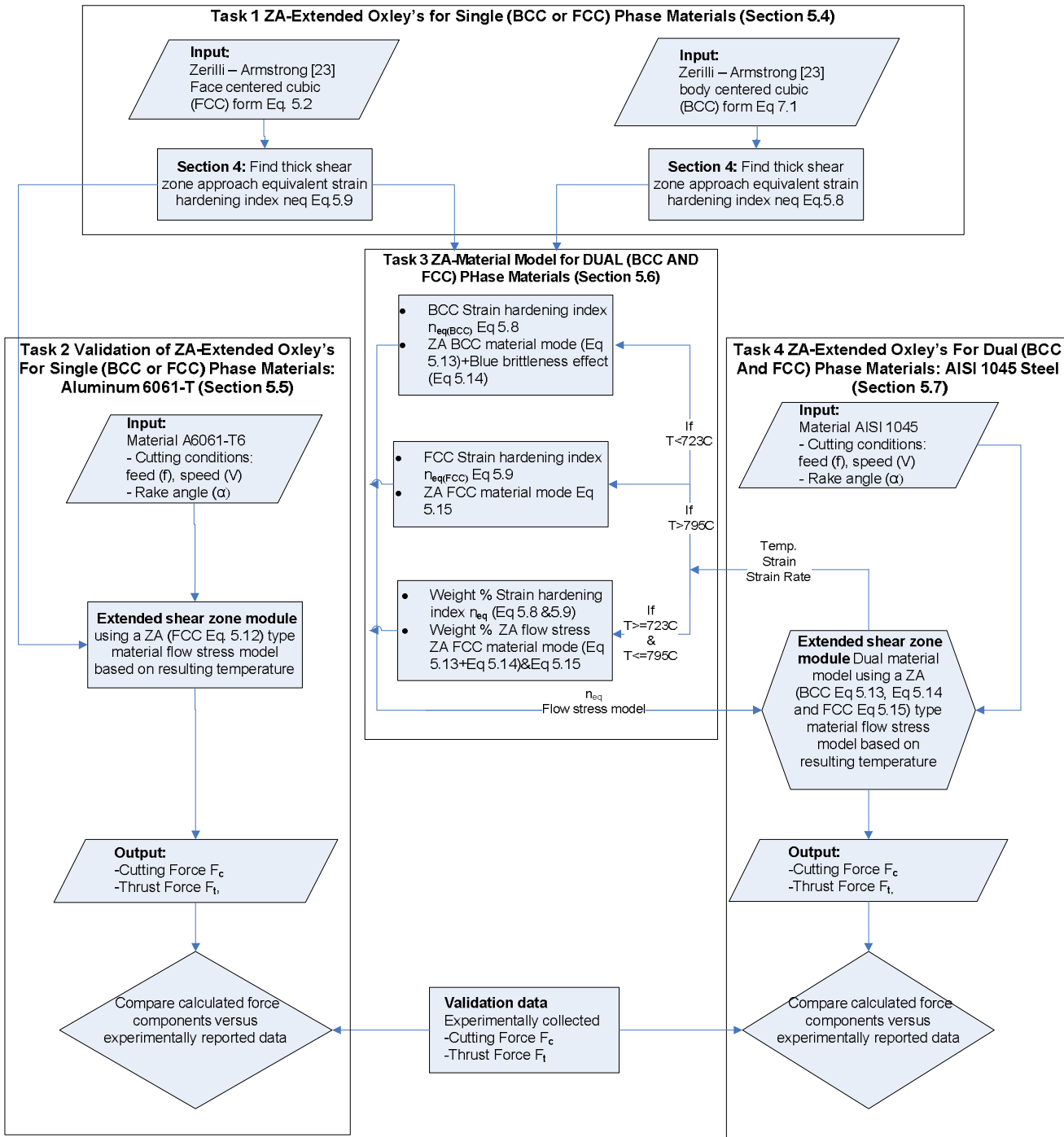


Figure 5.3. Flowchart illustrating the development and validation process for extending the thick shear zone to include ZA flow stress models for dual FCC/BCC materials.

Task 3 ZA-Material Model for Dual (BCC and FCC) Phase Materials (detailed in Section 5.6)

The material response of steels varies as a function of temperature where encountered in the region of 500°C to 700°C function of steel carbon content, a loss of ductility phenomena defined as blue brittleness Long [28] due to precipitate formation.

Also, examining the phase diagram for alloy steels shows how the material changes between a BCC ferrite and an FCC austenite solid solutions depending on the steel operating temperature crystal structure defined by Long and Leighty [65]. Considering different machining conditions generate different temperatures in the shear deformation zone. This methodology conceives a BCC/FCC Zerilli-Armstrong based material model that accounts for the effect of steel crystal structure change in addition to blue brittleness effect with Application of AISI 1045 steel.

Task 4 ZA-extended Oxley's for dual (BCC and FCC) phase materials: AISI1045 steel (detailed in Section 5.7)

Validation of the dual constitutive model approach achieved by comparing the methodology's generated cutting force predicted values against published orthogonal cutting forces. Offered improved predictability of steel cutting forces by adopting a dual BCC/FCC material models that can account for the generated temperatures along with its effect on the material crystal structure.

D. Za-extended Oxley's for single (bcc or fcc) phase materials (task 1)

Illustrated here is how we extend Oxley's parallel-sided thick zone analysis to incorporate a Zerilli-Armstrong material model. The machining forces calculated while

accounting for the material's crystal structure as well as the cutting parameters (e.g., feed and speed). The following assumptions made:

- 1) Large width to uncut chip thickness ratio to satisfy plane strain condition
- 2) The cutting tool is perfectly sharp, and no plowing force is involved.
- 3) Chip flow freely with no build-up at the tool-chip interface.
- 4) Cutting speed is constant.
- 5) Orthogonal cutting condition satisfied with a straight cutting-edge perpendicular

to the cutting velocity direction.

By assuming a linear distribution of normal stress along shear plane AB , Oxley [30] formulated the angle θ , formed between the resultant force, R and shear plane is presented in Figure 5.1 as

$$\tan(\theta) = 1 + 2 \left(\frac{\pi}{4} - \phi \right) - \left(\frac{\delta k}{\delta s_1} \right) \frac{1}{2k_{AB}} \quad (5.7)$$

And the term $\left(\frac{\delta k}{\delta s_1} \right) \frac{1}{2k_{AB}}$ is defined as $C' n_{eq}$ by Oxley [30] where the primary deformation zone thickness ratio C' is found through the thick shear analysis iterative methodology and Oxley [30] equivalent strain hardening index n_{eq} formulated in appendix 2 function of material model parameters.

Reference to Figure 5.4 formulation and as detailed in Appendix 2, The Oxley [30] equivalent strain hardening index $n_{eq}(\text{BCC})$ for Zerilli–Armstrong BCC material approximated as reported in Eq. (5.8).

$$n_{eq}(\text{BCC}) = \frac{n C_5 \varepsilon^n}{C_0 + C_1 e^{\left(-C_3 T + C_4 T \ln \left(\frac{\dot{\varepsilon}}{\dot{\varepsilon}_0} \right) \right) + C_5 (\varepsilon)^n}} \quad (5.8)$$

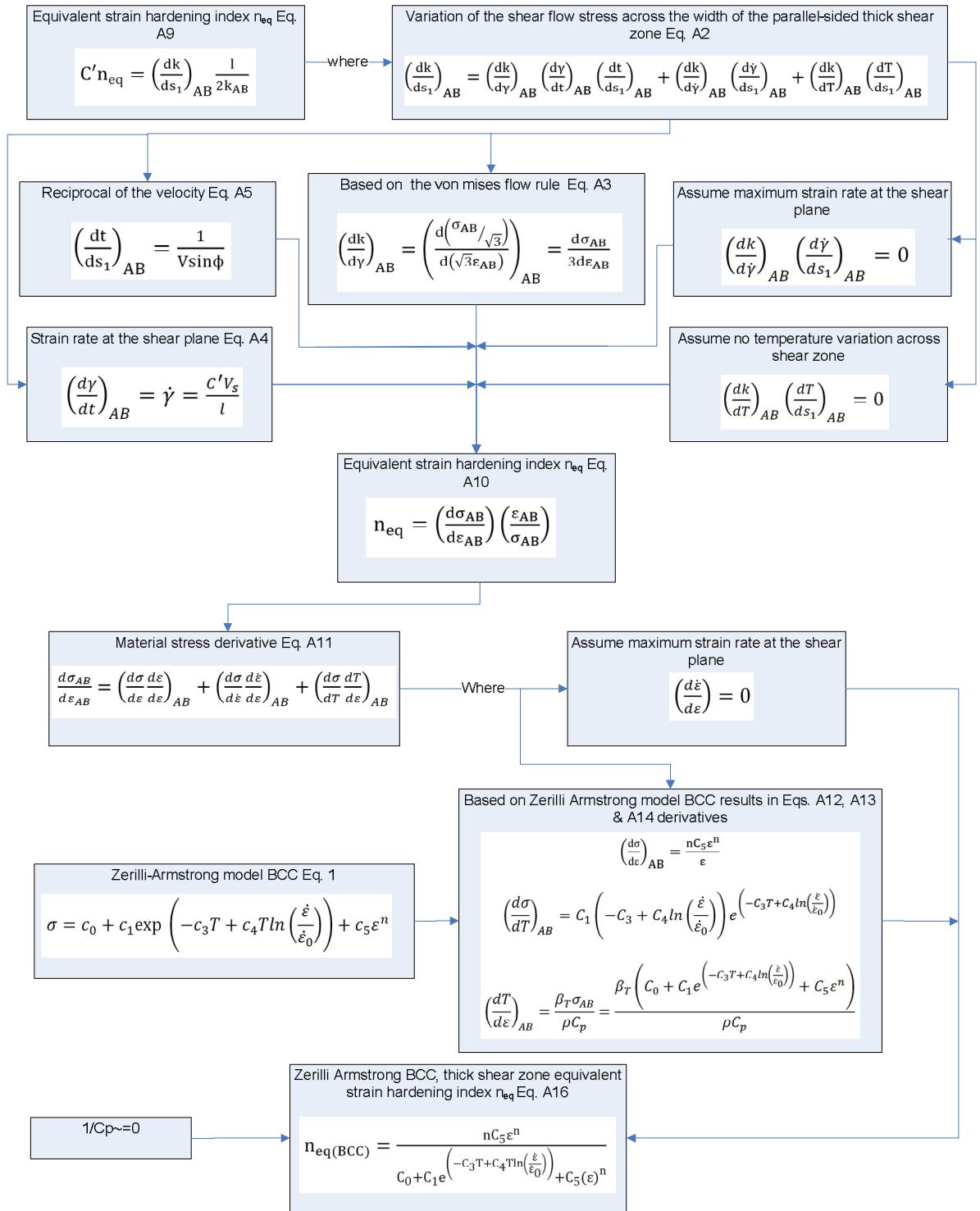


Figure 5.4. Flowchart illustrating the Zerilli-Armstrong thick shear zone extension methodology

The equivalent strain hardening index $n_{eq}(BCC)$ reported in Eq. 5.8 is also applicable for Zerilli–Armstrong (BCC) material model with blue hardness additive term defined in Eq. 5.3.

Inline with Lalwani et al. [19] Oxley approach extension and following methodology presented in Figure 5.4 flowchart and appendix 2, the equivalent strain hardening index $n_{eq}(FCC)$ using Zerilli–Armstrong (FCC) with material flow stress described in Eq. 5.2, is approximated by

$$n_{eq}(FCC) = \frac{n_{C_2} \varepsilon^{n_e} e^{-C_3 T + C_4 T \ln\left(\frac{\dot{\varepsilon}}{\dot{\varepsilon}_0}\right)}}{C_0 + C_2 \varepsilon^{n_e} \left(-C_3 T + C_4 T \ln\left(\frac{\dot{\varepsilon}}{\dot{\varepsilon}_0}\right)\right)} \quad (5.9)$$

The tool-chip contact length (h) and normal stress at point B (σ'_N) given by Oxley [30] are revised for ZA-extended Oxley's BCC and FCC flow stress models by replacing n' by with $n_{eq}(BCC)$ or $n_{eq}(FCC)$ as

$$h = \frac{t_1 \sin \theta}{\cos \lambda \sin \phi} \left(1 + \frac{C' n_{eq}[(BCC) \text{ or } (FCC)]}{3 \left(1 + 2 \left(\frac{\pi}{4} - \phi \right) - C' n_{eq}[(BCC) \text{ or } (FCC)] \right)} \right) \quad (5.10)$$

$$\sigma'_N = k_{AB} \left(1 + \frac{\pi}{2} - 2\alpha - 2C' n_{eq}[(BCC) \text{ or } (FCC)] \right) \quad (5.11)$$

E. Validation of Za-Extended Oxley's For Single (Bcc Or Fcc) Phase Materials: Aluminum 6061-T6 (Task 2)

Provided in this segment validation of the methodology reported in Appendix 2 and laid out in Section 5.4. Having an FCC crystal structure and considering its common use, Aluminum 6061-T6 is a good metal candidate used for methodology validation. Lee et al. [74] conducted compression tests on Aluminum 6061-T6 at elevated temperature conditions and strain rates larger than 103 s^{-1} and reported ZA FCC model as

$$\sigma = 156.7 + 710.4\epsilon^{0.624} \exp\left(-0.0055T + 0.00044T \ln\left(\frac{\dot{\epsilon}}{\dot{\epsilon}_0}\right)\right) \quad (5.12)$$

Figure 5.5 shows flow stress data for Aluminum 6061-T6, according to Zerilli-Armstrong FCC model by Lee et al. [74] and compared to those of Johnson-Cook [36] material model. Material response reported by Lee et al. [74] based on compression data for operating temperatures range from 100oC and 350°C, strains from 0.05 to 0.7mm/mm, and strain rates from 0.001 to 5000 s⁻¹ similar to loading conditions encountered in machining.

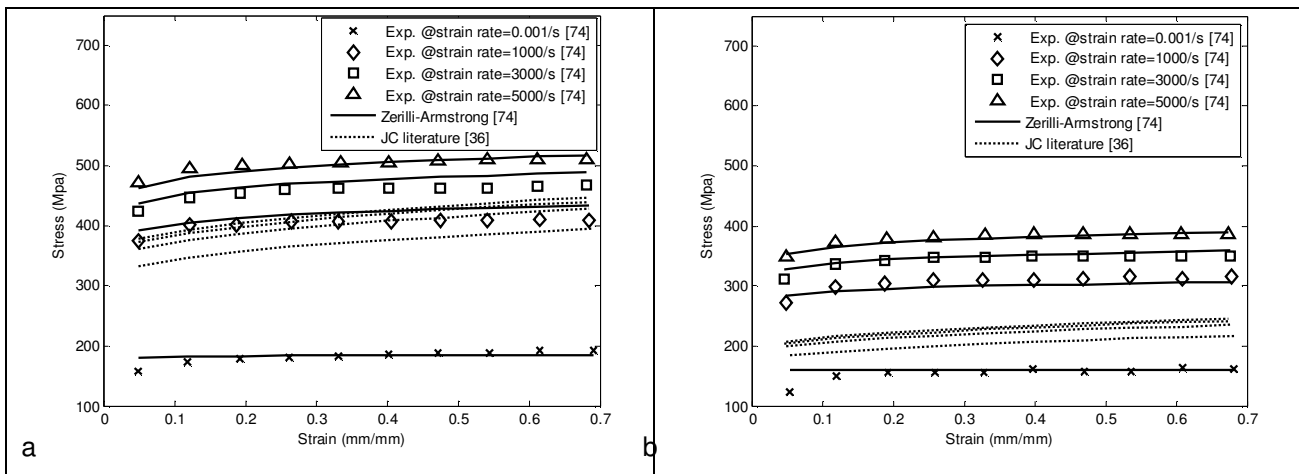


Figure 5.5. Aluminum 6061-T6 flow stress according to ZA [74] and JC [36] models as compared with experimental data [74] at temperatures: a) 100 °C, and b) 350 °C.

Figure 5.5 shows improved strain rate effect predictability of the Zerilli-Armstrong material model (Lee et al. [74]) as compared with Johnson Cook [36] material model for Aluminum 6061-T6 reported by Lesueur [67] at strain rates higher than 10³ s⁻¹.

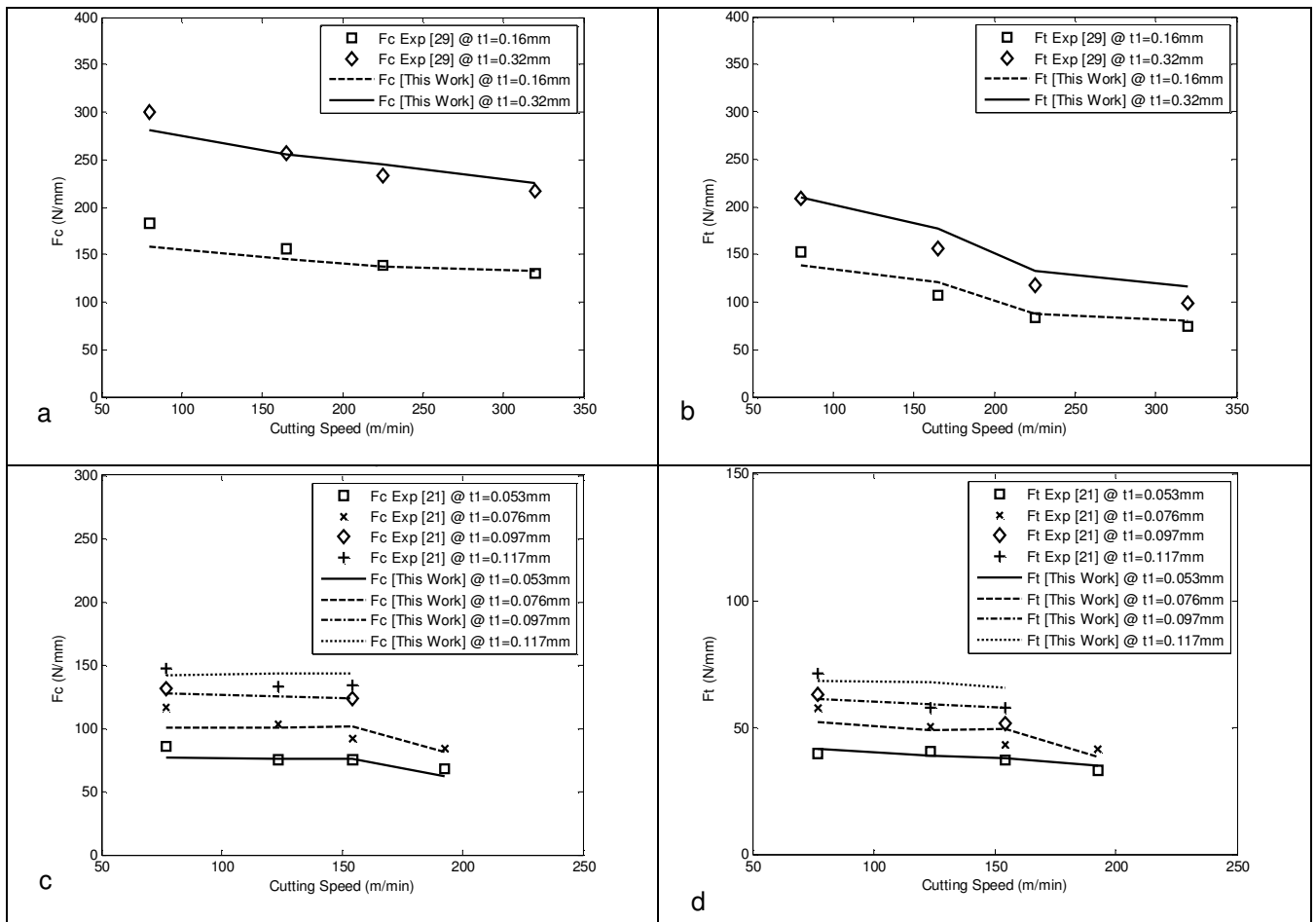


Figure 5.6. Cutting force components for Al 6061-T6: Experimental data (Adibi et al. [29], Guo [21]) and Oxley-ZA extended methodology results (this work): a) Cutting Force Component at 8° rake angle, b) Thrust Force Component at 8° rake angle, c) Cutting Force Component at 6° rake angle, d) Thrust Force Component at 6° rake angle.

Considering the high deformation rates involved in machining processes and considering the improved predictability of the Zerilli-Armstrong material model to predict dynamic stress at high deformation rate the thick shear zone approach of Zerilli-Armstrong extension methodology is expected to present an enhancement for the predictability of machining forces of Aluminum 6061-T6 at high cutting speeds.

Thick shear zone Zerilli-Armstrong FCC extension is utilized with strain hardening index $n_{eq}(FCC)$ (Eq. 5.9) and the methodology presented in Section 5.3. To validate the ZA-Oxley extension comparison with reported orthogonal cutting experiments published by Adibi et

al. [29]. Validation data were generated using cutting experiments performed on Aluminum 6061-T6 tubes of diameter 57mm and a wall thickness of 3mm using Kennametal grade K68 sharp tools with 80 rake angle at varying operating conditions of cutting speed and feed rate as reported by Adibi et al. [29].

Also utilized are orthogonal cutting experiments generated by Guo [21] using (K-type carbide) sharp tools with 60 rake angle for cutting Aluminum 6061-T6 tubes of 50.8mm diameter and 1.7mm wall thickness at varying operating conditions of cutting speed and feed rate. As shown in Figure 5.6 (a,b,c,d) developed methodology proved to predict well cutting and thrust forces where a mean absolute value difference of 5.2 % and 8.7% achieved respectively.

The goodness of the methodology is validated using the R2 parameter which returns the square of the Pearson Product-Moment Correlation Coefficient for the thrust and cutting force prediction versus experimentally obtained forces reported by Adibi et al. [29] and Guo[21]. Values that were closer to unity R2 indicate enhanced matching between model-generated forces and experimentally collected forces.

Table 5.1 lists calculated R squared (R2) values for cutting force F_c is 0.97, and for thrust force, F_t is 0.97, which proves the predictability of the cutting and thrust forces using the developed methodology.

Table 5.1 Aluminum 6061-T6 Orthogonal tests summary.

Test #	Rake angle (°)	Cutting Speed (m/min)	Feed (mm)	Exp. (N/mm), Jaspers et al. [82] & Pleta et al. [49]		Oxley (N/mm) [This work]		Diff. %, Oxley (N/mm) [This work]	
				F _c	F _t	F _c	F _t	F _c	F _t
1	8	80	0.16	183.4	153	159.2	138.5	13.20%	9.50%
2	8	165	0.16	156.3	106.5	146.3	121.4	6.40%	14.00%
3	8	225	0.16	138.8	83.1	137.3	87.5	1.10%	5.30%
4	8	320	0.16	130.8	74.8	132.7	80.3	1.50%	7.40%
5	8	80	0.32	299.8	209.1	281.3	210.3	6.20%	0.60%
6	8	165	0.32	256.8	156.3	255.3	177.5	0.60%	13.60%
7	8	225	0.32	232.9	117.5	245.3	132.8	5.30%	13.00%
8	8	320	0.32	216.9	99.1	225.3	116.5	3.90%	17.60%
9	6	77.1	0.053	85.6	39.5	76.5	41.6	10.60%	5.30%
10	6	123.42	0.053	75.4	40.5	75.9	39.5	0.70%	2.50%
11	6	154.26	0.053	75.3	36.9	75.8	37.9	0.70%	2.70%
12	6	192.84	0.053	67.9	33.2	61.6	35.5	9.30%	6.90%
13	6	77.1	0.076	116.2	57.7	100.7	52.3	13.30%	9.40%
14	6	123.42	0.076	102.9	50.4	100.2	48.7	2.60%	3.40%
15	6	154.26	0.076	91.8	43.2	101.7	49.2	10.80%	13.90%
16	6	192.84	0.076	83.7	41.4	81.3	38.2	2.90%	7.70%
17	6	77.1	0.097	131	62.8	128.3	61.2	2.10%	2.50%
18	6	154.26	0.097	123.2	51.5	123.4	57.7	0.20%	12.00%
19	6	77.1	0.117	147.1	71.4	141.3	68.1	3.90%	4.60%
20	6	123.42	0.117	132.5	57.8	143.2	67.6	8.10%	17.00%
21	6	154.26	0.117	134.1	57.5	143.5	65.4	7.00%	13.70%
R2 Fc, Ft Methodology versus Fc, Ft Exp.				0.97	0.97	-	-	-	-
Average %Difference: Fc, Ft Methodology versus Fc, Ft Exp.				-	-	5.20%	8.70%	-	-

Also, part of the thick shear zone Zerilli-Armstrong FCC extension validation, reported in Figure 5.7 good agreement between predicted chip thickness compared to experimentally measured chip thickness by Adibi et al. [29] and Guo [21] at operating conditions stated in Table 5.1 and mean predictability difference of 7.1%.

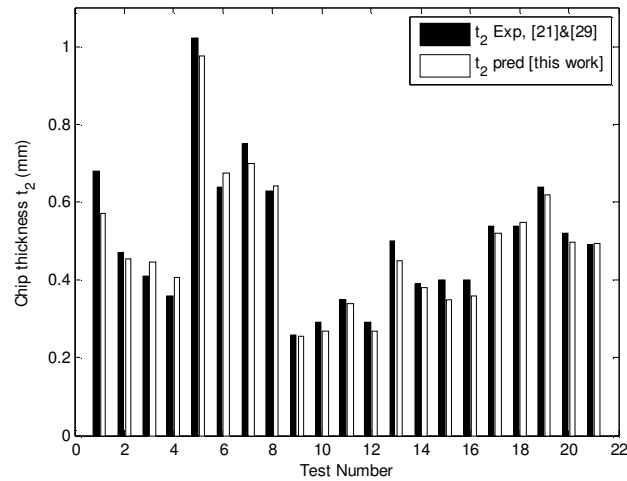


Figure 5.7. Chip thickness for Al 6061-T6: Experimental data (Adibi et al. [29], Guo [21]) and Oxley-ZA extended methodology results

F. Za-material model for dual (bcc and fcc) phase materials (task 3)

Oxley [30] conceived a power form material model accounting for both elevated temperature ductility loss and crystal structure changes effects where a modified temperature (T_{mod}) term function of strain rate is utilized to model the varying strain hardening effect function of operating temperature and strain rate reported by Ding and Shin [66] for both 0.2% carbon steel and 0.38% carbon steels. In this manuscript, AISI 1045 steel utilized as validation material for extending Oxley's analytical model [30] to dual BCC/FCC Zerilli-Armstrong material model. Based on the iron-carbon phase diagram presented by Long and Leighty [65] steels reported at zero strain rate conditions is an important guidance for the microstructural composition related to the widely used AISI 1045 steel. Where the investigated steel shows the full composition of ferrite solid solution (BCC crystal structure) at temperatures lower than 723°C and austenite solid solution (FCC crystal structure) at temperatures higher than 795°C with neglect of pearlite constituent at up to 975 °C. Dual-crystal structures such as AISI 1045 steel is defined by two Zerilli-Armstrong [26] constitutive models: one for operating temperature lower than 723 C

based on the BCC (Eq. 5.13) and for operating temperature higher than 795C based on FCC material model form (Eq. 5.15).

The BCC type Zerilli-Armstrong material model reported by Jaspers et al. [69] for AISI 1045 material based on experimental compression test data reported are for an operating temperature ranging from 100°C to 500° C, strain rate from 0.001 to 7500 s⁻¹ and strain from 0.05 to 0.3mm/mm similar to conditions encountered during machining process utilized for 1045 steel at temperatures lower than 723C.

$$\sigma = 159.2 + 1533.7 \exp\left(-6.09 \cdot 10^{-3} T + 1.89 \cdot 10^{-4} T \ln\left(\frac{\dot{\epsilon}}{\dot{\epsilon}_0}\right)\right) + 742.6 \epsilon^{0.171} \quad (5.13)$$

To account for precipitate hardening effect encountered with steel material defines a steel blue brittleness Long [28] an additive term(σ_B) for Zerilli-Armstrong [26] BCC constitutive models conceived by Zaeh et al. [71] for an operating temperature lower than 723oC defined as

$$\sigma_B = 50.2 \exp(-0.0003(T - 673)^2) \quad (5.14)$$

Figures 5.8a and 5.8c report comparison between published experimentally collected dynamic stress data published by Jaspers, [69] at varying strain and operating conditions versus working temperature and strain, respectively. As shown in Figures 5.8a and 8c, Jaspers et al. [69] Johnson Cook and Zerilli-Armstrong BCC material models coupled with Eq. 5.14 blue brittleness additive term predicted well experimentally collected data at temperatures lower than the steel phase change temperature of 723oC.

For AISI 1045 steel operating at temperatures from 795oC to 1100oC, the FCC Zerilli-Armstrong constitutive material model type reported by Mirzaie et al. [70] generated using

compression tests at a temperature ranging from 900oC to 1100oC, strain rate from 0.001 to 0.1 s⁻¹ and strain from 0.05 to 0.7mm/mm.

$$\sigma = 6771.175\epsilon^{0.232}\exp\left(-0.002953T + 0.00012T\ln\left(\frac{\dot{\epsilon}}{\dot{\epsilon}_0}\right)\right) \quad (5.15)$$

Shown in Figures 5.8b and 5.8d, comparison between published experimentally collected dynamic stress data by Mirzaie et al. [70] for the AISI 1045 and Oxley [30] 0.38 % steel, Johnson Cook reported by Jaspers et al. [69] and Zerilli-Armstrong FCC Mirzaie et al. [70] material models. Reported in Figures 5.8b and 5.8d Oxley [30] 0.38 % steel material model and Mirzaie et al. [70] AISI 1045 FCC Zerilli-Armstrong FCC models good predictability of Mirzaie et al. [70] experimentally collected dynamic stress data at the stated dynamic conditions.

Figures 5.8a and 5.8c Johnson cook, Oxley, and BCC Zerilli-Armstrong constitute model predict well the behavior of the AISI 1045 steel at a temperature lower than 700 oC. At operating temperature higher than 700 °C as presented in Figures 5.8b and 5.8d, Johnson Cook reported by Jaspers et al. [69] material model loses predictability compared to the Oxley model and AISI 1045 FCC Zerilli-Armstrong elevated temperature FCC material model. Johnson Cook AISI 1045, presented by Jaspers et al. [69], diminished accuracy at high temperature is correlated with the lack of modeling steel crystal structure change effect.

For an operating temperature of 723°C to 795°C, defined as AISI 1045 phase change temperature range reported by Long and Leighty [65], both ferrite (BCC) and austenite (FCC) solid solutions coexist, a dual Zerilli-Armstrong material model composition utilized. A compounded BCC/FCC material model is generated based on temperature varying weight fraction interpolation function of BCC type Zerilli-Armstrong Eq. 5.13 and FCC Zerilli-Armstrong Eq. 5.15, as reported by Ding and Shin [66].

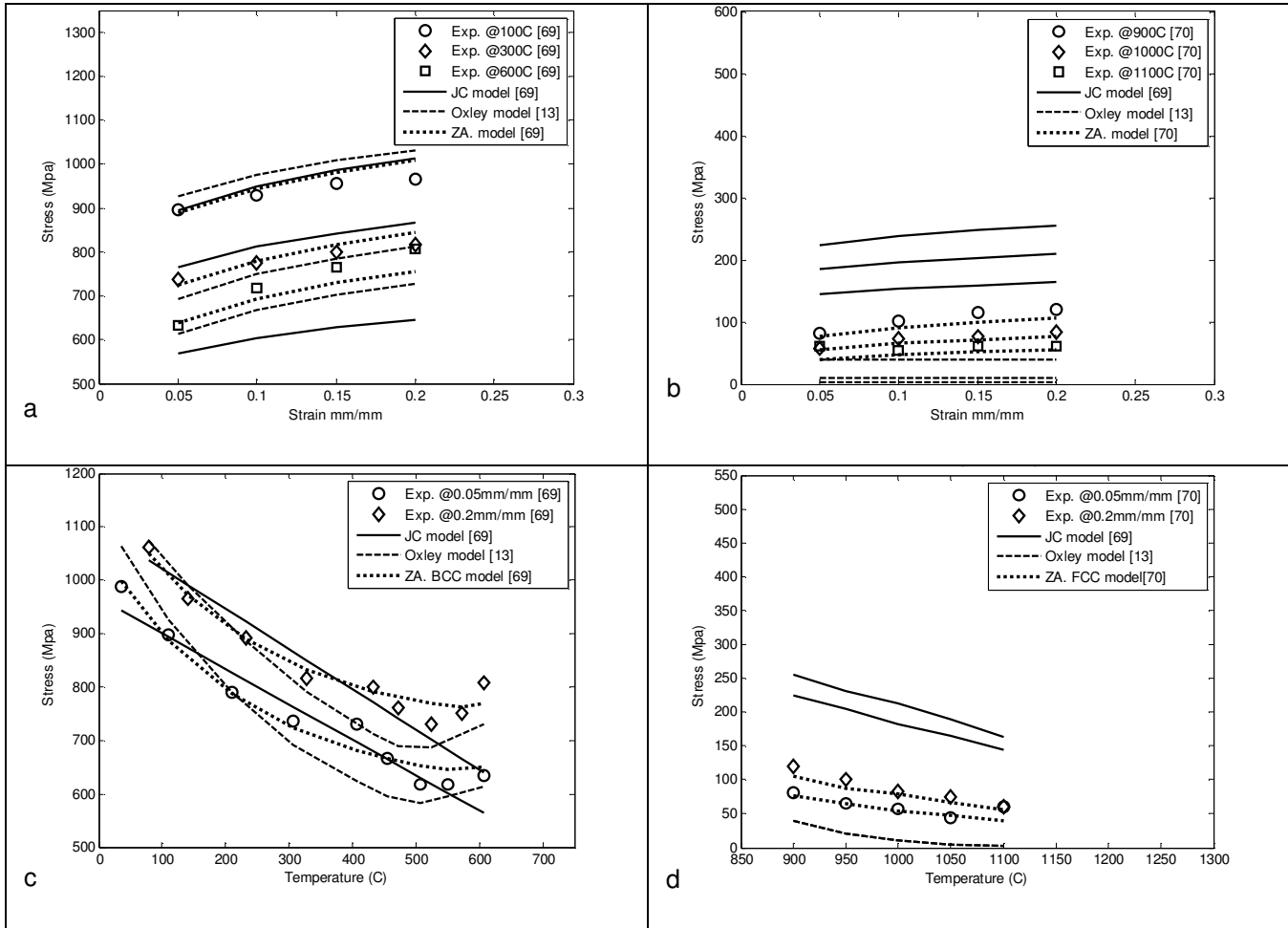


Figure 5.8. AISI-1045 flow stress for Oxley, JC, and ZA constitutive models compared with experimental data ([69],[70]): a) for BCC crystal structure versus strain, b) for FCC crystal structure versus strain, c) for BCC crystal structure versus temperature, d) for FCC crystal structure versus temperature.

To evaluate the accuracy of the conceived Zerilli-Armstrong dual-material model, comparison with published material models widely used in thick shear zone approach cutting force predictions such as Oxley [30], Johnson cook reported by Jasper et al., [69] and modified Johnson-Cook reported by Sartkulvanich et al. [75] performed for AISI 1045 material.

Figure 5.9a defines the different regions adopted incorporation of Zerilli-Armstrong based material model function of temperature described as four areas controlling the material

model which are, BCC, BCC-Blue Brittleness, dual BCC-FCC, and FCC regions reported at a strain of 0.7mm/mm, strain rate of 10000 s^{-1} . Figure 5.9 b reports matching the performance of the developed AISI 1045 Zerilli-Armstrong dual-material model with Sartkulvanich et al. [75] published AISI 1045 material model at a strain of 0.7mm/mm, strain rate of 10000 s^{-1} and a temperature range from 50°C to 1200°C coinciding with conditions encountered in machining processes.

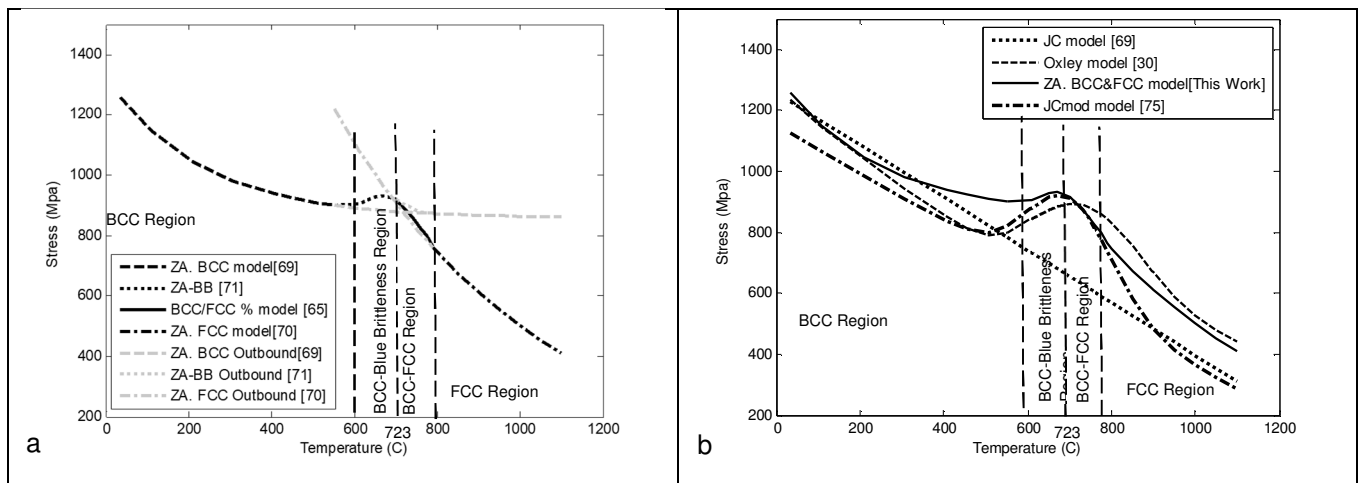


Figure 5.9 Methodology ZA based material model definition a) function of temperature b) comparison versus Oxley [30], Johnson cook [69] Modified Johnson cook by Sartkulvanich et al. [75] material models at 10000 s^{-1} & 0.7 mm/mm .

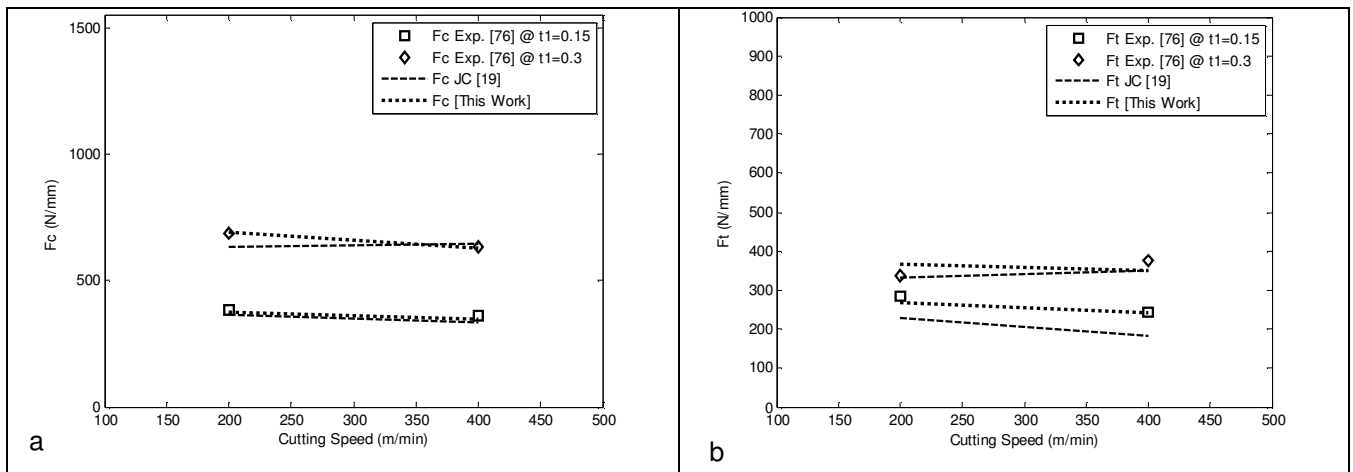
G. Za-extended Oxley's for dual (bcc and fcc) phase materials: aisi1045 steel (task 4)

Aiming to reflect the ductility loss behavior in addition to crystal structure variation of Steel at elevated temperature in this manuscript developed is an extension of the Oxley thick shear zone approach to account for both BCC and FCC Zerilli-Armstrong models. Zerilli-Armstrong form constitutive model with an application for AISI 1045 steel where the choice of the shear zone extension/material model is defined by operating temperature.

Orthogonal cutting tests for AISI 1045 steel reported by Oxley [30] and Ivester et al. [76] using sharp tools are utilized to validate the performance of the Oxley-Zerilli-Armstrong

extended methodology. Considering the improved dynamic stress predictability using dual Zerilli-Armstrong material reported in Figure 5.9a and 5.9b, we adopt the dual material model approach to the thick shear zone Zerilli-Armstrong extension methodology. As described in Figure 5.2, based on operating shear and tool-chip interface temperature, the suitable BCC/FCC material model is utilized and paired with the conceived thick Shear zone BCC/FCC Zerilli-Armstrong extension methodology. Based on the iron-carbon phase diagram presented by Long and Leighty [65], for operating temperature lower than 723oC matching full ferrite (BCC crystal structure) solid solution, the Oxley-Zerilli-Armstrong BCC extension developed methodology is utilized. At temperatures higher than 795oC matching with full austenite (FCC crystal structure) solution Oxley-Zerilli-Armstrong FCC extension developed methodology adopted.

For temperature ranging from 723oC and 795oC, Oxley-Zerilli-Armstrong BCC and FCC methodologies are adopted with flow stress values as reported in task 4 and equivalent strain hardening index, n_{eq} , conceived from the function of BCC ($n_{eq(BCC)}$) and FCC ($n_{eq(FCC)}$). Operating strain hardening indices calculation is based on the BCC/FCC phase diagram inverse lever rule define as weight percentage mixture of BCC and FCC solid-phase solution function of temperature.



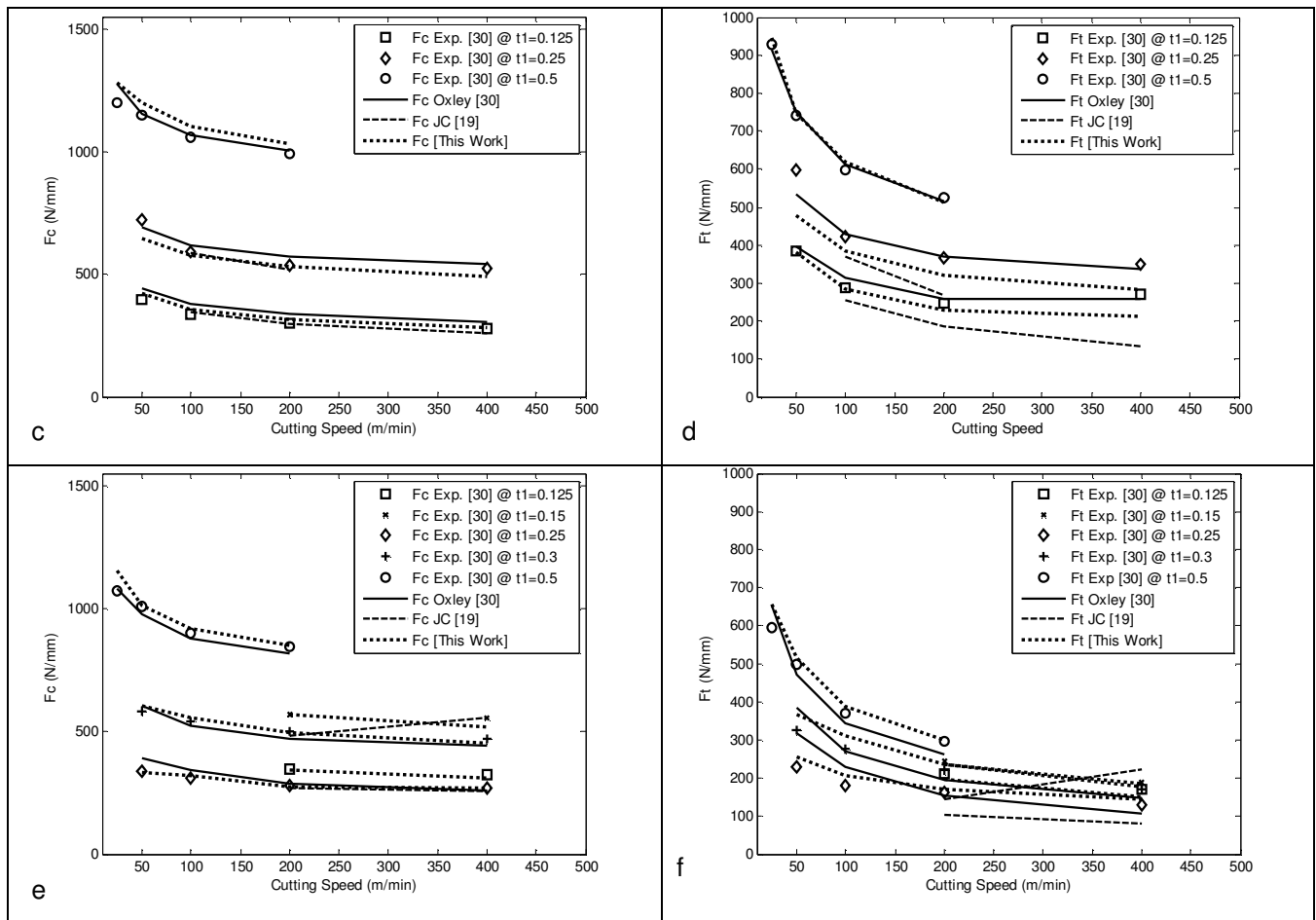


Figure 5.10. Cutting force components for AISI 1045 steel: Oxley experimental data Oxley [30], Ivester experimental data [76], Oxley numerical results Oxley [30], Oxley extended to JC results [19], and Oxley-ZA extended methodology results [this work]: a, c, e) Cutting force for rake angle = -7° , -5° , and 5° respectively; b, d, f) Thrust force for rake angle = -7° , -5° , and 5° respectively.

Cutting parameters consisting of cutting speed, cutting feed rate, and tool rake angles reported by Oxley [30] and Ivester et al. [76] utilized as input to the developed Oxley-Zerilli-Armstrong extended dual-material model methodology.

Figure 5.10 compares AISI 1045 experimentally found cutting and thrust forces from Oxley [30] and Ivester et al. [76] versus Oxley methodology reported results in Oxley [30], Johnson Cook thick shear zone approach extension published results in Ivester et al. [76] versus this work's ZA extended dual-material model methodology predicted forces.

Table 5.2 AISI 1045 Orthogonal tests summary

Test #	Rake angle (°)	Cutting Speed (m/min)	Feed (mm)	Exp. (N/mm), [30], [19]		Oxley (N/mm),		Diff. %, Oxley, [30]		Oxley-JC (N/mm),		Diff. %, Oxley -JC (N/mm),		Oxley (N/mm)		Diff. %, Oxley (N/mm)	
				F _c	F _t	F _c	F _t	F _c	F _t	F _c	F _t	F _c	F _t	F _c	F _t	F _c	F _t
1	-7	200	0.15	383.4	286	-	-	-	-	366	229	4.50	19.90	374.	267	2.26	6.68
2	-7	400	0.15	358.2	242	-	-	-	-	334	183	6.70	24.50	345.	240	3.51	1.00
3	-7	200	0.3	687.1	337	-	-	-	-	632	333	7.90	1.40	689.	367	0.36	8.67
4	-7	400	0.3	630.3	375	-	-	-	-	647	350	2.70	6.70	628.	349	0.35	6.82
5	-5	50	0.125	396.2	383	439	395	11.00	3.20	-	-	-	-	422.	380	6.69	0.63
6	-5	100	0.125	337.8	287	376	314	11.50	9.50	347	257	2.70	10.50	356.	285	5.57	0.61
7	-5	200	0.125	302.1	247	339	258	12.30	4.50	297	185	1.70	25.10	316.	228	4.63	7.72
8	-5	400	0.125	279.3	269	305	257	9.20	4.40	260	133	6.90	50.70	284.	210	1.93	21.83
9	-5	50	0.25	720.8	598	691	532	4.10	11.00	-	-	-	-	644.	478	10.53	19.98
10	-5	100	0.25	589.4	422	620	427	5.20	1.10	589	369	0.10	12.70	577.	384	2.02	9.02
11	-5	200	0.25	537.4	366	574	370	6.90	1.00	519	268	3.40	26.90	530.	318	1.28	13.09
12	-5	400	0.25	522.8	350	540	337	3.40	3.60	-	-	-	-	491.	281	5.93	19.76
13	-5	25	0.5	1200.5	929	127	915	6.20	1.50	-	-	-	-	1278	945	6.49	1.71
14	-5	50	0.5	1151	741	115	749	0.30	1.00	-	-	-	-	1196	747	3.97	0.79
15	-5	100	0.5	1060	598	106	612	0.60	2.40	102	535	3.10	10.60	1103	618	4.07	3.42
16	-5	200	0.5	992	525	100	515	1.30	1.90	-	-	-	-	1030	512	3.90	2.50
17	5	200	0.15	345.3	212	-	-	-	-	271	104	21.30	50.90	341.	198	1.07	6.52
18	5	400	0.15	324.6	171	-	-	-	-	256	79.	21.00	53.90	309.	151	4.81	11.84
19	5	200	0.3	567.6	245	-	-	-	-	484	145	14.60	27.30	567.	220	0.02	10.26
20	5	400	0.3	555.8	190	-	-	-	-	553	225	0.50	18.30	520.	185	6.44	2.73
21	5	50	0.125	336.1	228	393	317	17.00	39.20	-	-	-	-	333.	256	0.92	12.35
22	5	100	0.125	311.5	179	344	228	10.50	27.30	-	-	-	-	321.	205	3.23	14.41
23	5	200	0.125	278.7	163	286	154	2.90	5.00	-	-	-	-	273.	171	1.93	5.44
24	5	400	0.125	270.5	130	262	106	3.00	18.70	-	-	-	-	271.	144	0.41	10.45
25	5	50	0.25	582	326	606	383	4.20	17.50	-	-	-	-	605.	366	4.00	12.36
26	5	100	0.25	541	277	524	269	3.00	3.00	-	-	-	-	553.	312	2.26	12.59
27	5	200	0.25	500	220	467	195	6.60	11.10	-	-	-	-	497.	236	0.54	7.28
28	5	400	0.25	467.2	171	442	146	5.30	14.30	-	-	-	-	451.	175	3.30	2.58
29	5	25	0.5	1074	594	108	652	0.80	9.70	-	-	-	-	1154	657	7.50	10.70
30	5	50	0.5	1008	497	975	472	3.30	4.90	-	-	-	-	1013	515	0.52	3.68
31	5	100	0.5	901.6	369	877	342	2.70	7.30	-	-	-	-	915.	386	1.57	4.52
32	5	200	0.5	844.3	297	819	260	2.90	12.30	-	-	-	-	851.	299	0.86	0.84
R2 F_c, F_t Methodology versus F_c, F_t Exp.						0.99	0.96	-	-	0.97	0.75	-	-	0.99	0.96	-	-
Average % Difference F_c, F_t Methodology versus F_c, F_t Exp.						-	-	5.60%	9.00%	-	-	6.90%	24.2%	-	-	3.21%	7.90%

Table 5.2 summarizes Oxley [30] and Ivester et al. [76] experimental results compared to Oxley [30] methodology, Oxley- JC extension Lalwani et al. [19] methodology and conceived methodology. A mean difference of 3.21% achieved for F_c and 7.9% for F_t by comparing the methodology cutting F_c and thrust forces F_t versus experimentally collected data by Oxley [30] and Ivester et al. [76]. The presented methodology has a predictability performance similar to achieved by Oxley [30] methodology and enhanced predictability compared to the obtained by Lalwani et al. [19] Oxley-JC extended methodology.

For AISI 1045 and for rake angle = (left) -5° and (right) 5° , Figure 5.11 compares the experimentally-measured chip thickness Oxley [30] at cutting conditions reported in Table 5.2 against the presented methodology for chip thickness values predicted using the ZA extended dual-material methodology. Predicted chip thickness values compare well against experimentally-measured values with an average difference of 5.9 %.

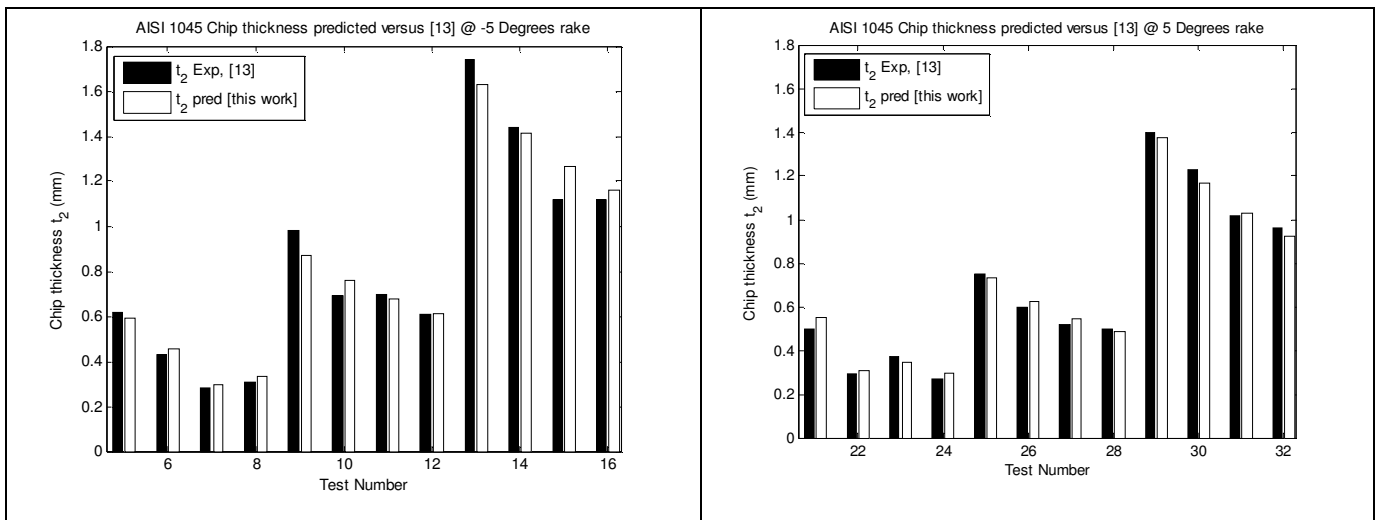


Figure 5.11. Chip thickness for AISI 1045 steel: Oxley experimental data Oxley [13] versus and Oxley-ZA extended methodology predicted results for rake angle = (left) -5° and (right) 5° .

H. Conclusions

This work extends Oxley's original thick shear zone formulations by incorporating Zerilli-Armstrong BCC and FCC material models. This extension is made possible by reformulating the thick shear zone strain hardening index, n_{eq} , specifically for either BCC or FCC Zerilli-Armstrong material models separately through derivation, making possible the application of Oxley shear zone approach to a wide range of materials and operating conditions. The adopted dual-material model approach also accounts for steel blue brittleness effect in addition to the BCC-FCC phase change.

The work results are verified using 6061-T6 Aluminum and AISI 1045 steel, an FCC, and dual-phase BCC/FCC materials. First, this work's estimates of flow stress values over a wide range of state variables of strain, strain rate, and temperature are compared against numerical predictions, including other works based on Johnson-Cook constitutive law and against experimental reports of cutting forces and chip thickness values. Then, verifications are performed on these two materials under simulated orthogonal cutting conditions. This work's force estimates are found to compare favorably with cutting and thrust force values from published experimental values and against simulated force values based on other methods.

CHAPTER VI

INCORPORATING CUTTING TEMPERATURE DISTRIBUTION INTO OXLEY'S MACHINING SHEAR ZONE THEORY

Presented a methodology considered a valuable tool for machinists allowing the simulation of complex machining processes that may be used to identify optimal cutting conditions that minimize energy consumption and increase tool life.

Part of the analysis investigated temperatures occurring during the drilling process, where a series of drilling experiments performed using an inverted setup. Adopted pre-cored Aluminum 6061-T6 workpieces drilled using straight Guhring RT150 drills with coolant through holes. Thermocouples are channeled through the coolant holes and fixed on the drill flank face allowing temperature measurements during the drilling process. Experimentally collected forces and temperature measurements at varied drilling conditions are used for work validation.

Conceived the modification of the Oxley Zerilli Armstrong by implementing the moving heat source method temperature analytical solution accounting for primary and secondary deformation zones heat generation adapted to account for the effect of plastic deformation heat generation occurring at the tool chip interface zone. The discretization of the shear and the tool chip interface planes is applied, and tool chip heat partition ratios are found for each element by applying the thermal continuity principle.

For the sake of validation, this work methodology forces and temperature results are compared against literature reported force and temperature measurements generated based on orthogonal cutting tests performed on AISI 1040 steel.

Using the thermally extended Zerilli Armstrong Oxley thick shear zone approach and considering drilling as application, the cutting simulation torque, thrust force, and flank surface temperatures are validated by comparing against experimentally collected torque, thrust, and temperatures at varied drilling conditions. Simulation results predicted experimentally collected results achieving a mean Error of 8.2%, 14.2%, and 7.5% for Drilling torque, thrust, and temperatures, respectively.

A. Introduction

Cutting temperature has a major effect on operating forces, process energy consumption, and machining tool life. Having a model that couples material model with operating cutting parameters to find resulting machining forces and temperatures is considered an advancement that permits the machinist to design tool geometry and select cutting parameters of cutting inclination angles, rake angles, uncut chip thickness and cutting speed that results in minimizing machining energy consumption. To analyze the response of Aluminum material under drilling conditions, a series of drilling tests using inverted set up are implemented inline with inverted drilling set up presented by Hamade et al. [77]. The drilling experiments allow the measurements of torque, thrust, and temperature at varying drilling conditions applied to pre-cored Aluminum 6061-T6 workpieces.

Temperature modeling has long been investigated in machining with the aim of characterizing temperature rise occurring at the shear zone and at the tool chip interface zone.

The thick shear zone approach presented by Oxley[78] utilized Boothroyd [31] empirical temperatures modeling for estimating shear tool chip interface zone stresses.

Considering that operating temperature is a major parameter affecting the machining process, developing a predictive temperature model is an aim highly investigated. In his work Boothroyd [31] presented an empirical temperature model predicting shear and tool chip interface. Others, like Jasper[79], adopted an iterative finite difference approach for temperature modeling. Finite Element analysis was also investigated by Tay[80] for machining temperature modeling. The analytical approach subject of this investigation was first adopted by Hahn [81] and Trigger [82]for machining thermal modeling. In his work Komanduri [83] developed Han's empirical model by adopting a variable tool chip heat partition model. Chenwen [84] coupled discretization of the tool chip interface and utilized it to depict the variation of the tool chip heat partition ratio along the tool chip line. All models presented by Hahn [81], Trigger [82], Komanduri [85], and Chenwen [84] adopted the tool chip friction force as the cause of heat generated at the tool chip interface area. Also, Chenwen [84] found the tool chip interface heat partition ratio by applying equality of temperature at tool and chip for each discretized interface element at matching geometric location.

Even though finite element analysis accounts for tool chip interface plastic deformation heat generation effect, machining models following the two dimensional heat transfer equation solution presented by Komanduri [85] and Chenwei [84] accounts only for the secondary deformation zone heat generation caused by the tool chip friction forces. In this work the chip thermal boundary conditions following Komanduri [85] are modified to account also for the heat generation caused by plastic deformation occurring within secondary deformation zone adjacent to the tool chip interface plane. Benefiting from the large improvement in computer technology, proposed the modification of the Oxley thick shear zone approach to account for the

extended analytical temperature solution by utilizing the found shear zone and interface zone temperatures as a substitute to the long-used Boothroyd [31] empirical temperature models.

The conceived improved thermal machining model is used to estimate the shear and tool chip interface temperatures modeling by averaging temperatures within the shear and the tool chip interface secondary deformation zones, respectively. The temperature averaging is performed through zone integration, estimating the mean shear and tool chip interface temperatures and is used part of the thick shear zone approach as a substitute to the empirical temperature model, as presented by Karpat and Ozel [86].

Thus presented a methodology that is an advancement to Zerilli Armstrong extended Oxley thick shear zone approach reported by Seif et al. [52] by substituting Boothroyd [31] empirical approach with this work analytical temperature solution for the shear zone and tool chip interface zone temperature models. Part of this work validation, simulation results using the thermally extended Zerilli Armstrong dual BCC\FCC Oxley thick shear zone approach reported are compared against AISI 1040 steel machining force and temperatures measurements reported by Saglam [32] at varying cutting conditions.

The thick shear zone approach based on Oxley [78] methodology was found applicable to modeling complex machining process as presented by Watson[87] also in their work Seif et al. [88] adopted Lalwani et al. [89], thick shear zone approach accounting for Johnson cook material model to estimate cutting lip torque and thrust forces generated along the cutting lip through the use of Lin [40] oblique cutting geometric transformation. For further corroboration, the conceived thermally extended Zerilli Armstrong extended Oxley thick shear zone approach is adopted for drilling process simulation.

The Cutting lip is divided into a series of cutting edge elements, and each element is assigned with a rake, inclination angle, cutting speed, and uncut chip thickness cutting conditions, and flank surface temperature is estimated following Agupiu et al. [90] temperature simulation arrangement inline with Armarego[91] Cutting lip model..

The thermally extended thick shear zone approach accounting for FCC Zerilli Armstrong is applied to each cutting-edge element. This work temperature and force methodology reported improved performance in predicting experimentally collected torque, thrust forces, and flank face temperatures, using as input the Aluminum 6061-T6 FCC Zerilli Armstrong material model and drilling cutting conditions of speed and feed rates.

B. Methodology

The methodology adopted in realizing this research is divided into five tasks defined as:

Task 1 implements the inverted drilling set up, allowing the measurement of torque, thrust, and temperature occurring during the drilling process at varying cutting conditions.

Task 2 revises the Oxley Zerilli Armstrong extended methodology reported by Seif et al. [52] thermal modeling to allow interface with moving heat source closed-form temperature modeling of the cutting process.

Task 3, extends the Komanduri [85] closed form machining thermal model to allow for updated heat partition ratio at the tool chip interface zone accounting for heat generation due to shear zone plastic deformation, tool chip zone friction effect and the advanced tool chip plastic deformation effect occurring at the secondary deformation zone.

Task 4, Validates the Oxley Dual BCC/FCC methodology reported by Seif et al. [52] coupled with the extended closed-form temperature model by comparing against cutting, thrust, and tool chip interface temperature results reported in the literature for AIS1040 Steel material

Task 5, Validates the thermally extended Oxley Dual FCC methodology coupled with the drill lip cutting model reported by Seif et al. [88] for drilling torque thrust and temperature simulation by comparing against experimentally collected torque, thrust and temperature data.

C. Experimental

For the sake of analyzing temperatures occurring at the drill bit flank face, adopted an inverted set up as presented by Hamade et al. [77]. To limit the experimental investigation to the cutting action occurring at the drill bit cutting lip region, the Aluminum 6061-T6 workpiece is pre-cored with a small drill having a diameter slightly larger than the drill bit chisel edge diameter, as presented in Figure 6.1a. Straight flute drill of type Guhring RT150 with 10mm diameter is adopted, thermocouples are passed through the coolant holes and welded at the lip flank face, as presented in Figures 6.1b and 6.1c. Also presented in Figure 6.1d, a sample drilled workpiece.

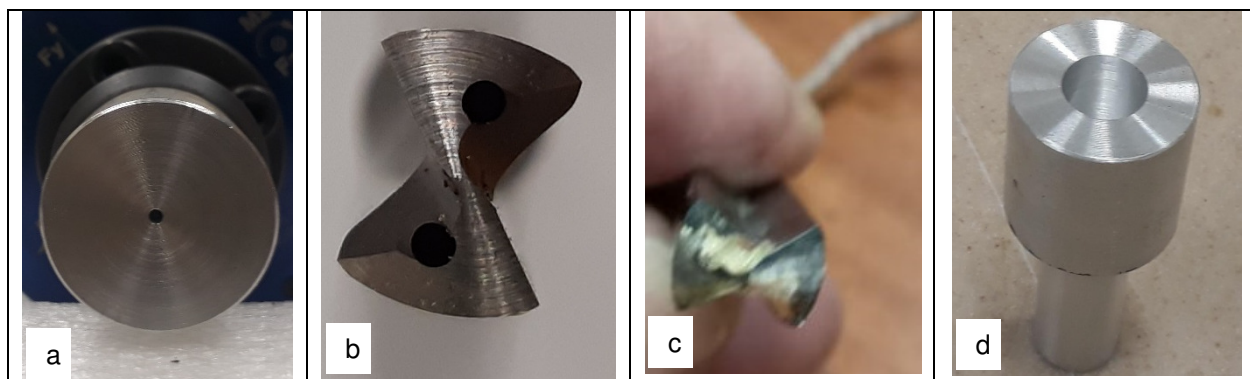


Figure 6.1. Photograph reporting a) Pre-cored Workpiece b) Drilled workpiece c) Guhring RT150 straight flute drill d) Thermocouples brazed on the drill flank face

Two thermocouples type K were fitted inside the Guhring RT150 drill coolant channels; the thermocouple tip is welded at the lip flank face using silver joining material having a melting temperature 795 degrees higher than the melting temperature of the Aluminum being cut. Thermocouple electric signal is processed by national instruments NI-9213 C series temperature input module and transmitted through data acquisition board for collection.



Figure 6.2 Photograph reporting a) Drill with brazed thermocouples fixed in inverted positions b) Inverted Drilling Set up c) Drilling experiment following inverted setup d) Machine Center.

Calibration of the temperature measurement sensors is made against boiling water to guarantee the accuracy of the measurements. Inverted set up as presented in Figure 6.2a, is adopted where the straight flute Guhring, RT150, 10 mm diameter drill is fixed to the CNC working space in an inverted position, and the workpiece is fixed to the 4-channel rotary dynamometer (Kistler type model 9123) as presented in Figure 6.2b. Torque and thrust measurements are processed through a multichannel charge amplifier (Kistler type model 5223) and transmitted for processing using the Dynoware software. Calibration of thrust and torque measurements is made against fixed weights and fixed torques to guarantee the accuracy of the measurements. The fixed drill is aligned with the center of rotation of the spindle head, thus minimizing additional forces and vibrations caused by misalignments. For conducting the drilling experiments, Machine center HAAS VF-6 type CNC powered by a 20 hp Motor presented in Figure 6.2d available at the AUB is adopted.

Presented in Figure 6.2c, the inverted set up under in operation. In order to minimize the effect of plowing forces on the measured temperatures and forces, fresh tools are adopted with each experiment. Reported in Table 6.1 are the Guhring RT150 Straight flute drill geometric characteristics as per manufacturer datasheet.

Table 6.1: Guhring RT150 Straight Flute Drills Geometric Characteristics

	SI units
Diameter, D (mm)	10
Web thickness (mm)	1.8
Point angle 2κ (degrees)	119
Helix angel β_0 (degrees)	0
Chisel angle ψ (degrees)	135

Reported in Table 6.2 is the summary of the drilling experiments conducted covering a wide range of cutting speed and feed rate performed using the straight flute Guhring RT150 drill characterized by a tool cutting edge radius is 5 μm .

Table 6.2 Drilling test matrix

Exp #	Feed (mm/rev)	CER to uncut chip thickness ratio	Max Cutting Speed (m/min)	Rpm	Max depth of cut (mm)	Cutting length (mm)	Time of experiment (s)
1	0.16	6.25%	35	1114	15	471.238898	5.049371634
2	0.32	3.13%	35	1114	15	471.238898	2.524685817
3	0.64	1.56%	35	1114	15	471.238898	1.262342908
4	0.16	6.25%	70	2228	15	471.238898	2.524685817
5	0.32	3.13%	70	2228	15	471.238898	1.262342908
6	0.16	6.25%	140	4456	15	471.238898	1.262342908
7	0.32	3.13%	140	4456	15	471.238898	0.631171454
8	0.16	6.25%	280	8913	15	471.238898	0.63110064
9	0.32	3.13%	280	8913	15	471.238898	0.31555032

To improve the reliability of the measurements, experiments are repeated twice at each of the considered conditions reported in Table 6.2. Fixed drilling depth is adopted per experiment where the maximum drilling feed reached is 1.5D inline with the maximum 4D drilling depth recommended by the manufacturer.

Reported in Figure 6.3a are the temperature profiles for the average measured temperature collected from TC1 and TC2 thermocouples for the different machining conditions reported in Table 6.2. Also reported in Figure 6.3b are sample torque and thrust data collected at a feed rate of 0.16mm/rev and a rotational spindle speed of 1114 rpm. Torque, thrust, and temperatures are collected using a sampling rate of 3000 Hz.

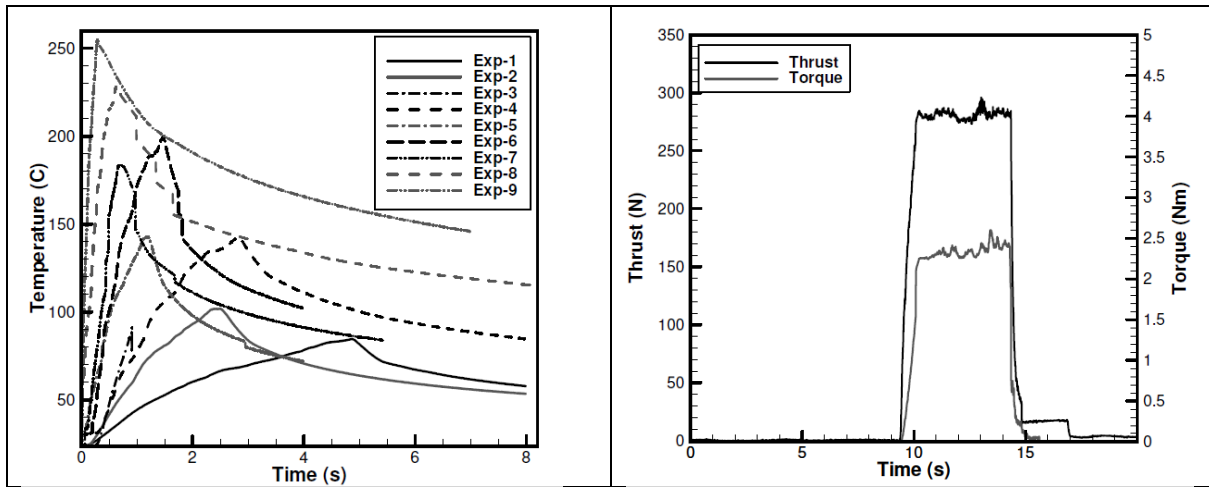


Figure 6.3 Experimentally measured a) Sample temperature data b) Sample torque and thrust data

D. Thermal extension of Oxley thick shear zone approach adapted Zerilli-Armstrong

The machining process is the act of removing unwanted material under the action of high plastic deformation. Machining processes are classified as simple turning operation modeled as orthogonal cutting, or complex machining process such as drilling. The orthogonal cutting considered as the basis for modeling the different machining processes and is the simplest machining action where the material is removed under the linear motion of cutting tool at a fixed operational rake angle and clearance angles.

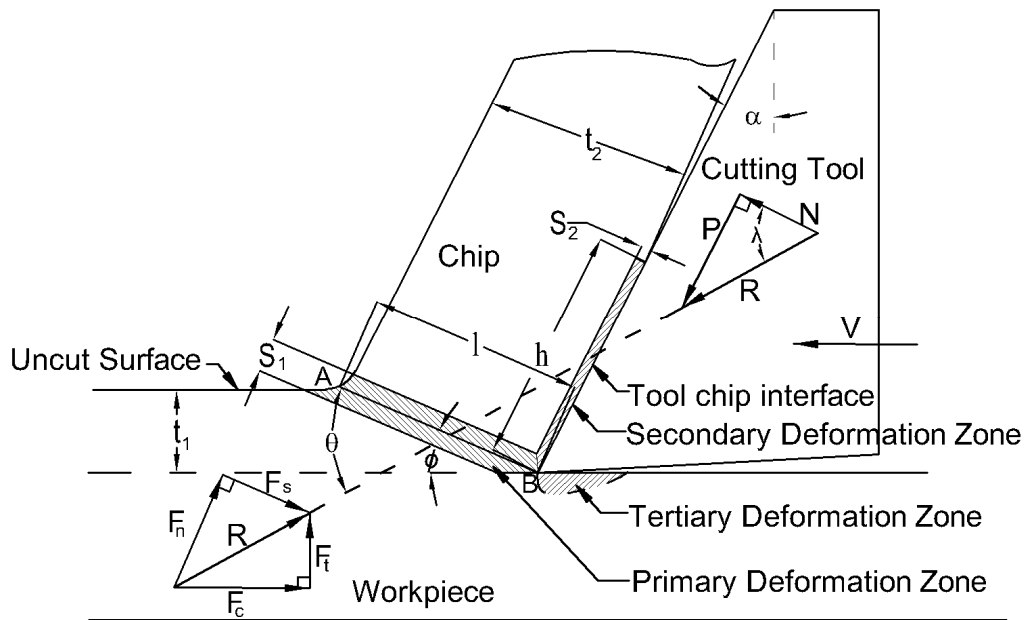


Figure 6.4. Shear zone's orthogonal cutting parameters and force components.

As Presented in Figure 6.4, the orthogonal machining process involves three main

deformation zones defined as:

- Primary deformation zone at the shear deformation zone.
- Secondary deformation zone at the chip tool interface zone.
- Tertiary deformation zone at the newly formed workpiece surface.

In his work Oxley[78] proposed a methodology based on thick shear zone approach that predicts shear angle, tool chip friction angle and machining forces based on Oxley [78] material flow stress model and cutting parameters at a shear angle and primary secondary deformation zone thickness parameters that guarantee the balance of forces between shear plane forces and tool chip interface forces.

A thermal model predicting the response of material accurately is consisted an important parameter to improve the accuracy of Oxley [78] thick shear zone approach for predicting machining forces along with operating shear and tool chip interface temperatures. In

his work Oxley [78] relied on Boothroyd [31] analytical equations predicting average machining temperatures along the primary shear zone, T_{AB} , and secondary (tool chip interface) zone, T_{int} , reported in Eqs 6.1 and 6.2 respectively.

$$T_{AB} = T_w + \eta \frac{(1-\beta_T)F_s \cos\alpha}{\rho_d C_p t_1 w \cos(\phi-\alpha)} \quad (6.1)$$

$$T_{int} = T_w + \frac{(1-\beta_T)F_s \cos\alpha}{\rho_d C_p t_1 w \cos(\phi-\alpha)} + \psi \Delta T_m \quad (6.2)$$

Presented in this work, the thermal extension of the Oxley's parallel-sided thick zone analysis incorporating the Zerilli-Armstrong material models. Adopted in this work, the use of an analytical closed-form solution for the temperature estimation at the shear zone and tool chip interface region inline with machining thermal modeling reported by Komanduri [83]. Shear angle, primary deformation zone thickness ratio ($C'=l/S1$), secondary deformation zone thickness ratio ($\delta=S2/t2$), material flow stress parameters varied in the thick shear zone analyses, are used as input parameters to the analytical form machining thermal model.

E. Analytical approach simulating shear and tool chip interface temperature

Thermal modeling of machining processes has long been a challenge for researchers. Hahn [81] and Chao [92] were among the pioneers who investigate analytical solutions for machining thermal modeling. All models reported heat sources located at the shear plane and the tool chip interface with moving characteristics. All researchers focused on primary deformation zone heat source and secondary deformation zone heat source and discarded the tertiary deformation zone heat sources. In their work Komanduri [83],[85], and [93] revisited Hahn [81] thermal model where a solution for the moving oblique heat source model at a shear angle ϕ is adopted to model the effect of heat generation caused by shear plastic deformation and adopted

the infinitely long moving line heat source approach. Heat generation at the shear zone affects the workpiece, and the formed chip temperature rise. The tool chip interface heat generation is an added factor contributing to the formed chip temperature rise as well as well as is affecting the cutting tool temperature distribution. Adopted by Komanduri [83],[85] and [93] modeling assumptions defined as:

1-Steady state condition with constant temperature fields.

2-Primary zone deformation and tool chip friction forces are converted to heat absorbed by the tool, chip, and workpiece, matching adiabatic surface assumption reported by Chao [92].

3- Cutting edge of the tool is perfectly sharp, and no tool wear is considered, and the influence of parasitic forces as a heat source on the tool flank face is considered to be negligible.

4-The cutting tool is assumed to be a semi-infinite medium relative to the chip inline with Wiener [94]reported works.

Figure 6.5 defines a graphical representation of the boundary conditions assumptions adopted by Komanduri [83], and implemented in the presented research to reach the shear and tool chip interface temperature analytical solution.

Presented by Jaspers [79], the two-dimensional heat transfer equation for a medium moving in the x-direction relative to a stationary heat source derived from the basic conduction equation reported in Eq. 6.3:

$$\frac{\delta}{\delta x} \left(k \frac{\delta T}{\delta x} \right) + \frac{\delta}{\delta y} \left(k \frac{\delta T}{\delta y} \right) - \rho c V_c \left(\frac{\delta T}{\delta x} \right) + q = \rho c \frac{\delta T}{\delta t} \quad (6.3)$$

In his work Chenwei [84], based on Komanduri [83] work divided the orthogonal cutting temperature modeling into three interconnected heat transfer models consisting of

1-Workpiece temperature model

2-Chip temperature model

3-Tool temperature model

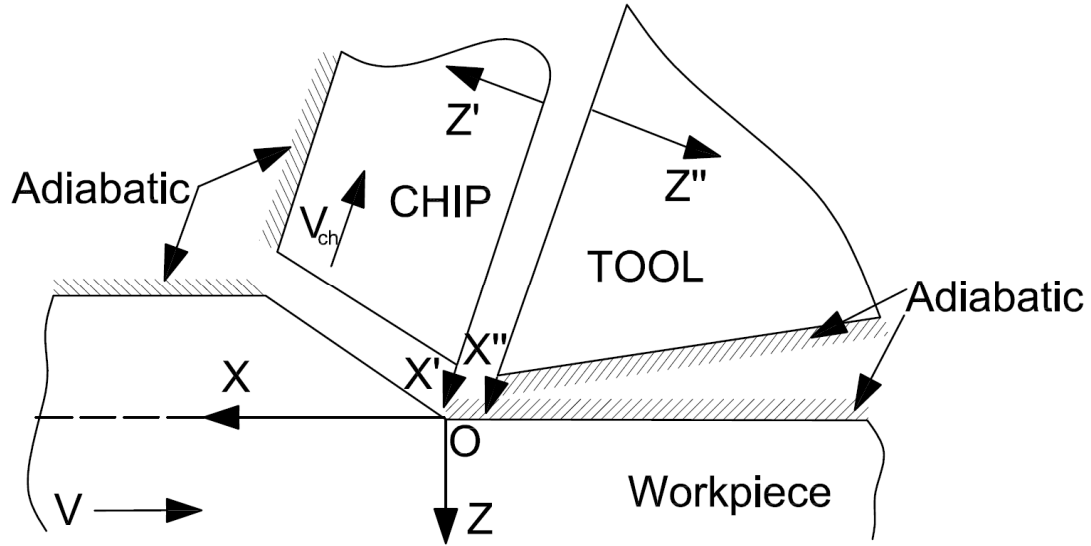


Figure 6.5. Workpiece boundary conditions

Each of the models has its specific moving two-dimensional heat transfer conduction equation reported in Eq. 6.3 along with its boundary conditions, as shown in Figure 6.5.

1. Workpiece side temperature modeling

Based on Komanduri [83] work, the workpiece boundary conditions are reported in Figure 6.5 utilized as a simplification for the two-dimensional conduction heat problem with moving material.

Considering the moving heat source model, heat intensity at the shear plane adopted as uniform flux reported by Trigger [82] and Chao[92] heat generated at the shear plane shown in

Eq. 6.4

$$q_s = \frac{F_s V_s}{w L_{AB}} \quad (6.4)$$

The heat intensity is assumed to be split equally between the workpiece and chip inline with Komanduri [83], compared to Boothroyd [31] where the adopted chip shear heat partition ratio of 0.7.

Considering the workpiece boundary conditions presented in Figure 6.5, the workpiece heat losses to the environment are neglected by assuming adiabatic conditions at workpiece uncut and newly formed surfaces. The heat intensity $(1-\eta)q_s$ is absorbed by the workpiece as presented by Chenwei [84] to obtain the workpiece temperature rise distribution $T_{work-shear}$ influenced by the workpiece shear plane heat source. Equation 6.5 reports the solution for the heat conduction equation estimating the temperature distribution rise $T_{work-shear}$ at an arbitrary point M (x, z) within the machined workpiece.

$$T_{work-shear} = \frac{q_s}{2\pi\lambda_w} \int_0^{L_{AB}} e^{-(x-l_i \sin(\phi))V/2a_w} \left\{ K_0 \left(\frac{VR_1}{2a_w} \right) + K_0 \left(\frac{VR_2}{2a_w} \right) \right\} dl_i \quad (6.5)$$

Where λ_w is the workpiece thermal conductivity, a_w is the workpiece thermal diffusivity, V is the cutting speed, L_{AB} is the shear plane length, ϕ the shear angle, t_1 the uncut chip thickness and $K_0(x)$ is the modified Bessel function of the second kind of order zero

$$R_1 = \sqrt{(x - l_i \cos(\phi))^2 + (z + l_i \sin(\phi))^2} \quad (6.6)$$

$$R_2 = \sqrt{(x - l_i \cos(\phi))^2 + (z + 2t_1 - l_i \sin(\phi))^2} \quad (6.7)$$

The closed-form workpiece temperature rise reported in Eq. 6.5 follows the X-Z coordinate system orientation presented in Figure 6.5.

2. Chip side temperature modeling

The same two-dimensional conduction equation as reported in Eq. 6.3 is adopted for modeling the chip temperature distribution. The solution of the chip temperature rise accounting for the shear zone heat generation and the tool chip interface heat generation following the

overlaying of heat source principle is adopted. The formed chip temperature distribution considered takes into account the boundary conditions presented by Komanduri [83] inline with Trigger [82] model where

1-Constant heat intensity is adopted at the shear plane with a value of ηq_s

2- Variable heat intensity is adopted at the tool chip interface with a value of $B(l_i)q_{int}(l_i)$ where $B(l_i)$ and $q_{int}(l_i)$ are the tool chip heat partition ratio and the heat generation at the tool chip interface both functions of the element location along the tool chip contact length l_i .

3-Adiabatic condition at the formed chip outer surface is adopted, and heat losses to the surrounding environment are neglected. The considered adiabatic condition accounts for high chip moving speed involved in the cutting process.

Temperature distribution occurring within the formed chip reported in Eq. 6.8 is caused by the shear zone heat generation defined as $T_{chip-shear}(x', z')$ overlaid with the chip temperature distribution caused by the tool chip interface heat generation defined as $T_{chip-secondary}(x', z')$.

$$T_{chip}(x', z') = T_{ambient} + T_{chip-shear}(x', z') + T_{chip-secondary}(x', z') \quad (6.8)$$

The temperature distribution estimates at an arbitrary point in the chip caused by shear heat generation are obtained using the closed-form solution presented in Eq. 6.9.

$$T_{chip-shear} = T_{ambient} + T_{chip-shear} \frac{q_s}{2\pi\lambda_{ch}} \int_0^L e^{-(x'-L_c+l_i\sin(\phi-\alpha))V_c/2a_{ch}} \left\{ K_o \left(\frac{V_c R'_1}{2a_{ch}} \right) + K_o \left(\frac{V_c R'_2}{2a_{ch}} \right) \right\} dl_i \quad (6.9)$$

And reported by Komanduri [85], the chip temperature rise due to the tool chip heat generation is presented in Eq. (6.10).

$$T_{chip-Secondary}(x', z') = \frac{1}{\pi\lambda_{ch}} \int_0^{L_c} B(l_i) q_{int}(l_i) e^{-(x'-l_i)V_c/2a_{ch}} \left\{ K_0 \left(\frac{V_c R'_3}{2a_{ch}} \right) + K_0 \left(\frac{V_c R'_4}{2a_{ch}} \right) \right\} dl_i \quad (6.10)$$

The chip temperature rise temperature is a function of machining conditions defined as t_1 the uncut chip thickness, ϕ the rake angle, L_c the tool chip contact length, t_2 the chip thickness, λ_{ch} the chip thermal conductivity, a_{ch} is the chip thermal diffusivity, where the shear plane heat source moves at a chip flow velocity V_c . Also R'_1 and R'_2 are the shear chip temperature distribution modified Bessel function of the second kind of order zero terms as defined in Eqs 6.11 and 6.12.

$$R'_1 = \sqrt{(x' - L_c + l_i \cos(\phi - \alpha))^2 + (z' + l_i \cos(\phi - \alpha))^2} \quad (6.11)$$

$$R'_2 = \sqrt{(x' - L_c + l_i \sin(\phi - \alpha))^2 + (z' + 2t_{ch} - l_i \cos(\phi - \alpha))^2} \quad (6.12)$$

And R'_3 and R'_4 the chip secondary deformation zone temperature distribution modified Bessel function of the second kind of order zero terms as defined in Eqs 6.13 and 6.14.

$$R'_3 = \sqrt{(x' - l_i)^2 + (z')^2} \quad (6.13)$$

$$R'_4 = \sqrt{(x' - l_i)^2 + (2t_2 - z')^2} \quad (6.14)$$

The closed-form chip temperature rise reported in Eq. 6.8 follows the X'-Z' coordinate system with directions defined in Figure 6.5. The chip temperature distribution caused by the secondary deformation zone effect reported in Eq. 10 is a function of $q_{int}(l_i)$ the tool chip heat generation ratio and $B(l_i)$ the tool chip heat partition ratio varying along the tool chip contact length.

As presented by Young et al. [95], tool chip interface heat generation has a dominant effect on the chip temperature distribution compared to the shear zone heat generation. The heat

generated at the interface tool chip is mainly caused by the tool chip rubbing action and defined as friction heat q_f adopted by researchers as a uniform heat flux boundary conditions with a heat liberation mean intensity defined by Komanduri [83] in Eq. 6.15

$$q_f = \frac{PV_c}{wL_c} \quad (6.15)$$

Where P is the cutting tool friction forces, V_c the chip velocity, w is the width of cut, and L_c is the tool chip contact length.

Added to the friction heat generation, this research accounts for the plastic deformation heat flux occurring at the secondary deformation zone defined q_p and controlled by the operating tool normal forces N at the secondary deformation zone. To the authors knowledge, secondary zone plastic heat generation was rarely investigated for machining thermal modeling; nevertheless heat generation due to plastic deformation is commonly reported by researchers occurring at high strain rate operation based on tensile tests as presented by Kapoor [96]. Presented in this work Eq. 6.16 representing the intensity of the heat generation occurring at the tool chip interface caused by plastic deformation caused by the tool face normal forces N .

$$q_p \left(\frac{W}{mm^2} \right) = \frac{\dot{m}c_p\Delta T}{w*L_c} \quad (6.16)$$

The *parameter* \dot{m} is the material mass flow plastically deformed at the secondary plastic deformation zone defined in Eq. 6.17.

$$\dot{m} = \frac{\rho w * \delta t_2 * L_c}{\frac{L_c}{V_c}} = V_c w * \delta t_2 \quad (6.17)$$

Where w the width of cut, δ the secondary deformation zone thickness ratio, ρ the machined material density and t_2 is the chip thickness. The term $\frac{L_c}{V_c}$ reflects the time necessary for chip material located within the secondary deformation zone to achieve full plastic

deformation, and L_c is the tool chip contact length reported in Eq. 6.18 defined by Lalwani [19] function of the shear angle ϕ , friction angle λ , resultant force angle, θ_R , strain hardening index n_{eq} , and primary deformation zone thickness ratio, C_0 .

$$L_c = \frac{t_1 \sin \theta_R}{\cos \lambda \sin \phi} \left(1 + \frac{C_0 n_{eq}}{3 \left(1 + 2 \left(\frac{\pi}{4} - \phi \right) - C_0 n_{eq} \right)} \right) \quad (6.18)$$

Presented by Kajberg et al. [97], the temperature increase due to plastic heat generation is reported to be a function of operating stress and plastic strain, as defined in Eq. 6.19.

$$\Delta T = \frac{\beta}{\rho c_p} \int_0^{\varepsilon_p} \sigma_N \partial \varepsilon_p \quad (6.19)$$

Thus substituting Eqs 6.17 and 6.19 into Eq. 6.16 results in the average plastic heat generation intensity reported in Eq. 6.20 following Kajberg et al. [97] plastic deformation heat generation. To the authors knowledge, the plastic heat generation at the secondary deformation zone was never reported in machining temperature simulation.

$$q_p \left(\frac{W}{mm^2} \right) = \frac{V_c * \delta t_2 \beta \int_0^{\varepsilon_p} \sigma \partial \varepsilon_p}{L_c} = \frac{V_c * \delta t_2 \beta}{L_c} (\sigma_N * \varepsilon_p) \quad (6.20)$$

Adopted the plastic energy conversion to heat ratio β is a variable parameter function of the operating strain rates, as reported by Feng et al.[55], 0.95 value of β is a good approximation for metals at high strain rates similar to encountered in machining.

Based on Eq. 6.20, heat generation rate due to plastic deformation at the tool chip interface is a function of tool chip normal stress σ_N and secondary plastic strain ε_p reported in Eqs 6.21 and 6.22, respectively, as presented by Oxley[78].

$$\sigma_N = \frac{N}{w L_c} \quad (6.21)$$

$$\varepsilon_p = \frac{L_c}{2\sqrt{3}(\delta t_2)} \quad (6.22)$$

Where N is the tool chip normal force, δ the secondary deformation zone thickness ratio, L_c the chip thickness ratio, and w the width of cut.

Thus, as advancement adopted in this research the total heat generation at the tool chip interface following Eq. 6.22

$$q_{tool\ chip}(l_i) = q_{plastic}(l_i) + q_{friction}(l_i) \quad (6.23)$$

However, according to the Huang-Liang [98] model, the heat generated along the tool-chip interface is described as having a non-uniform heat intensity $q_{tool\ chip}(l_i)$, function of the distance along the tool chip contact length l_i and presented in Figure 6.6 The tool chip heat generation follows the stress distribution occurring along the tool chip interface where the heat flux is modeled to be of constant magnitude along the sticking friction region and varying along the sliding friction region. As reported by Huang-Liang [98] in the sliding region, $q_{tool\ chip}(l_i)$ decreases linearly to zero by the end of the tool chip contact length. The sticking region length is defined as a percentage “a” of the tool chip contact length with a dimension defined as “aLc”. The dimension of the sliding region is defined as “(1-a)Lc”.

The ratio of the sticking length to the tool-chip contact length and its value is in the range of $0 < a < 1$, as reported by Huang-Liang [98]. According to the law of conservation of energy, $q_{tool\ chip}(x)$ is expressed in Eqs 6.24 and 6.25 accounting for both tool chip friction and plastic deformation heat generation.

$$q_{tool\ chip}(x) = (q_f + q_p) \frac{2x}{(1-a^2)L_c} \quad for \quad 0 \leq x < (1-a)L_c \quad (6.24)$$

$$q_{tool\ chip}(x) = (q_f + q_p) \frac{2}{(a+1)L_c} \quad for \quad (1-a)L_c \leq x < L_c \quad (6.25)$$

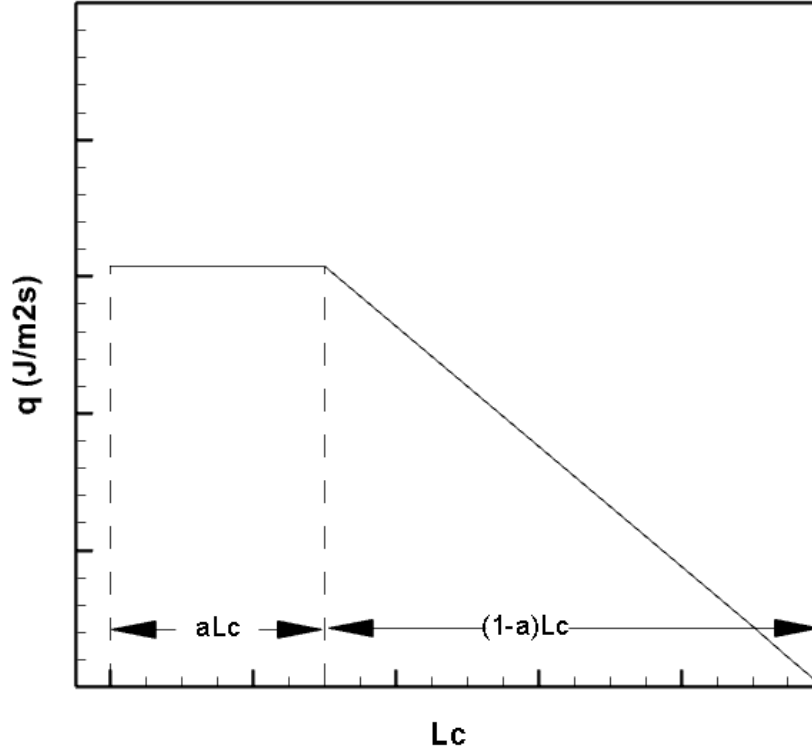


Figure 6.6. Tool chip interface heat generation profile

The sticking length to tool chip contact length ratio, a , is function of operating tool chip interface strain and strain rate to vary between 0.3 and 0.7, as reported by Chenwei [84].

Based on the overlapping principles of heat transfer field, the chip temperature T_{chip} at point $M_0(x_0, z_0)$ in the chip function of both shear heat intensity and tool chip heat intensity can be expressed in Eq. 6.26 as

$$T_{chip}(x', z') = T_{ambient} + \frac{q_s}{2\pi\lambda_{ch}} \int_0^L e^{-(x'-L_c+l_i \sin(\phi-\alpha))V_c/2a_{ch}} \left\{ K_o \left(\frac{V_c R'_1}{2a_{ch}} \right) + K_o \left(\frac{V_c R'_2}{2a_{ch}} \right) \right\} dl_i + \frac{1}{\pi\lambda_{ch}} \int_0^{L_c} B(l_i) q_{int}(l_i) e^{-(x'-l_i)V_c/2a_{ch}} \left\{ K_o \left(\frac{V_c R'_3}{2a_{ch}} \right) + K_o \left(\frac{V_c R'_4}{2a_{ch}} \right) \right\} dl_i \quad (6.26)$$

All terms Eq 6.26 are known except the ratio of the $B(x)$ representing the fraction of heat transferred into the chip, which is a function of the tool chip sticking sliding conditions reported by Komanduri [93].

3. Temperature modeling on the tool side

As shown in Figure 6.5 is a diagrammatical representation of the heat transfer conditions occurring at the tool where it is considered as a static semi-infinite medium with adiabatic surface condition at the clearance edge and heat flux condition of variable magnitude $(1-B(l_i))*q_{int}(l_i)$ function of the tool chip contact length at the chip interface surface.

As presented by Komanduri [85], the tool temperature distribution is defined as T_{tool} for the stationary conditions expressed in Eq. 6.27 as:

$$T_{tool}(x'', y'', z'') = T_{ambient} + \frac{1}{2\pi\lambda_t} \int_0^{L_c} [1 - B(l_i)] q_{int}(x_i) dx_i * \int_{-\frac{w}{2}}^{\frac{w}{2}} \left(\frac{1}{R_1''} + \frac{1}{R_2''} \right) dy_i \quad (6.27)$$

Function of the special terms R_1'' , R_2'' defined in Eq. 6.29 and 6.30, respectively.

$$R_1'' = \sqrt{(x'' - x_i)^2 + (y'' - y_i)^2 + (z'')^2} \quad (6.28)$$

$$R_2'' =$$

$$\sqrt{\{L_c + L_c \cos(2(\alpha + \gamma)) - x'' \cos(2(\alpha + \gamma))\}^2 + (y'' - y_i)^2 + \{z'' - (L_c - x_i) \sin(2(\alpha + \gamma))\}^2} \quad (6.29)$$

Where α is the tool rake angle, γ is the tool clearance angle, w is the width of cut, and the closed-form workpiece temperature rise defined in Eq. 6.27 follows the X''-Z'' coordinate system. All terms defined as geometric and operational parameters are known except the tool chip heat partition ratio of the $B(l_i)$ defining the portion of interface heat absorbed by the chip.

4. Discretization for the tool chip heat partition ratio.

Part of finding an operational specific variable tool chip heat partition ratio, in his work Chenwei [84] divided the tool chip contact length into n elements and assumed that at each

element, the chip side temperature matches the temperature at the corresponding tool chip side. Identical to Chenwei [84] equal tool chip temperature condition is adopted for all elements along the tool chip contact length. By adopting the equal temperature conditions presented in Eq. 30 a system of the equation with n variables defined as the tool chip heat ratio B_n .

$$T_{ambient} + T_{chip-shear}(x', 0) + T_{chip-friction}(x', 0) = T_{ambient} + T_{tool-friction}(x'', 0, 0) \quad (6.30)$$

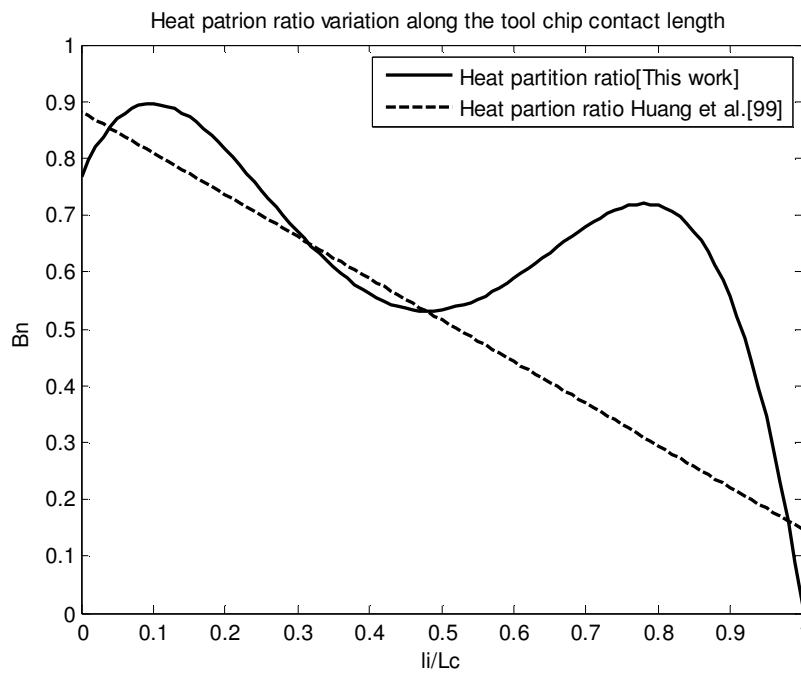


Figure 6.7. Tool chip heat partition ratio

The system of n equation within n unknowns solved numerically using MATLAB®, and the found n heat partition ratios B_n along the chip tool interface satisfies the equal chip and tool temperature conditions at the different positions along the interface line. The solved heat partition ratio varied between 0.9 for elements adjacent to the tool nose to 0 for elements in the vicinity of the chip tool, loss of contact point. Presented in Figure 6.7 sample tool chip heat partition ratio distribution calculated following Eq. 6.30 system of equations for the operational conditions of cutting speed of $V_c=139$,/min, Uncut chip thickness of 0.6mm, cutting Force

$F_c=356\text{N}$, thrust force $F_t=125\text{ N}$, chip thickness ratio for $r=0.1$ and tool chip length of $L_c=0.023\text{ cm}$ for machining AISI 1045 steel.

Part of this work corroboration of the found sample reported heat partition ratio shown in Figure 6.7 matched well with heat partition ratio model Eq. 6.31 conceived by Huan[99] as the heat partition ratio reported by Chenwei [84] for the same machining condition .

$$B = -0.71341 \left(\frac{l_i}{L_c} \right) + 0.8825 \quad (6.31)$$

5. Comparison against temperature contours presented in the literature

Aiming to validate the extended thermal machining model accounting for heat generated by the secondary plastic deformation, presented in Figure 6.8a temperature prediction contour plots compared against Figure 6.8b machining contour plots presented by Komanduri [93].

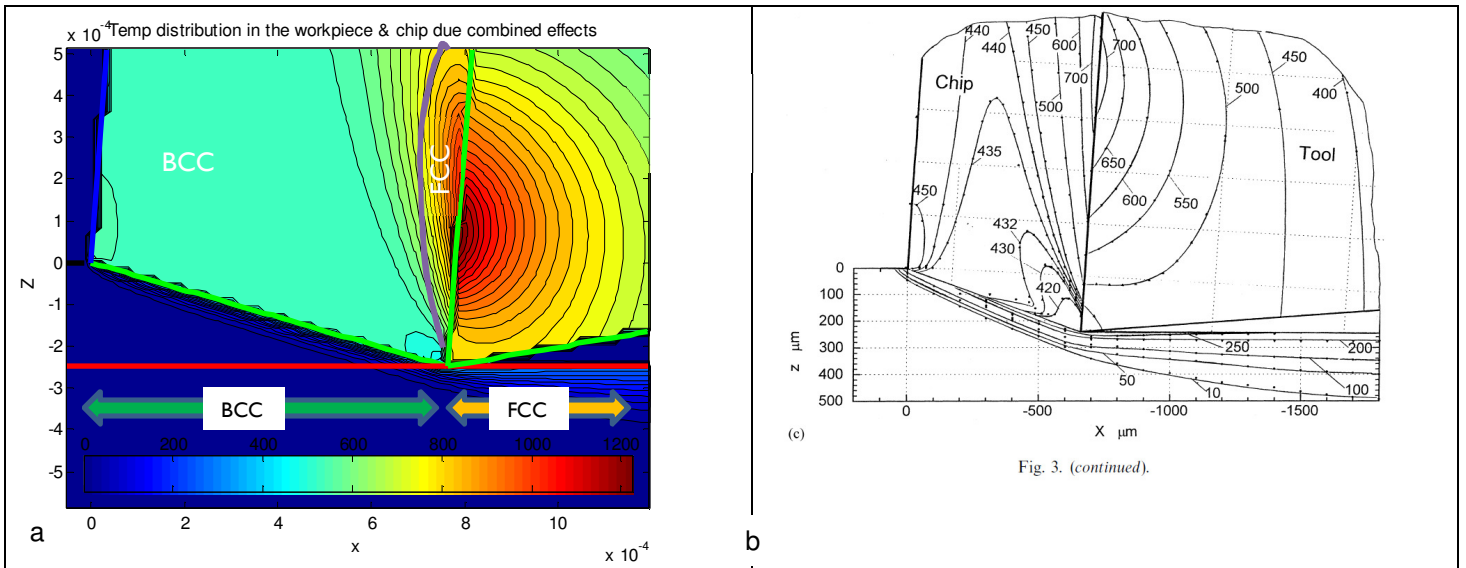


Figure 6.8. Comparison for AISI 1045 steel: a) This work thermal model contours b) Published machining temperature contours Komanduri [93]

Both Figures 6.8a and 6.8b report thermal simulation of steel NE 9444 material at cutting conditions of shear angle equal to 4 degrees, uncut chip thickness $t_1=0.2489\text{mm}$, width of cut $w=2.591\text{mm}$, cutting speed $V_c=152.4\text{cm/s}$, Cutting forces $F_c=1681.3\text{N}$, $F_t=854.0\text{N}$. Chip thickness ratio for $r_c=0.375$ and tool chip contact length $L=1.209\text{mm}$, as reported by Komanduri [93]. The simulated conceived work reports contour plots matched well contour plots presented by Komanduri [93] with an increased tool chip interface temperatures identified in Figure 6.8a driven by the secondary deformation zone plastic heat generation added effect.

F. Oxley Zerilli Armstrong adapted a thick shear zone approach thermal extension.

Proposed in this work, the extension of the shear and interface temperature solution based on the moving heat source method originally conceived by Jaeger [98] for shear and tool chip interface temperatures. The presented work is based on Chenwei [84] improved shear and tool chip interface temperature that extended Komanduri [83],[85], and [93]orthogonal cutting temperature prediction analytical solution. The improved thermal model is used to extend the Zerilli Armstrong adapted thick shear zone approach presented by Seif et al. [52]. The thick shear zone approach thermal extension is performed by interfacing with the extended thermal model to incorporate this work modified Komanduri [83] closed-form temperature model conceived using extended Chenwei [84], closed-form model.

The proposed thermal extension allows the use of close form thermal solution as a substitute to Boothroyd [31] empirical temperature models for predicting operating shear and tool chip interface temperatures. Operating shear angle, primary deformation zone thickness ratio ($C'=l/S_1$), secondary deformation zone thickness ratio ($\delta=S_2/t_2$), material flow stress parameters are utilized as interfacing parameters with the thermal machining model.

Illustrated in Figure 6.9, the thick shear zone approach identified solution shear angle, ϕ , primary deformation zone thickness, S_1 , and secondary deformation zone thickness, S_2 , at conditions that satisfy equilibrium between shear transmitted forces and tool chip interface forces.

Presented in Figure 6.9 is the modification of the Oxley parallel-sided thick shear zone algorithm to account for the shear and tool chip interface temperature models defined in the presented work.

The proposed temperature models are also a function of the shear angle ranging from 5 to 45 degrees, primary deformation zone thickness ratio ($C'=l/S_1$) from 2.0 to 10, and secondary deformation zone thickness ratio ($\delta=S_2/t_2$) from 0.05 to 2.

The thick shear zone approach is extended by calculating the workpiece and chip heat distribution temperature using Eqs 6.5 and 6.26. The Shear zone temperature is evaluated by averaging the temperature within the shear zone through integration. The calculated shear temperature is interfaced with the Oxley Zerilli Armstrong methodology, as shown in Figure 6.9, where the shear zone has a thickness S_1 and length L_{AB} , varied function of the primary deformation zone thickness ratio C and operating shear angle ϕ respectively.

The Adopted shear zone space integration of the $T_{Mshear}(x, z)$ identifies average shear zone temperature, as reported in Eq. 6.31 below.

$$T_{AB} = \frac{1}{S_1} \frac{1}{l_{AB}} \int_{-\frac{S_1}{2}}^{+\frac{S_1}{2}} \int_0^{l_{AB}} T_{Mshear}(x, z) dl_i dS_1 + T_o \quad (6.31)$$

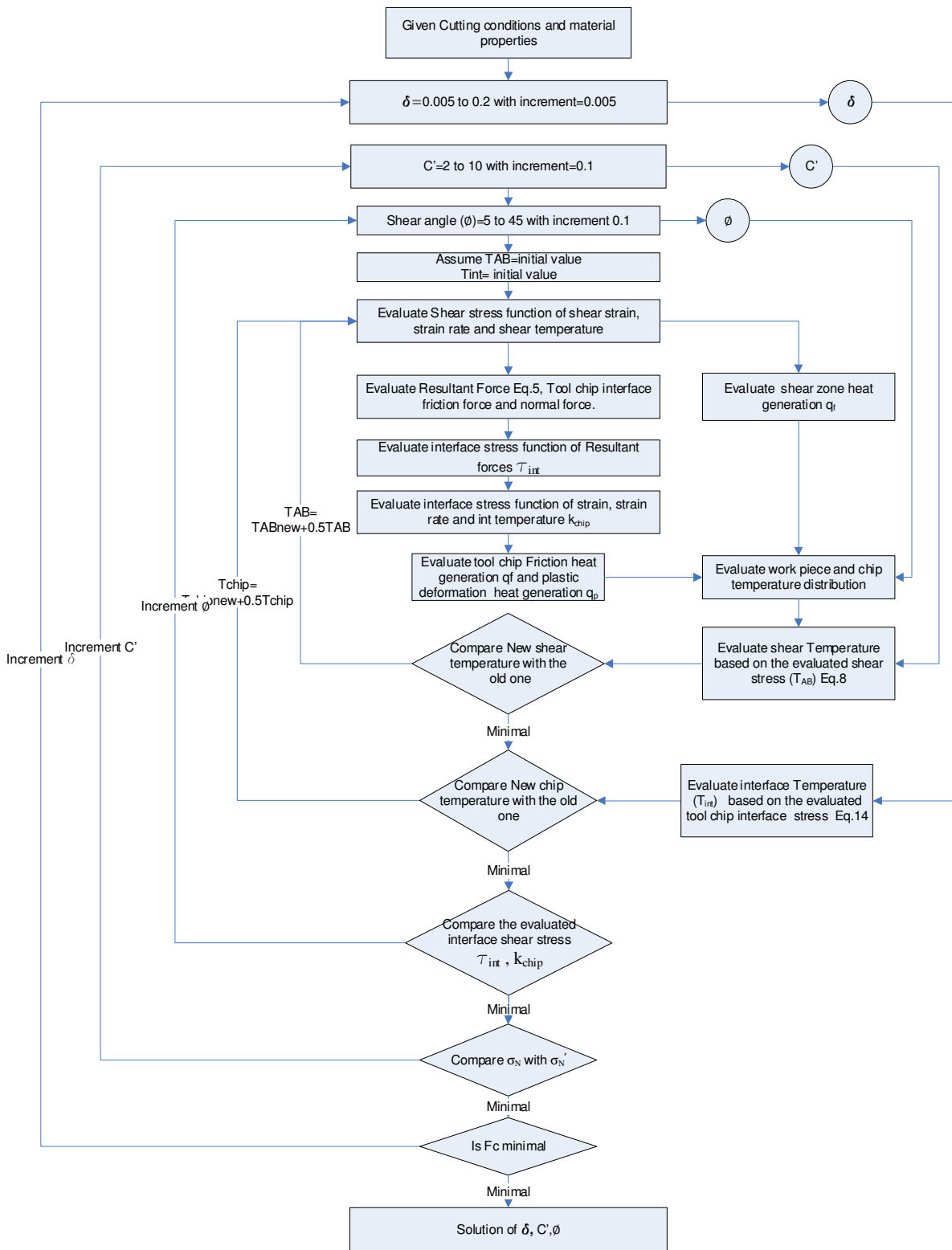


Figure 6.9. Flowchart illustrating the development and validation process for extending the thick shear zone to include ZA flow stress models for dual FCC/BCC material

For the range shear zone region $-\frac{S_1}{2}$ to 0 adopted the workpiece temperature distribution as $T_{Mshear}(x, z) = T_{work-shear}(x, z)$.

And for the range from 0 to $\frac{S_1}{2}$ adopted the chip temperature distribution as $T_{Mshear}(x, z) = T_{chip}(x', z')$

The tool chip interface temperature is calculated by the averaging the temperature within the secondary interface zone through integration, as presented in Eq. 6.34. The calculated mean tool chip interface adopted is used for extending the thick shear zone approach as presented by Karpap and Ozel [86]

$$T_{int} = \frac{1}{S_2} \frac{1}{l_c} \int_0^{S_2} \int_0^{l_{AB}} T_{Mshear}(x, z) + T_{M chip int}(x, z) dl_i dS_1 + T_o \quad (6.32)$$

Where Eq. 6.34 is a function of the secondary deformation zone thickness S_2 and tool chip contact length defined as L_c . As reported by Lalwani [19], the tool chip contact length is function of the shear angle ϕ , friction angle λ , resultant Force angle, θ , strain hardening index n' , and primary deformation zone thickness ratio, C' .

$$L_c = \frac{t_1 \sin \theta}{\cos \lambda \sin \phi} \left[1 + \frac{C' n'}{3(1+2(\frac{\pi}{4}-\phi)-C' n')} \right] \quad (6.33)$$

To the authors knowledge, coupling the moving heat source model with the extended thick shear zone approach is not implemented before. The Adoption of the moving heat source methodology is considered a development of the Oxley thick shear zone approach resulting in an improved machining simulation methodology.

G. Validation of Orthogonal cutting simulation methodology

Part of this work validation comparison of the conceived methodology temperature and force results against cutting forces, thrust forces, and tool chip interface temperature experimentally reported by Saglam [32] for AISI 1040 steel material using turning experiments.

In his work Saglam [32] reported tool surface temperature using a radiation thermometer in addition to cutting and thrust forces generated by the turning process. Presented in Table 6.3 are the set of turning experiments conditions adopted by Saglam [32] where reported experimentally measured cutting, thrust forces, and tool chip interface temperature.

Table 6.3 Drilling test matrix Saglam [32]

Exp #	Feed (mm/rev)	Cutting speed (m/min)	Rake angle (Degrees)
1	0.2	75	0
2	0.2	113	0
3	0.2	160	0
4	0.2	236	0
5	0.2	75	6
6	0.2	113	6
7	0.2	160	6
8	0.2	236	6
9	0.2	75	12
10	0.2	113	12
11	0.2	160	12
12	0.2	236	12
13	0.2	75	20
14	0.2	113	20
15	0.2	160	20
16	0.2	236	20

The Oxley dual BCC/FCC methodology, first reported by Seif et al. [52] is now extended to account for the closed-form thermal model solution presented in this research. The thermally extended Oxley Dual BCC and FCC Zerilli Armstrong material model is adapted for modeling steel material characterized by the temperature-dependent crystal structure. Inline with

Seif et al. [52], Zerilli-Armstrong model presented in Eq. 6.34 presented by Jaspers et al. [69] for AISI 1045 is adopted for the BCC temperature range.

$$\sigma = 159.2 + 1533.7 \exp\left(-6.09 * 10^{-3}T + 1.89 * 10^{-4}T \ln\left(\frac{\dot{\epsilon}}{\dot{\epsilon}_0}\right)\right) + 742.6\epsilon^{0.171} \quad (6.34)$$

Added to it the blue brittleness relation presented in Eq. 6.35 as presented by Zaeh et al. [71]

$$\sigma_B = 50.2 \exp(-0.0003(T - 673)^2) \quad (6.35)$$

And for the steel FCC crystal structure temperature range adopted the FCC the Mirzaie et al. [70] material model presented in Eq. 6.36

$$\sigma = 6771.175\epsilon^{0.232} \exp\left(-0.002953T + 0.00012T \ln\left(\frac{\dot{\epsilon}}{\dot{\epsilon}_0}\right)\right) \quad (6.36)$$

Presented in Figure 6.10, the temperature validation outcomes where tool chip interface temperature simulation results are compared against Saglam [32] experimentally reported results at cutting conditions listed in Table 6.3.

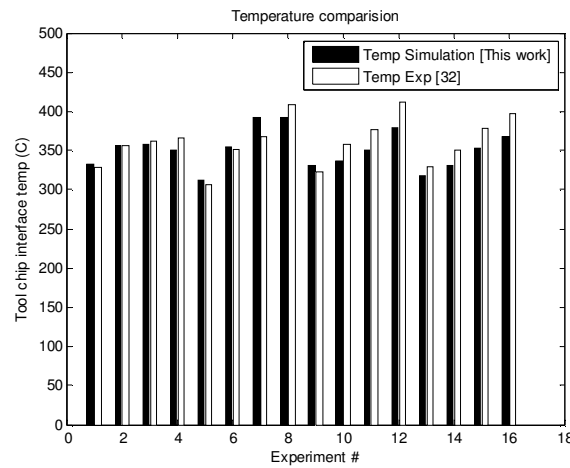


Figure 6.10. Comparison for AISI 1045 steel: a) interface Saglam [32] versus and Oxley-ZA extended methodology

This work thermally extended thick shear zone approach predicted well the measured tool chip interface temperature reported by Saglam [32] at identical operating conditions with achieved predictability mean error of 7.5%.

Described in Figures 6.11 are the cutting and thrust forces simulation results against Saglam [32] orthogonal tests results with achieved predictability error of 8.2 % for cutting forces and 11.3% for thrust forces. The achieved predictability of experimentally presented cutting forces, thrust forces and tool chip interface temperatures support the use of the thermally modified dual crystal structure BCC/FCC Zerilli Armstrong thick shear zone approach for predicting machining forces and operating temperatures.

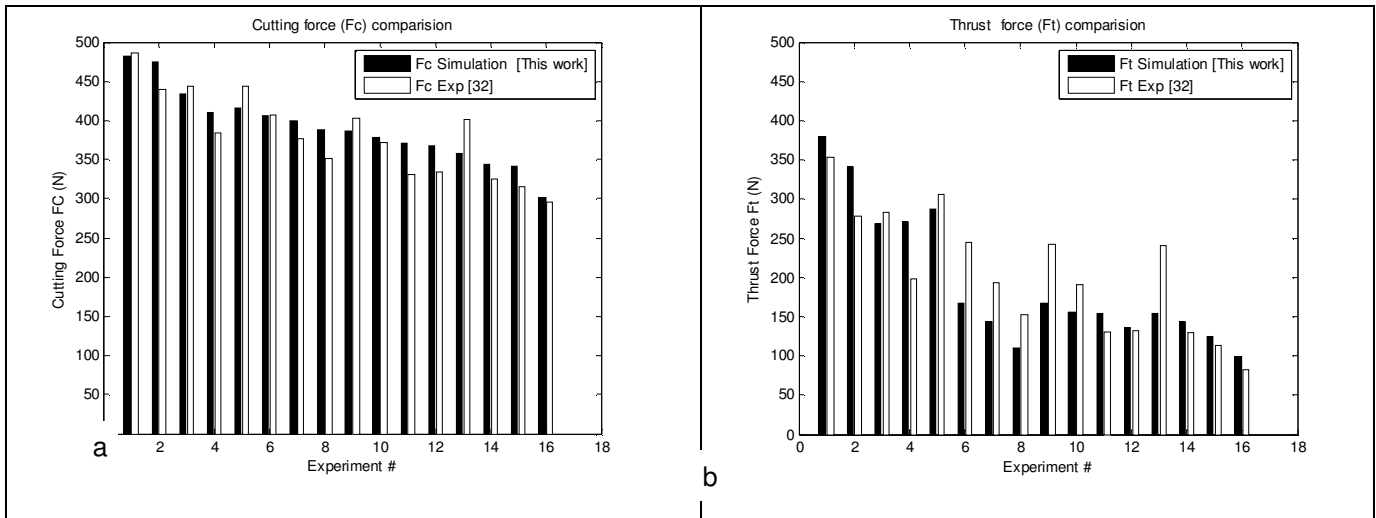


Figure 6.11. Comparison for AISI 1045 steel: a) Cutting Forces Saglam [32] versus and Oxley-ZA extended methodology b) thrust Forces Saglam [32] versus and Oxley-ZA extended methodology

H. Validation of Drilling simulation methodology

Considering the larger variation of machining conditions occurring along the drill bit cutting lip, adopted the use of the Drill lip force prediction module (DLFPM) reported by Seif et al. [88] coupled with the straight flute drill geometric characteristics reported in Table 6.1 characterized by a drill helix angle δ_0 at the outer plan equal to zero. As presented

diagrammatically in Figure 6.12, the DLFPM has been extended to account for the thermally extended thick shear zone approach adapted to Zerilli Armstrong FCC material model reported by Seif et al. [52].

Considering its wide use, in industry investigation is made for Aluminum 6061-T6 material having an FCC type Zerilli Armstrong model reported in Eq. 6.37, as presented by Lee et al. [74].

$$\sigma = 156.7 + 710.4\varepsilon^{0.624} \exp\left(-0.0055T + 0.00044T \ln\left(\frac{\dot{\varepsilon}}{\dot{\varepsilon}_0}\right)\right) \quad (6.37)$$

Targeting to validate the use of the Drill lip force prediction module coupled with the thermally extended Zerilli Armstrong thick shear zone approach, simulation results are compared against experimentally collected torque, thrust forces, and flank temperature. Reference to the proposed methodology diagrammatical representation reported in Figure 6.12, material flow stress presented in Eq. 6.37, along with cutting speed and uncut chip thickness, are used as input to the conceived methodology.

The cutting lip is divided into N elements and for each element is assigned the geometric tool conditions of cutting oblique and rake angles in addition to operating cutting conditions defined as the uncut chip thickness t_1 and cutting Speed V.

Function of the straight flute cutting lip geometric characteristics the oblique angle $i(\rho)$ as reported in Eq. 6.38. as presented by Askatov [100]

$$\sin(i(\rho)) = \sin(\theta(\rho))\sin(p) \quad (6.38)$$

Where p is the drill half-point angle and $\theta(\rho)$ is the local element web angle presented by Armarego[91] function of chisel edge web half-thickness w reported in Table 6.1 and r the element radial positions and described in Eq. 6.39.

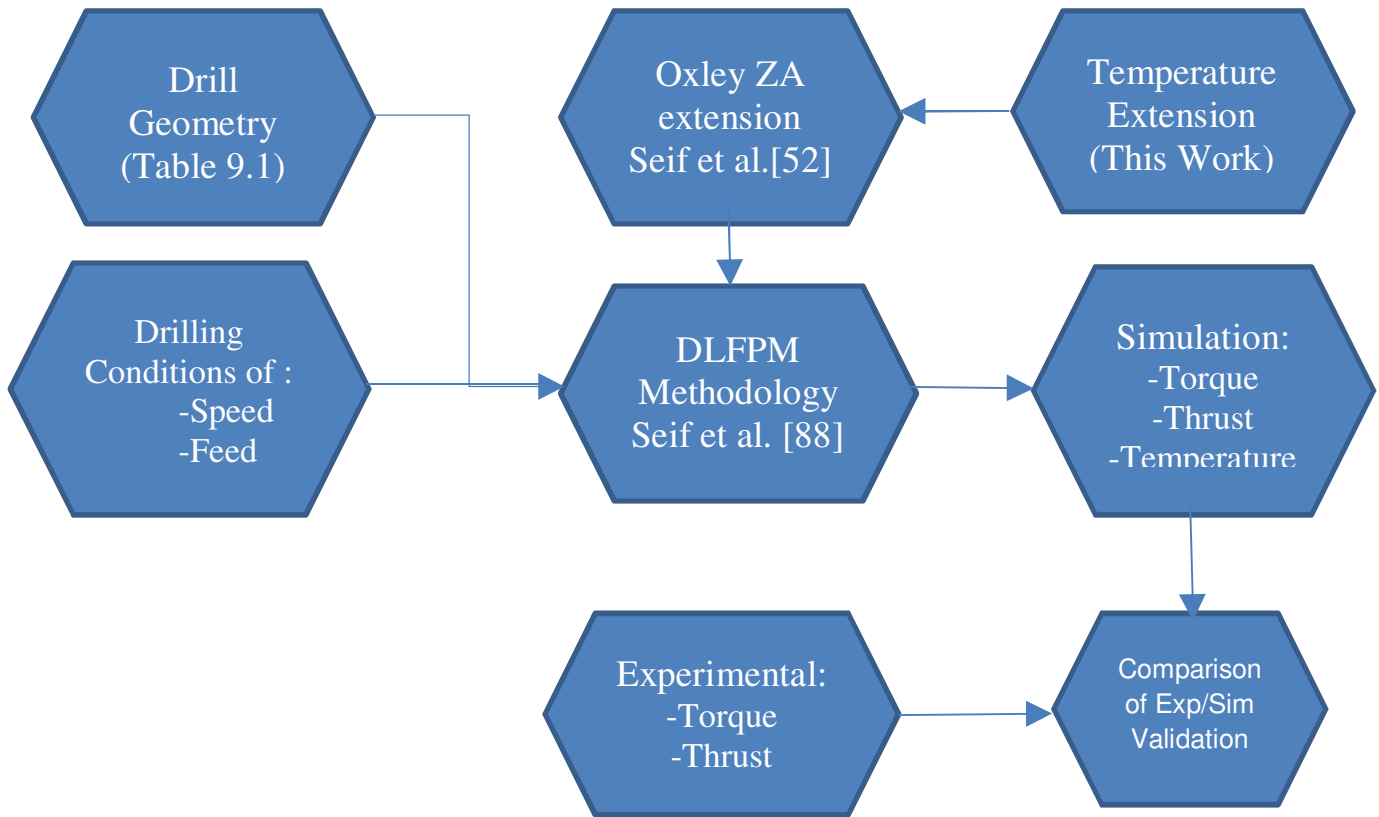


Figure 6.12 Drill Force and temperature simulation flow diagram

$$\theta(\rho) = \sin^{-1}\left(\frac{w}{r}\right) \quad (6.39)$$

Also normal rake angle α_n reported by Askatov [100] for drills having straight flutes follows Eq. 6.40:

$$\tan(\alpha_n) = -\theta(\rho) \cos(p) \quad (6.40)$$

With reference to Askatov [100] the local helix angle $\beta(\rho)$ equal to zero considering the adopted straight flute drill geometry.

As presented by Armarego[91], the resultant cutting speed angle η :

$$\tan(\eta) = \tan(i(\rho))\cos(\alpha_n) \quad (6.41)$$

The uncut chip thickness t_1 is calculated as a function of operational feed, f , and drill point half-angle, p , as

$$t_1 = \frac{f \sin(p)}{2} \quad (6.42)$$

The cutting speed along the lip is a function of rotational speed, ω , and varies as a function of normal radius as defined in Eq 6.43.

$$V(\rho) = \omega r \quad (6.43)$$

Reported by Agapiu et al. [90] The elemental force in the velocity direction ΔF_p , elemental force ΔF_q is normal to the velocity and the machined surface and elemental force ΔF_r is normal to both ΔF_p and ΔF_q as:

$$\Delta F_p = \frac{\tau * \Delta b * t_1 * \cos(i(\rho)) [\cos(\beta_n - \alpha_n) + \tan(i(\rho)) \tan(\eta) \sin(\lambda_n)]}{\sin(\phi_n) C_2} \quad (6.44)$$

$$\Delta F_q = \frac{\tau * \Delta b * t_1 * \sin(\lambda_n - \alpha_n)}{\sin(\phi_n) C_2} \quad (6.45)$$

$$\Delta F_r = \frac{\tau * \Delta b * t_1 * \cos(i(\rho)) [\cos(\beta_n - \alpha_n) \tan(i(\rho)) - \tan(\eta) \cos(\lambda_n)]}{\sin(\phi_n) C_2} \quad (6.46)$$

Where

$$C_2 = [\cos^2(\phi_n + \lambda_n - \alpha_n) + \tan^2(\eta) \sin^2(\lambda_n)]^{0.5} \quad (6.47)$$

The elemental forces are a function of the shear stress τ , shear angle ϕ_n , and normal friction angle λ_n are found using the thermally modified, ZA extended thick shear zone approach for each incremental lip element.

Reported by Williams [1] the torque and thrust generated at each lip element function of the element force components ΔF_p , ΔF_q , ΔF_r , calculated using Eq. 6.48 and 6.49

$$dM(\rho) = r \cdot F_p(r) \quad (6.48)$$

$$dF_t(\rho) = F_q(r) \sin(p) - F_r(r) \cos(p) \quad (6.49)$$

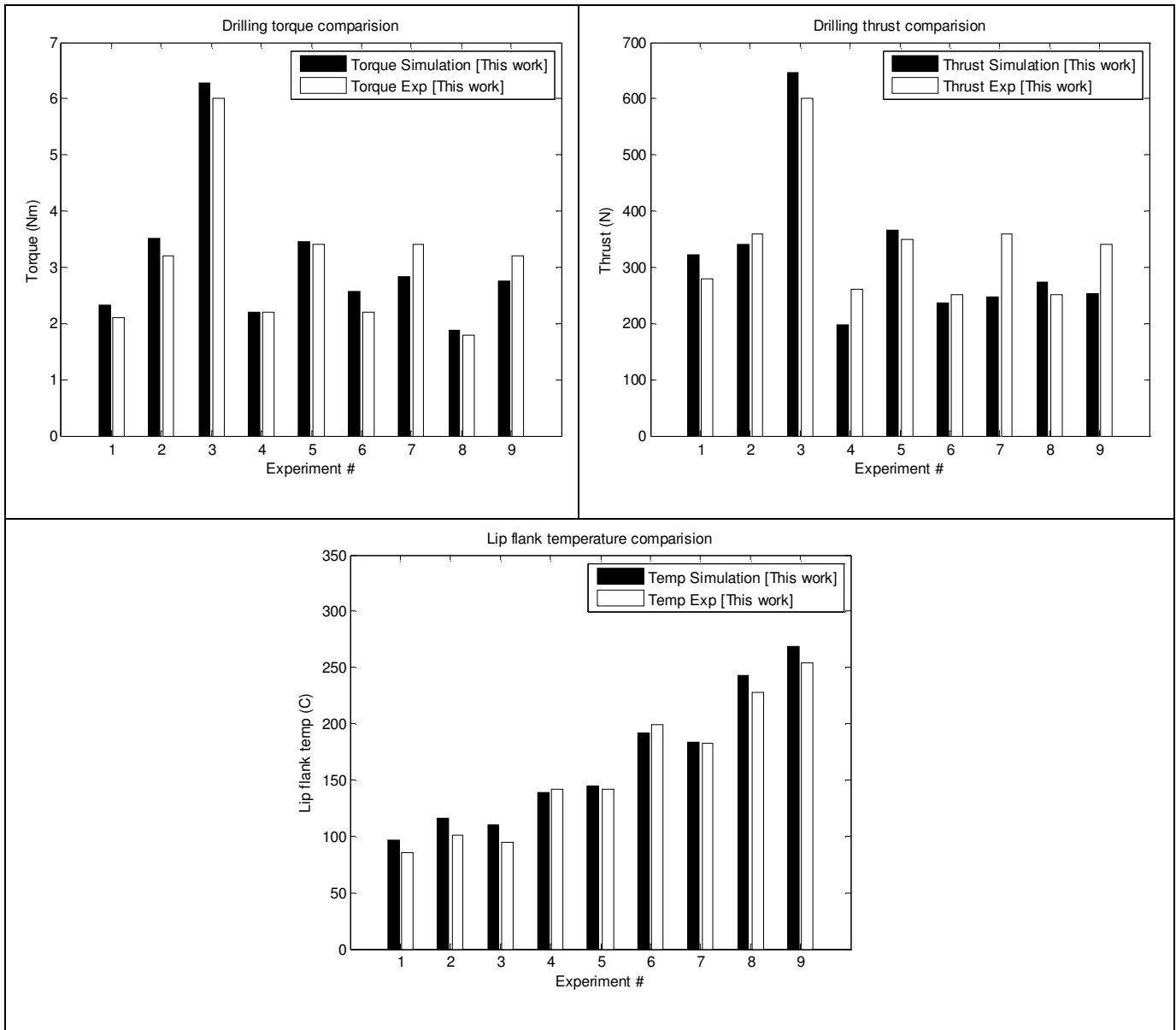


Figure 6.13. Comparison for Al 6161-T6: a) Drilling torque (this work) [32] versus and Oxley-ZA extended methodology b) Drilling thrust (this work) versus and Oxley-ZA extended methodology c) Flank temperature (this work) versus and Oxley-ZA extended methodology

The lip average steady-state tool chip interface temperature at each increment is found for the solution increment shear angle, friction angle, and resulting shear stress based on the thick shear zone approach extended for the ZA FCC model, accounting for the moving heat

source thermal model. The average steady-state tool chip interface temperature for the N number of elements is evaluated to be:

$$T_{int-s} = \frac{1}{N} \sum_{j=1}^N T_{int-s,j} \quad (6.50)$$

Based on the steady-state temperature at the tool chip interface, the occurring temperature at a distance X for the transient time t is estimated following Bergman et al. [101] as:

$$T(X, t) = T_{int-s} + erf\left(\frac{X}{2\sqrt{\alpha t}}\right) (T_i - T_{int-s}) \quad (6.51)$$

The adopted X value is 1.5mm, matching with the position of the thermocouples with respect to the tool chip interface and the drilling time adopted matches with the maximum drilling depth reached, as reported in Table 6.2. The Drill thermal diffusivity α is adopted to be 0.18cm²/s for carbide machining tools. Also, the initial drill temperature is defined as T_i matching with ambient conditions.

Reported in Figure 6.13 a, b and c is a comparison of simulation machining torque, thrust, and temperatures occurring a drill depth of 15mm matching with the drilling time reported in Table 6.1 achieving a mean predictability error of 8.7%, 14.5% and 7.2% for operating torque, thrust and temperature respectively. Also, part of validating the use of DLFPM methodology reported in Figure 6.14 simulated drilling flank surface temperature estimation following Eqs 6.50 and 6.51 function of the engaged cutting lip length and drilling operation time. Figure 6.14 simulation flank temperature compared well to experimentally collected flank surface temperature using the inverted drilling set up adopted for drilling Aluminum 6061-T6 material.

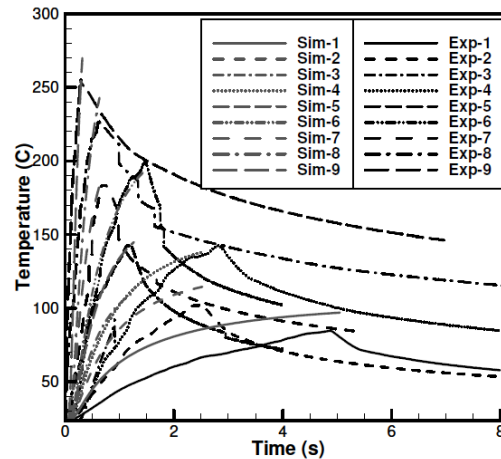


Figure 6.14. Simulated temperature versus experimentally collected flank temperature comparison

I. Discussion

Considering the development of available computational capabilities presented a thermal extension for Seif et al. [52] Oxley Zerilli Armstrong thick shear zone approach for modeling machining processes. The Adopted analytical closed-form solution for machining thermal modeling is in line with the 2D heat conduction laws and follows the moving heat source approach presented by Komanduri [83],[85], and [93]. The defined thermal model accounts for heat generated by the plastic deformation at the primary deformation zone, the friction heat generation occurring at the tool chip interface added to the heat caused by the plastic strain taking place at the secondary deformation zone. Turning experiments are considered for validation of the conceived thermally extend Zerilli Armstrong, thick shear approach. The AISI 1045 simulation cutting force, thrust force, and tool chip interface temperature predicted well Saglam [32] experimentally reported data with a mean error of 7.2%, 8.25, and 11.5%, respectively. Part of extending the conceived thick shear zone methodology to more complex machining processes, drilling experiments for Aluminum 60601-T6 is performed following the

inverted set up reported by Hamade et al. [77]. The presented thermally extended thick shear zone approach is coupled with Seif et al. [88] drill lip force prediction module to predict torque, thrust, and drill flank machining temperature following Agapiu et al. [90] flank face thermal model. The presented work achieved predictability of Aluminum 6061-T6 lip torque, thrust, and flank temperature with a mean error of 8.7%, 14.5%, and 7.2%, respectively. Also, the simulated transient flank temperature results predicted well experimentally collected flank temperature as presented in Figure 6.14. The Achieved predictability results makes the proposed thermally extended Zerilli Armstrong thick shear zone approach applicable for simulating simple (turning) and complex (drilling) machining processes.

J. Conclusion

The adoption of the closed-form moving heat source thermal model accounting for heat generated by the plastic deformation action occurring at the primary and secondary deformation zones added to the tool chip interface friction heat generation proved to predict well the machining thermal performance when coupled with Seif et al. [52] Oxley Zerilli Armstrong thick shear zone approach. Application for the proposed methodology is performed for simulating AISI 1045 turning tests reported in the literature with achieved R square predictability of 90%, 85% and 91% for experimentally reported tool chip interface temperature, cutting and thrust forces respectively. Also, the proposed methodology, once coupled with the Drill lip force prediction module (DLFPM) reported by Seif et al. [88], proved to predict also complex drilling machining processes. Drill lip machining simulation results achieved a predictably R square of 85%, 90 %, and 75% compared to Aluminum 6061-T6 experimentally collected drilling flank temperature, torque, and thrust. Comparison of the Drill lip machining simulation flank

temperature against FEM modeling will be considered as future development to this work. The presented machining simulation methodology based on the Oxley thick shear zone approach allows machinist to predict the response of the material under the different cutting instances to identify optimal machining conditions satisfying the minimum energy aims while minimizing the tool chip interface temperatures thus increasing the tool life.

CHAPTER VII

CONCLUSION

The presented thesis focuses on extending the thick shear zone approach machining force and temperature method which offers an improved understanding of phase changes mechanisms that occur during machining steel. This chapter summarizes the main research outcomes, followed by proposed future recommendations and developments.

A. Summary of Results and Contributions

Modeling machining processes is an important field investigated by researchers with a target to identify machining conditions that minimize operation time, power consumption, and tool wear. The presented research contributions are summarized below:

- 1 Implementing an orthogonal cutting turning setup for machining forces data collection necessary for validating the investigated modeling procedures.
- 2 Conceive an inverted drilling setup measuring cutting force and operating temperature. The inverted set up is also adopted for machining data collection.
- 3 Implementation the Drill Lip Cutting Force Prediction Methodology (DLCFPM) that estimated cutting lip forces based on the thick shear zone approach and utilize the developed methodology to find materials model using the inverse scheme. The methodology robustness is demonstrated by comparing torque and thrust forces profiles at progressive lip engagement using the DLCFPM-found JC parameter versus experimental torque and thrust profiles. DLCFPM predicted well the drilling torque forces but, to a lesser extent, the

drilling thrust forces where some deviations from the experimental thrust values are observed.

- 4 Investigation of AZ31B material characterized by an HCP material model and implementing the extension of the Oxley shear zone approach to account for the Zerilli Armstrong material model in the HCP forms to update the AZ31b magnesium alloy HCP material model through the inverse methodology. The presented methodology for updating HCP- Zerilli - Armstrong material model parameters based on orthogonal cutting tests is a complementary alternative to time-consuming standard flow stress tests.
- 5 Devise the extension of the Oxley thick shear zone approach to account for the Zerilli Armstrong material model in the BCC, FCC forms, and the validation of the proposed methodology is performed through comparison with experimental orthogonal cutting tests performed on AISI1045 and Aluminum 6061-T6 material. The work presents an additional step towards making Oxley thick shear zone approach a popular methodology considering the availability of Zerilli-Armstrong material models for a large number of metals.
- 6 Adopt the improved heat source machining thermal model for estimating operating temperatures involved in the cutting process as a substitute to Boothroyd[31] temperature estimation empirical approach adopted in the Oxley thick shear zone approach. Validation of the extension is made through comparison with temperature measurements collected from simple orthogonal and complex drilling setup. The presented machining simulation methodology is based on the Oxley thick shear zone approach allows machinist to predict the response of the material under the different cutting conditions to identify optimal machining conditions satisfying the minimum energy aims while minimizing the tool chip interface temperatures thus increasing the tool operating life.

B. Recommendations and Future Research Developments

Even though this research addressed the topic of machining force and temperature prediction methodologies, application of the presented work would be investigated in future research developments and comprise the below:

- 1- Extending the machining model to high plastic deformation cutting encountered along the drill bit chisel edge.
- 2- Adopting the presented modeling techniques in designing machining tools adapted to the response of the material cut. The application may be useful for designing novel tool geometry, engineered to optimize the machining process
- 3- Utilizing high-speed infra-red imaging to analyze the operating machining temperature distribution and identify conditions that improve the cutting process.

BIBLIOGRAPHY

- [1] R.A. Williams, A Study of the Drilling Process, *J. Eng. Ind.* 96 (1974) 1207.
<https://doi.org/10.1115/1.3438497>.
- [2] S. Wiriyacosol, E.J.A. Armarego, Thrust and Torque Prediction in Drilling From a Cutting Mechanics Approach, *CIRP Ann. Technol.* (1979) 87–91.
- [3] R.F. Hamade, C.Y. Seif, F. Ismail, Extracting cutting force coefficients from drilling experiments, *Int. J. Mach. Tools Manuf.* 46 (2006) 387–396.
<https://doi.org/10.1016/j.ijmachtools.2005.05.016>.
- [4] A.J.P. Sabberwal, An investigation into the chip section and cutting forces during milling operations, (1961).
- [5] B. Rao, Y.C. Shin, Analysis on high-speed face-milling of 7075-T6 aluminum using carbide and diamond cutters, *Int. J. Mach. Tools Manuf.* 41 (2001) 1763–1781.
- [6] S.G. Chandrasekharan, V., Kapoor, A Mechanistic Approach to Predicting the Cutting Forces in Drilling : With Application to Fiber-Reinforced Composite Materials, *J. Eng. Ind.* Novemb. 1, 1995 117(4)559. 1 (1996).
- [7] D.A. Stephenson, P. Bandyopadhyay, Process-independent force characterization for metal-cutting simulation, *J. Eng. Mater. Technol.* 119 (1997) 86–94.
- [8] K.P. Kumar, K. Kishore, P. Laxminarayana, Prediction of thrust force and torque in drilling on aluminum 6061-T6 alloy, *Int. J. Eng. Res. Technol.* 2 (2013) 181–2278.
- [9] C.J. Oxford Jr, On the drilling of metals 1: basic mechanics of the process, *Trans. ASME.* 77 (1955) 103–111.
- [10] A.K. Pal, A. Bhattacharyy, G.C. Sen, Investigation of the torque in drilling ductile materials, *Int. J. Mach. Tool Des. Res.* 4 (1965) 205–221.
- [11] M.E. Merchant, Mechanics of the metal cutting process. I. Orthogonal cutting and a type 2 chip, *J. Appl. Phys.* 16 (1945) 267–275.

- [12] J. Kouam, A. Djebara, V. Songmene, Experimental investigation on the effect of pre-holes on drilling process performance of aluminum alloys: Forces, surface finish and dust emission, *Adv. Mater. Sci. Appl.* 3 (2014) 13–23.
- [13] P.L.B. Oxley, *The Mechanics of Machining: An Analytical Approach to Assessing Machinability*, Ellis Horwood, 1989.
- [14] V. Piispanen, Theory of formation of metal chips, *J. Appl. Phys.* 19 (1948) 876–881.
- [15] H. Ernst, *Machining of metals*, American Society for Metals, 1938.
- [16] A.R. Watson, Drilling model for cutting lip and chisel edge and comparison of experimental and predicted results. IV—drilling tests to determine chisel edge contribution to torque and thrust, *Int. J. Mach. Tool Des. Res.* 25 (1985) 393–404.
- [17] M. Elhachimi, S. Torbaty, P. Joyot, Mechanical modelling of high speed drilling . 1 : predicting torque and thrust, 39 (1999) 553–568.
- [18] G.R. Johnson, W.H. Cook, A constitutive model and data for metals subjected to large strains, high strain rates and high temperatures, 7th Int. Symp. Ballist. (1983) 541–547. <https://doi.org/10.1038/nrm3209>.
- [19] D.I. Lalwani, N.K. Mehta, P.K. Jain, Extension of Oxley’s predictive machining theory for Johnson and Cook flow stress model, *J. Mater. Process. Technol.* 209 (2009) 5305–5312. <https://doi.org/10.1016/j.jmatprotec.2009.03.020>.
- [20] M. Daoud, W. Jomaa, J.F. Chatelain, A. Bouzid, V. Songmene, Identification of material constitutive law constants using machining tests: a response surface methodology based approach, 2014 Int. Conf. High Perform. Optim. Des. Struct. Mater. 137 (2014) 25–36. <https://doi.org/10.2495/HPSM140031>.
- [21] Y.B. Guo, An integral method to determine the mechanical behavior of materials in metal cutting, *J. Mater. Process. Technol.* 142 (2003) 72–81. [https://doi.org/10.1016/S0924-0136\(03\)00462-X](https://doi.org/10.1016/S0924-0136(03)00462-X).
- [22] P. Naik, A. Naik, Determination of Flow Stress Constants by Oxley ‘ s Theory, *IJLTEMAS. IV* (2015) 110–116.

- [23] F.J. Zerilli, Dislocation mechanics-based constitutive equations, *Metall. Mater. Trans. A.* 35 (2004) 2547–2555.
- [24] A.H. Ammouri, R.F. Hamade, On the selection of constitutive equation for modeling the friction stir processes of twin roll cast wrought AZ31B, *Mater. Des.* 57 (2014) 673–688.
- [25] D. Hasenpouth, Tensile high strain rate behavior of AZ31B magnesium alloy sheet, (2010).
- [26] F.J. Zerilli, R.W. Armstrong, Dislocation-mechanics-based constitutive relations for material dynamics calculations, *J. Appl. Phys.* 61 (1987) 1816–1825.
<https://doi.org/10.1063/1.338024>.
- [27] P.L.B. Oxley, Rate of strain effect in metal cutting, *Trans. ASME J. Engng Indust.* 85 (1963) 335–338.
- [28] I.E. Dolzhenkov, The nature of blue brittleness of steel, *Met. Sci. Heat Treat.* 13 (1971) 220–224.
- [29] A.H. Adibi-Sedeh, V. Madhavan, B. Bahr, Extension of Oxley’s analysis of machining to use different material models, *J. Manuf. Sci. Eng.* 125 (2003) 656–666.
- [30] P.L.B. Oxley, Modelling machining processes with a view to their optimization and to the adaptive control of metal cutting machine tools, *Robot. Comput. Integr. Manuf.* 4 (1988) 103–119. [https://doi.org/10.1016/0736-5845\(88\)90065-8](https://doi.org/10.1016/0736-5845(88)90065-8).
- [31] G. Boothroyd, Temperatures in orthogonal metal cutting, *Proc. Inst. Mech. Eng.* 177 (1963) 789–810.
- [32] H. Saglam, S. Yaldiz, F. Unsacar, *Materials & Design* The effect of tool geometry and cutting speed on main cutting force and tool tip temperature, 28 (2007) 101–111.
<https://doi.org/10.1016/j.matdes.2005.05.015>.
- [33] S. Kalpakjian, *Manufacturing engineering and technology*, (1992) xix, 1258, 21 p.
<file://catalog.hathitrust.org/Record/002505825>.
- [34] A. Shrot, M. Bäker, Determination of Johnson–Cook parameters from machining

- simulations, *Comput. Mater. Sci.* 52 (2012) 298–304.
- [35] R.F. Hamade, F. Ismail, A case for aggressive drilling of aluminum, *J. Mater. Process. Technol.* 166 (2005) 86–97. <https://doi.org/10.1016/j.jmatprotec.2004.07.099>.
- [36] G.R. Johnson, R.A. Stryk, T.J. Holmquist, J.A. Schonhardt, C.R. Burns, User Instructions for the Final Version of the EPIC Research Code, 600 Second Street, N.E. Hopkins, MN 55343, 1994. <https://doi.org/WL-TR-96-7028>.
- [37] W.K. Rule, A numerical scheme for extracting strength model coefficients from Taylor test data, *Int. J. Impact Eng.* 19 (1997) 797–810. [https://doi.org/10.1016/S0734-743X\(97\)00015-8](https://doi.org/10.1016/S0734-743X(97)00015-8).
- [38] W. Dabboussi, J.A. Nemes, Modeling of ductile fracture using the dynamic punch test, *Int. J. Mech. Sci.* 47 (2005) 1282–1299. <https://doi.org/10.1016/j.ijmecsci.2005.01.015>.
- [39] A. Manes, L. Peroni, M. Scapin, M. Giglio, Analysis of strain rate behavior of an Al 6061 T6 alloy, in: *Procedia Eng.*, 2011: pp. 3477–3482. <https://doi.org/10.1016/j.proeng.2011.04.573>.
- [40] G.C.I. Lin, Prediction of cutting forces and chip geometry in oblique machining from flow stress properties and cutting conditions, *Int. J. Mach. Tool Des. Res.* 18 (1978) 117–130. [https://doi.org/10.1016/0020-7357\(78\)90003-3](https://doi.org/10.1016/0020-7357(78)90003-3).
- [41] G. V Stabler, The fundamental geometry of cutting tools, *Proc. Inst. Mech. Eng.* 165 (1951) 14–26.
- [42] P. Mathew, P.L.B. Oxley, Predicting the effects of very high cutting speeds on cutting forces, etc., *CIRP Ann.* 31 (1982) 49–52.
- [43] Y.C. Shin, A.J. Waters, A new procedure to determine instantaneous cutting force coefficients for machining force prediction, *Int. J. Mach. Tools Manuf.* 37 (1997) 1337–1351. [https://doi.org/10.1016/S0890-6955\(96\)00093-4](https://doi.org/10.1016/S0890-6955(96)00093-4).
- [44] I.S. Boldyrev, I.A. Shchurov, A. V. Nikonov, Numerical Simulation of the Aluminum 6061-T6 Cutting and the Effect of the Constitutive Material Model and Failure Criteria on Cutting Forces' Prediction, in: *Procedia Eng.*, 2016: pp. 866–870.

<https://doi.org/10.1016/j.proeng.2016.07.031>.

- [45] M. Easton, A. Beer, M. Barnett, C. Davies, G. Dunlop, Y. Durandet, S. Blacket, T. Hilditch, P. Beggs, Magnesium alloy applications in automotive structures, *Jom.* 60 (2008) 57.
- [46] T. Ozel, Development of a predictive machining simulator for orthogonal metal cutting process, in: *Proc. 4th Int. Conf. Eng. Des. Autom.* July, 2000.
- [47] R. Stevenson, The measurement of parasitic forces in orthogonal cutting, *Int. J. Mach. Tools Manuf.* 38 (1998) 113–130.
- [48] Y.B. Guo, Y.K. Chou, The determination of ploughing force and its influence on material properties in metal cutting, *J. Mater. Process. Technol.* 148 (2004) 368–375.
- [49] C.Y. Seif, I.S. Hage, R.F. Hamade, Determining cutting pressure coefficients for aluminum 6061-T6 using a small number of drilling experiments, in: *ASME Int. Mech. Eng. Congr. Expo. Proc.*, 2018. <https://doi.org/10.1115/IMECE2018-86224>.
- [50] R.W. Armstrong, F.J. Zerilli, Dislocation mechanics based viscoplasticity description of fcc, bcc, and hcp metal deformation and fracturing behaviors, *Proc. ASME Mater. Div.*, MD-69-1. (1995) 417–428.
- [51] A.H. Adibi-Sedeh, V. Madhavan, Effect of some modifications to oxley's machining theory and the applicability of different material models, *Mach. Sci. Technol.* 6 (2002) 379–395.
- [52] R.F.H. Charbel Y. Seif, Ilige S. Hage, Incorporating Dual BCC/FCC Zerilli-Armstrong and Blue Brittleness Constitutive Material Models into Oxley's Machining Shear Zone Theory," *J. Manuf. Process.* (n.d.).
- [53] J.J. Valencia, P. Quested, Thermophysical properties, *Model. Cast. Solidif. Process.* 189 (2001).
- [54] R.F.H. Charbel Y. Seif, Ilige S. Hage, Utilizing the Drill Cutting Lip to Extract Johnson Cook Flow Stress Parameters for Al6061-T6, *CIRP J. Manuf. Sci. Technol.* (n.d.).

- [55] F. Feng, S. Huang, Z. Meng, J. Hu, Y. Lei, M. Zhou, Z. Yang, A constitutive and fracture model for AZ31B magnesium alloy in the tensile state, *Mater. Sci. Eng. A.* 594 (2014) 334–343.
- [56] S. Akram, S.H.I. Jaffery, M. Khan, M. Fahad, A. Mubashar, L. Ali, Numerical and experimental investigation of Johnson–Cook material models for aluminum (Al 6061-T6) alloy using orthogonal machining approach, *Adv. Mech. Eng.* 10 (2018) 1687814018797794.
- [57] P. Albrecht, New developments in the theory of the metal-cutting process: part I. The ploughing process in metal cutting, *J. Eng. Ind.* 82 (1960) 348–357.
- [58] C.Y. Gao, L.C. Zhang, H.X. Yan, A new constitutive model for HCP metals, *Mater. Sci. Eng. A.* 528 (2011) 4445–4452.
- [59] R. Viswanathan, S. Ramesh, V. Subburam, Measurement and optimization of performance characteristics in turning of Mg alloy under dry and MQL conditions, *Measurement.* 120 (2018) 107–113.
- [60] M.N.A. Nasr, J.C. Outeiro, Sensitivity analysis of cryogenic cooling on machining of magnesium alloy AZ31B-O, *Procedia CIRP.* 31 (2015) 264–269.
- [61] S. Kurukuri, M.J. Worswick, D. Ghaffari Tari, R.K. Mishra, J.T. Carter, Rate sensitivity and tension–compression asymmetry in AZ31B magnesium alloy sheet, *Philos. Trans. R. Soc. A Math. Phys. Eng. Sci.* 372 (2014) 20130216.
- [62] S.A. Iqbal, P.T. Mativenga, M.A. Sheikh, Characterization of machining of AISI 1045 steel over a wide range of cutting speeds. Part 2: evaluation of flow stress models and interface friction distribution schemes, *Proc. Inst. Mech. Eng. Part B J. Eng. Manuf.* 221 (2007) 917–926.
- [63] K. Maekawa, T. Shirakashi, E. Usui, Flow stress of low carbon steel at high temperature and strain rate. ii: flow stress under variable temperature and variable strain rate, *Bull. Japan Soc. Precis. Eng.* 17 (1983) 167–172.
- [64] N. Fang, A New Quantitative Sensitivity Analysis of the Flow Stress of 18 Engineering

- Materials in Machining, *J. Eng. Mater. Technol.* 127 (2005) 192.
<https://doi.org/10.1115/1.1857935>.
- [65] G.J. Long, H.P. Leighty Jr, The iron-iron carbide phase diagram: A practical guide to some descriptive solid state chemistry, *J. Chem. Educ.* 59 (1982) 948.
- [66] H. Ding, Y.C. Shin, A metallo-thermomechanically coupled analysis of orthogonal cutting of AISI 1045 steel, *J. Manuf. Sci. Eng.* 134 (2012) 51014.
- [67] D.R. Lesuer, G.J. Kay, M.M. LeBlanc, Modeling large-strain, high-rate deformation in metals, *Third Bienn. Tri-Laboratory Eng. Conf. Model. Simul.* (2001) 3–5. <https://e-reports-ext.llnl.gov/pdf/243782.pdf%5Cnpapers2://publication/uuid/04B1CA64-2CAF-40B9-8E26-61527F12AE97>.
- [68] A.L. Gurson, Continuum theory of ductile rupture by void nucleation and growth: Part I—Yield criteria and flow rules for porous ductile media, *J. Eng. Mater. Technol.* 99 (1977) 2–15.
- [69] S.P.F.C. Jaspers, J.H. Dautzenberg, Material behaviour in conditions similar to metal cutting: Flow stress in the primary shear zone, *J. Mater. Process. Technol.* 122 (2002) 322–330. [https://doi.org/10.1016/S0924-0136\(01\)01228-6](https://doi.org/10.1016/S0924-0136(01)01228-6).
- [70] T. Mirzaie, H. Mirzadeh, J.M. Cabrera, A simple Zerilli-Armstrong constitutive equation for modeling and prediction of hot deformation flow stress of steels, *Mech. Mater.* 94 (2016) 38–45. <https://doi.org/10.1016/j.mechmat.2015.11.013>.
- [71] M.F. Zaeh, F. Schwarz, Implementation of a process and structure model for turning operations, *Prod. Eng.* 3 (2009) 197–205.
- [72] K. Okushima, K. Hitomi, An analysis of the mechanism of orthogonal cutting and its application to discontinuous chip formation, *J. Eng. Ind.* 83 (1961) 545–555.
- [73] N.N. Zorev, Inter-relationship between shear processes occurring along tool face and shear plane in metal cutting, *Int. Res. Prod. Eng.* 49 (1963) 143–152.
- [74] W.S. Lee, Z.C. Tang, Relationship between mechanical properties and microstructural response of 6061-T6 aluminum alloy impacted at elevated temperatures, *Mater. Des.* 58

- (2014) 116–124. <https://doi.org/10.1016/j.matdes.2014.01.053>.
- [75] P. Sartkulvanich, F. Koppka, T. Altan, Determination of flow stress for metal cutting simulation—a progress report, *J. Mater. Process. Technol.* 146 (2004) 61–71.
- [76] R.W. Ivester, M. Kennedy, M. Davies, R. Stevenson, J. Thiele, R. Furness, S. Athavale, Assessment of machining models: progress report, *Mach. Sci. Technol.* 4 (2000) 511–538. <https://doi.org/10.1080/10940340008945720>.
- [77] R.F. Hamade, I.S. Jawahir, Core drilling versus chisel drilling with an eye on sustainability, in: *ASME 2009 Int. Mech. Eng. Congr. Expo.*, American Society of Mechanical Engineers Digital Collection, 2009: pp. 61–66.
- [78] P.L.B. Oxley, H.T. Young, *The Mechanics of Machining: An Analytical Approach to Assessing Machinability*, Ellis Horwood Publ. (1989) 136–182.
- [79] S. Jaspers, J.H. Dautzenberg, D.A. Taminiau, Temperature measurement in orthogonal metal cutting, *Int. J. Adv. Manuf. Technol.* 14 (1998) 7–12.
- [80] A.O. Tay, M.G. Stevenson, G. de Vahl Davis, Using the finite element method to determine temperature distributions in orthogonal machining, *Proc. Inst. Mech. Eng.* 188 (1974) 627–638.
- [81] R.S. Hahn, On the temperature developed at the shear plane in the metalcutting process, in: *J. Appl. Mech.* ASME, ASME-AMER SOC MECHANICAL ENG 345 E 47TH ST, NEW YORK, NY 10017, 1951: p. 323.
- [82] K.J. Trigger, An analytical evaluation of metal-cutting temperatures, *Trans. ASME.* 73 (1951) 57.
- [83] R. Komanduri, Z.B. Hou, Thermal modeling of the metal cutting process: Part I—Temperature rise distribution due to shear plane heat source, *Int. J. Mech. Sci.* 42 (2000) 1715–1752.
- [84] S. Chenwei, X. Zhang, S. Bin, D. Zhang, An improved analytical model of cutting temperature in orthogonal cutting of Ti6Al4V, *Chinese J. Aeronaut.* 32 (2019) 759–769.

- [85] R. Komanduri, Z.B. Hou, Thermal modeling of the metal cutting process—Part II: temperature rise distribution due to frictional heat source at the tool–chip interface, *Int. J. Mech. Sci.* 43 (2001) 57–88.
- [86] Y. Karpat, T. Özel, Predictive Analytical and Thermal Modeling of Orthogonal Cutting Process—Part II: Effect of Tool Flank Wear on Tool Forces, Stresses, and Temperature Distributions, *J. Manuf. Sci. Eng.* 128 (2006) 445. <https://doi.org/10.1115/1.2162591>.
- [87] A.R. Watson, Drilling model for cutting lip and chisel edge and comparison of experimental and predicted results. I—initial cutting lip model, *Int. J. Mach. Tool Des. Res.* 25 (1985) 347–365.
- [88] C.Y. Seif, I.S. Hage, R.F. Hamade, Utilizing the drill cutting lip to extract Johnson Cook flow stress parameters for Al6061-T6, *CIRP J. Manuf. Sci. Technol.* (2019).
- [89] D.I. Lalwani, N.K. Mehta, P.K. Jain, Extension of Oxley’s predictive machining theory for Johnson and Cook flow stress model, *J. Mater. Process. Technol.* 209 (2009) 5305–5312. <https://doi.org/10.1016/j.jmatprotec.2009.03.020>.
- [90] J.S. Agapiou, M.F. DeVries, On the determination of thermal phenomena during drilling—Part I. Analytical models of twist drill temperature distributions, *Int. J. Mach. Tools Manuf.* 30 (1990) 203–215.
- [91] E.J.A. Armarego, C.Y. Cheng, Drilling with flat rake face and conventional twist drills—I. theoretical investigation, *Int. J. Mach. Tool Des. Res.* 12 (1972) 17–35.
- [92] B.T. Chao, The significance of the thermal number in metal machining, *Trans. ASME.* 75 (1953) 109–120.
- [93] R. Komanduri, Z.B. Hou, Thermal modeling of the metal cutting process—Part III: temperature rise distribution due to the combined effects of shear plane heat source and the tool–chip interface frictional heat source, *Int. J. Mech. Sci.* 43 (2001) 89–107.
- [94] J.H. Wiener, Shear-plane temperature distribution in orthogonal cutting, *Trans. ASME.* 77 (1955) 1331–1341.
- [95] H.T. Young, T.L. Chou, Modelling of tool/chip interface temperature distribution in metal

- cutting, *Int. J. Mech. Sci.* 36 (1994) 931–943.
- [96] R. Kapoor, S. Nemat-Nasser, Determination of temperature rise during high strain rate deformation, *Mech. Mater.* 27 (1998) 1–12.
- [97] J. Kajberg, K.-G. Sundin, Material characterisation using high-temperature Split Hopkinson pressure bar, *J. Mater. Process. Technol.* 213 (2013) 522–531.
- [98] Y. Huang, S.Y. Liang, Cutting temperature modeling based on non-uniform heat intensity and partition ratio, *Mach. Sci. Technol.* 9 (2005) 301–323.
- [99] K. Huang, W. Yang, Analytical model of temperature field in workpiece machined surface layer in orthogonal cutting, *J. Mater. Process. Technol.* 229 (2016) 375–389.
- [100] V.P. Astakhov, *Geometry of single-point turning tools and drills: fundamentals and practical applications*, Springer Science & Business Media, 2010.
- [101] T.L. Bergman, F.P. Incropera, D.P. DeWitt, A.S. Lavine, *Fundamentals of heat and mass transfer*, John Wiley & Sons, 2011.
- [102] P.L.B. Oxley, *Modelling machining processes with a view to their optimization and to the adaptive control of metal cutting machine tools.*, (1988) 242 p.
<file://catalog.hathitrust.org/Record/001299715>.

APPENDIX 1

Table S-1a. Shear Zone Model validation results for 0.2% carbon and rake angle of -5 degrees

Uncut chip thickness $t_1=0.125$ mm			Uncut chip thickness $t_1=0.250$ mm		
Speed m/min	Chip thickness t_2 mm [27]	Chip thickness t_2 , this work	Speed m/min	Chip thickness t_2 mm [27]	Chip thickness t_2 , this work
100	0.6	0.6	50	1.09	1.07
200	0.48	0.5	100	0.91	0.91
300	0.44	0.45	200	0.76	0.78
400	0.39	0.42	300	0.71	0.73
			400	0.67	0.69

Table S-1b. Shear Zone Model validation results for 0.38% carbon and rake angle of +5 degrees case

Uncut chip thickness $t_1=0.125$ mm			Uncut chip thickness $t_1=0.250$ mm		
Speed m/min	Chip thickness t_2 mm [30]	Chip thickness t_2 , this work	Speed m/min	Chip thickness t_2 mm [30]	Chip thickness t_2 , this work
100	0.43	0.42	50	0.75	0.75
200	0.33	0.34	100	0.62	0.63
300	0.32	0.31	200	0.54	0.54
			300	0.51	0.5

Table S-2. JC extended Shear Zone Model validation results for 0.38% carbon steel

Input				Published Model Results [102] (published in [19])		Our duplicated Model Results, this work	
Test #	Rake angle (Degrees)	t_1 (mm)	Speed (m/min)	Cutting Force F_c (N/mm)	Thrust Force F_t (N/mm)	Cutting Force F_c (N/mm)	Thrust Force F_t (N/mm)
1	-5	0.125	100	347	257	345.7	242.0
2	-5	0.125	200	297	185	295.7	180.2
3	-5	0.125	400	260	133	262.9	132.1
4	-5	0.25	100	589	369	593.2	362.3
5	-5	0.25	200	519	268	518.8	260.7
6	-5	0.5	100	1027	535	1023.7	514.4

APPENDIX 2

Appendix A

This section reports the extension of Oxley thick shears based on the BCC Zerilli-Armstrong constitutive analytical model [26] inline with reported Lalwani et al. [19], Johnson Cook [18] material model thick shear zone approach extension. Using Eq. 5.1 BCC Zerilli-Armstrong constitutive and Von Mises flow rule, the material shear flow stress k_{AB} at the shear plane AB is described by

$$k_{AB} = \frac{c_0 + c_1 \exp(-c_3 T + c_4 T \ln(\dot{\epsilon})) + c_5 (\epsilon)^n}{\sqrt{3}} \quad (A1)$$

The flowchart in Figure 5.4 illustrates how the equivalent Zerilli Armstrong strain hardening index n_{eq} is found. The $(dk/ds_1)_{AB}$ term is the variation of the shear flow stress across the width of the parallel-sided thick shear zone. Since the shear stress is a function of strain, strain rate, and temperature, the term $(dk/ds_1)_{AB}$ is

$$\begin{aligned} \left(\frac{dk}{ds_1}\right)_{AB} &= \left(\frac{dk}{d\gamma}\right)_{AB} \left(\frac{d\gamma}{dt}\right)_{AB} \left(\frac{dt}{ds_1}\right)_{AB} + \left(\frac{dk}{d\dot{\gamma}}\right)_{AB} \left(\frac{d\dot{\gamma}}{ds_1}\right)_{AB} + \\ &\left(\frac{dk}{dT}\right)_{AB} \left(\frac{dT}{ds_1}\right)_{AB} \end{aligned} \quad (A2)$$

Where k , γ , $\dot{\gamma}$, s_1 , T represent stress, shear strain, shear strain rate, thickness, and operating temperature T , coinciding with the shear plane deformation zone, respectively.

Considering that strain rate is maximum at the shear plane, the second term of Eq. A2

“ $\left(\frac{dk}{d\dot{\gamma}}\right)_{AB} \left(\frac{d\dot{\gamma}}{ds_1}\right)_{AB}$ ” reduces to zero. The steady-state assumption is applied, and the temperature

variation across the primary deformation zone is negligible, the third term of Eq. A2

“ $\left(\frac{dk}{dT}\right)_{AB} \left(\frac{dT}{ds_1}\right)_{AB}$ ” is also reduced to zero. Based on the Von Mises flow rule the term “ $\left(\frac{dk}{d\gamma}\right)_{AB}$ ” in

Eq. A2 formulated as

$$\left(\frac{dk}{d\gamma}\right)_{AB} = \left(\frac{d\left(\frac{\sigma_{AB}}{\sqrt{3}}\right)}{d\left(\sqrt{3}\varepsilon_{AB}\right)}\right)_{AB} = \frac{d\sigma_{AB}}{3d\varepsilon_{AB}} \quad (A3)$$

Where σ_{AB} and ε_{AB} are the operating stress and strain occurring at the shear plane.

The “ $\left(\frac{d\gamma}{dt}\right)_{AB}$ ” term is the strain rate at the shear plane and is a function of shear plane

velocity, V_s , primary deformation zone thickness ratio, C' , and shear plane length, l , as

$$\left(\frac{d\gamma}{dt}\right)_{AB} = \dot{\gamma} = \frac{C'V_s}{l} \quad (A4)$$

And the “ $\left(\frac{dt}{ds_1}\right)_{AB}$ ” term is the reciprocal of the velocity normal to the shear plane AB

denoted as V .

$$\left(\frac{dt}{ds_1}\right)_{AB} = \frac{1}{V\sin\phi} \quad (A5)$$

Substituting Eqs. A3, A4, and A5 in Eq. A2 yields

$$\left(\frac{dk}{ds_1}\right)_{AB} \frac{l}{2k_{AB}} = \left(\frac{d\sigma_{AB}}{3d\varepsilon_{AB}}\right) \left(\frac{C_0V_s}{l}\right) \left(\frac{1}{V\sin\phi}\right) \frac{l}{2k_{AB}} \quad (A6)$$

Rearranging the terms and using the shear strain term in Eq. A7 and Von Mises shear stress yield Eq. A8 where Oxley's primary deformation zone thickness ratio, C' , and strain hardening index, n_{eq} , as follows

$$\frac{V_s}{V} \sin\phi = 2\sqrt{3}\varepsilon_{AB} \quad (A7)$$

And

$$k_{AB} = \frac{\sigma_{AB}}{\sqrt{3}} \quad (A8)$$

$$C'n_{eq} = \left(\frac{dk}{ds_1}\right)_{AB} \frac{1}{2k_{AB}} = C' \left(\frac{d\sigma_{AB}}{d\varepsilon_{AB}}\right) \left(\frac{\varepsilon_{AB}}{\sigma_{AB}}\right) \quad (A9)$$

In Eq. A9, Oxley's strain rate constant, C' , simplifies at both ends of the equation and strain hardening index n_{eq} is

$$n_{eq} = \left(\frac{d\sigma_{AB}}{d\varepsilon_{AB}}\right) \left(\frac{\varepsilon_{AB}}{\sigma_{AB}}\right) \quad (A10)$$

Considering that for BCC, Zerilli-Armstrong constitutive model (Eq. 5.2), the material stress is a function of strain, strain rate, and temperature and the first term of Eq. A10 “ $\left(\frac{d\sigma_{AB}}{d\varepsilon_{AB}}\right)$ ” is

$$\frac{d\sigma_{AB}}{d\varepsilon_{AB}} = \left(\frac{d\sigma}{d\varepsilon} \frac{d\varepsilon}{d\varepsilon}\right)_{AB} + \left(\frac{d\sigma}{d\dot{\varepsilon}} \frac{d\dot{\varepsilon}}{d\varepsilon}\right)_{AB} + \left(\frac{d\sigma}{dT} \frac{dT}{d\varepsilon}\right)_{AB} \quad (A11)$$

Applying derivative rules to BCC Zerilli-Armstrong constitutive model (Eq. 5.2), the derivative terms of Eq. A11 yield Eqs. A12-A14

$$\left(\frac{d\sigma}{d\varepsilon}\right)_{AB} = \frac{nC_5\varepsilon^n}{\varepsilon} \quad (A12)$$

$$\left(\frac{d\sigma}{dT}\right)_{AB} = c_1 \left(-c_3 + c_4 \ln\left(\frac{\dot{\varepsilon}}{\dot{\varepsilon}_0}\right)\right) e^{\left(-c_3T + c_4 \ln\left(\frac{\dot{\varepsilon}}{\dot{\varepsilon}_0}\right)\right)} \quad (A13)$$

$$\left(\frac{dT}{d\varepsilon}\right)_{AB} = \frac{\beta_T \sigma_{AB}}{\rho C_p} = \frac{\beta_T \left(C_0 + C_1 e^{\left(-C_3T + C_4 \ln\left(\frac{\dot{\varepsilon}}{\dot{\varepsilon}_0}\right)\right) + C_5 \varepsilon^n}\right)}{\rho C_p} \quad (A14)$$

As strain-rate assumed to be maximum at AB, the term “ $\left(\frac{d\dot{\varepsilon}}{d\varepsilon}\right)$ ” of equation A11 reduces to zero. Substituting equation, A12, A13, A14 and $\left(\frac{d\dot{\varepsilon}}{d\varepsilon}\right) = 0$ in Eq. A11 yields

$$\frac{d\sigma_{AB}}{d\varepsilon_{AB}} = \frac{nC_5\varepsilon^n}{\varepsilon} + \frac{\beta_T \left(C_0 + C_1 e^{\left(-C_3 T + C_4 \ln\left(\frac{\dot{\varepsilon}}{\dot{\varepsilon}_0} \right) \right) + C_5 \varepsilon^n} \right) C_1 \left(-C_3 + C_4 \ln\left(\frac{\dot{\varepsilon}}{\dot{\varepsilon}_0} \right) \right) e^{\left(-C_3 T + C_4 \ln\left(\frac{\dot{\varepsilon}}{\dot{\varepsilon}_0} \right) \right)}}{\rho C_p} \quad (A15)$$

Considering that $1/C_p \approx 0$ using Eqs. A11 and A15, the Oxley [30] equivalent strain hardening index $n_{eq}(BCC)$ for Zerilli–Armstrong BCC material approximated as

$$n_{eq}(BCC) = \frac{nC_5\varepsilon^n}{C_0 + C_1 e^{\left(-C_3 T + C_4 \ln\left(\frac{\dot{\varepsilon}}{\dot{\varepsilon}_0} \right) \right) + C_5(\varepsilon)^n}} \quad (A16)$$

Also Eq. A16 reported equivalent strain hardening index $n_{eq}(BCC)$ is applicable for Zerilli–Armstrong (BCC) material model with blue hardness additive term also reported in Eq. 4.

For Zerilli–Armstrong (FCC) with material flow stress described in Eq. 5.3, a similar approach is followed, and the equivalent strain hardening index $n_{eq}(FCC)$ is approximated by

$$n_{eq}(FCC) = \frac{nC_2\varepsilon^n e^{-C_3 T + C_4 \ln\left(\frac{\dot{\varepsilon}}{\dot{\varepsilon}_0} \right)}}{C_0 + C_2\varepsilon^n e^{\left(-C_3 T + C_4 \ln\left(\frac{\dot{\varepsilon}}{\dot{\varepsilon}_0} \right) \right)}} \quad (A17)$$